Karlsruhe Institute of Technology

Non-equilibrium quasiparticles and topological excitations in hybrid superconducting structures

Zur Erlangung des akademischen Grades eines
DOKTORS DER NATURWISSENSCHAFTEN
von der Fakultät für Physik des
Karlsruher Instituts für Technologie (KIT)

genehmigte

DISSERTATION

von

Dipl.-Phys. Andreas Franz Heimes

aus Lennestadt

Datum der mündlichen Prüfung:	12. Dezember 2014
Referent:	Prof. Dr. Gerd Schön
Korreferent:	Prof. Dr. Jukka P. Pekola

Contents

Preface

The present thesis covers the major part of my research activity carried out between 2011 and 2014 at the "Institut für Theoretische Festkörperphysik" of the Karlsruhe Institute of Technology. Here I will focus on two topics which touch upon different aspects of superconducting devices and differ not only in their phenomenology but also in the theoretical methodology. Therefore the thesis will be divided into two parts with the titles

(I) "Quasiparticle dynamics in hybrid superconducting single-electron transistors", and

(II) "Topological superconductivity from magnetic adatoms on top of superconductors"

In condensed matter, *quasiparticles* are fundamental excitations of a many-particle system with properties resembling those of elementary particles. In electronic systems like metals or semiconductors these quasiparticles behave like electrons but, e.g., with a different *effective* mass. In the language of second quantization the operator $c^\dagger_{k\sigma}$ creates an *electron* with momentum k and spin σ, whereas the operator $c_{k\sigma}$ removes it. Alternatively one could say that $c_{k\sigma}$ creates a *hole* with opposite charge. In the *superconducting* phase the situation is even more different. Since the early breakthrough of Bardeen, Cooper and Schrieffer in 1956 [1] we know that the ground state of a superconductor is composed of a condensate of electron-pairs, so-called Cooper pairs, whereas excitations above this ground state are superpositions of electrons and holes. These are most generally described by the so-called Bogolioubov quasiparticle operators, e.g., for a *spin-singlet* superconductor these are given by $u_k c^\dagger_{k\sigma} + \sigma v_k c_{-k,-\sigma}$.

If quasiparticles are not thermally excited but originate from other sources we speak about *non-equilibrium quasiparticles*. They are known, e.g., to limit the coherence of superconducting qubits [2, 3, 4, 5, 6] and reduce the accuracy of single-electron sources used for metrology [7, 8, 9]. Their undesirable presence is reflected in the frequently used term *quasiparticle poisoning*. Currently, there are great efforts in understanding and reducing their influence on the previously mentioned electronic devices.

In the first part of the thesis we will investigate the dynamics of non-equilibrium quasiparticles in a single-electron transistor (SET) which consists of a *small* superconducting island and two *normal* (non-superconducting) metallic leads that are separated by high-resistance tunnel barriers. In this particular setup quasiparticles have been created by a periodic perturbation. The overall number of quasiparticle excitations remains balanced via the interplay of tunneling-excitation and recombination due to electron-phonon interaction.

The small island we are considering is made of *conventional*, so-called s-wave superconductors. This means that the Cooper pair wavefunction has vanishing angular momentum $l = 0$ and the two electron spins assume a spin-singlet configuration. In these superconductors, the pairing originates from an effective attraction between electrons mediated

by a virtual exchange of phonons. The excitation of Bogolioubov quasiparticles comes along with an energy cost that is commonly known as superconducting excitation gap Δ. In order to *break* a Cooper pair, an energy equal to twice the gap is required, because a particle-hole pair is created. This pair may *recombine* to a Cooper pair by releasing its energy, e.g., into the phonon bath due to electron-phonon coupling. In order to fix the notation and in order to introduce the quasiparticle concept we give a very basic theoretical introduction to phonon-mediated superconductivity in chapter **1**.

In structures of small size and reduced dimensions, charging effects dramatically influence the transfer of electrons from the leads into the superconducting island, since the energy associated with adding a single electron to the island increases with decreasing system size. In particular, at low temperatures the transport of single electrons can be suppressed in a controllable way, a situation commonly known as *Coulomb-blockade*. A short discussion of Coulomb-blockade phenomena and experimental setups relevant for this work are presented in chapter **2**.

The physics of the Coulomb-blockade can be exploited to implement a periodic and sequential *one by one* transport of electrons. In the SET-setup this is realized by applying a DC bias voltage between the normal leads and an AC gate voltage to the metallic island. In this manner the Coulomb-blockade can be switched off for short times only, allowing for single tunneling events through the left and right tunneling barrier one after another. Therefore a single charge can be transfered through the single-electron transistor within one time-period of the applied AC gate voltage. This scenario is called *single-electron turnstile*. Single-electron turnstiles that are composed of superconductor – normal-metal heterostructures were first proposed in the group of Pekola [7]. They are one of the most promising high-precision current standards to be used for the redefinition of the Ampere [10]. Under the assumtion that ideally one electron is transferred at a time, these devices offer a direct link between driving frequency and current, i.e. $I = ef$. In chapter **3** we present a short review of single-electron turnstiles and a more detailed discussion of their working principle.

Recently Maisi *et al.* [9] demonstrated that single-electron turnstiles may also be used to investigate the dynamics of Bogolioubov quasiparticles. Since electrons are combinations of quasiparticles and holes, the tunneling of charge is directly related to the excitation and annihilation of Bogolioubov quasiparticles. Once quasiparticles are injected into the superconductor, their number relaxes either due to electron-phonon recombination or due to escape through the tunneling barriers. For the periodic *turnstile protocol* the injection is balanced by these relaxation processes leading to a quasi-stationary non-equilibrium quasiparticle number. Increasing the turnstile frequency leads on average to an enhanced quasiparticle number and vise versa. Furthermore, non-equilibrium quasiparticles contribute an additional current, which is detectable by standard single electron counting schemes. Thus, recording the single-electron current in dependence of the operation frequency offers a measure of the quasiparticle dynamics.

Theoretical models describing the interplay of tunneling and relaxation subject to the Coulomb-blockaded transport have been formulated in publications [I] and [II] of the publication list on page 7. In this thesis we focus on the approach of Ref. [II] which describes the non-equilibrium situation in a normal-metal – superconductor – normal-metal single-electron turnstile by the solution of a master equation for the probability to find excess charges on the island combined with a kinetic Boltzmann equation for the quasiparticle distribution. We formulate a model that appropriately accounts for the *parity effect*, i.e.,

we distinguish between even and odd numbers of electrons on the superconducting island. Because electrons condense into Cooper pairs the *odd* charging state has an extra quasiparticle which remains unpaired and accounts for an additional current contribution [11]. We find that our results are compatible with experimental observations in a rather wide frequency window for both, the single-quasiparticle limit as well as the regime with more than one quasiparticle.

In the second part of the thesis we proceed with aspects of *topological superconductivity*. Apart from *conventional* s-wave superconductors there exist superconductors with an *unconventional* pairing-mechanism and a Cooper pair wavefunction which is parametrized by higher spherical harmonics $Y_{lm}(\boldsymbol{k})$ in momentum space. For instance, strontium ruthenate (Sr_2RuO_4) is considered to be a $(k_x \pm ik_y)$-superconductor ($l = 1$ and $m = \pm 1$) corresponding to spin-triplet pairing. In nature there exist few examples of this type of pairing, with strontium ruthenate being one potential candidate. These superconductors are particularly interesting as they are known to host exotic quasiparticle excitations with properties similar to *Majorana particles* discussed in high-energy physics. In 1937 Ettore Majorana discovered that Dirac's equation could also support real solutions of fermionic fields, meaning that a spin-$\frac{1}{2}$ particle is its own antiparticle. So far there are no confirmed Majorana particles in nature. However, they can appear as specific quasiparticle excitations in electronic condensed matter systems. For the case of spin-triplet superconductors with fully spin-polarized fermion operators, c_k, the quasiparticle operator is given by $\gamma_k = u_k c_k + v_k c^\dagger_{-k}$. Particle-hole symmetry implies a direct link between the creation of a quasiparticle with energy E_k and the creation a quasi-hole with energy $-E_k$, i.e. $\gamma^\dagger_k(E_k) = \gamma_{-k}(-E_k)$, which in turn is the defining condition for a Majorana particle.[1]

In this thesis we focus on one-dimensional *topological* superconductors for which Majorana excitations appear as zero-energy states at the edges of the system. The two Majorana excitations make up a *delocalized* electronic state characterized by the fermionic operator $d = \gamma_1 + i\gamma_2$, with $\gamma_i = \gamma_i^\dagger$. The occupation of the fermionic state does not cost any energy, resulting in a two-fold degenerate ground state, comprising of the states $|0\rangle$ and $|1\rangle = d^\dagger |0\rangle$. The Majorana operators fulfill the fermionic commutator relations $\{\gamma_i, \gamma_j\} = 2\delta_{ij}$, however in contrast to ordinary fermions one can not define a occupation number because $\gamma_i^2 = 1$. Because of these properties Majorana excitations in condensed matter physics are different from those in particle physics. Nevertheless, we will call *Majorana-like* excitations in electronic systems *Majorana fermions* in the course of this thesis. In fact one finds that they are not usual fermions but instead Ising anyons. Upon an adiabatic exchange of the Majorana fermions in two-dimensional space one can unitarily rotate the two-fold degenerate ground-state, i.e. $|0\rangle \to |0\rangle$ and $|1\rangle \to i\,|1\rangle$, generating a non-Abelian Berry-phase. The arising topological phase gate constitutes the basis to perform topologically protected quantum computing with Majorana fermions.

In topological superconductors the appearance of zero-energy Majorana excitations is intimately connected to non-trivial topological properties of the system, which also leads to a protection of Majorana fermion bound states against local perturbations. In order to give a short overview of the emergent field of topological superconductivity we start with a conceptional introduction of the topological classification of bandstructures in chapter **4**. In particular we establish a connection between topology and the emergence of zero-energy edge states, often referred to as *bulk-boundary* correspondence, which allows

[1] In terms of field operators the particle-antiparticle identity is given by $\gamma(x,t) = \gamma^\dagger(x,t)$ with $\gamma(x,t) = \int dk e^{ikx - iE_k t}\gamma_k$ (here x and t are spacetime coordinates).

immediately for a conclusion whether Majorana zero-energy states are possible or not.

Recently many different proposals appeared discussing the possibility of engineering *topological* superconductors with the objective to realize and manipulate Majorana zero-energy excitations. In chapter **4** we discuss some of them. The main ingredient needed to engineer a triplet superconducting gap is an s-wave superconductor with broken spin-rotational symmetry. The latter can be achieved by proximity of superconductivity to magnetism or spin-orbit coupling. In spring 2012 the group of Kouwenhoven [12] presented the first encouraging but not yet fully conclusive experimental signatures of zero-energy Majorana states in heterostructures of Rashba spin-orbit coupled nanowires and s-wave superconductors. Even more recently, in autumn 2014, the group of Yazdani [13] published results on one-dimensional wires of magnetic atoms on top of a spin-orbit coupled superconductor. The scanning tunneling microscopy (STM) technique they used made it possible to map the local density of states and identify the emergent zero-energy state at the edges of the atomic wire.

In chapter **5** we present two alternative Majorana platforms relying on collinear, i.e., either ferromagnetically (FM) or antiferromagnetically (AFM) ordered, chains of magnetic adatoms on top of a *conventional* superconductor. These systems can be produced with state-of-the-art STM techniques [14]. The two proposals have been presented in articles [III] and [IV]. They rely on additional quasiparticle states that are induced within the excitation gap of the s-wave superconductor by the presence of magnetic adatoms. The corresponding wavefunctions are localized at each adatom site and due to hybridization form bands, so-called *Shiba bands*[2] (for a basic discussion of magnetic atoms in superconductors we refer to chapter **1**).

The first part of chapter **5** is devoted to the discussion of Shiba bands that emerge in AFM adatom chains under the influence of external control fields. More precisely, spin-rotational invariance is broken by a magnetic field, which in combination with a supercurrent generates a coupling between momentum and spin, similar to the spin-orbit coupling in the realizations [12] and [13]. We find that the resulting zero-energy Majorana excitations show peculiar features like a characteristic spatial profile of their wavefunctions as well as specific electronic spin-polarization, which can be measured and manipulated in a STM setup.

In the second part of chapter **5** we discuss adatom chains which are deposited on a Rashba spin-orbit coupled superconductor. Spin-orbit coupling leads to an effective *anisotropic* Ruderman-Kittel-Kasuya-Yosida (RKKY) superexchange interaction [18, 19, 20] between adatoms, favoring a spiral order of their magnetic moments. We discuss how the additional presence of crystal-field effects may stabilize FM and AFM orders. Furthermore we show that both, FM and AFM adatom chains, harbor phases with one or two zero-energy Majorana states per edge. These can be realized by an appropriate choice of materials and adatom-spacing. In the final part of the thesis we discuss new directions on how to experimentally access the various Majorana phases and how to manipulate them in order to perform quantum information processing. We show that a logical Majorana qubit can be defined on a single adatom chain and present a general idea on how to couple certain Majorana operators using external fields. This provides ways to apply single-qubit operations or couple the Majorana qubit to other solid state quantum information devices.

[2]These quasiparticle states have been independently discussed by Yu [15], Rusinov [16] and Shiba [17], they are often solely called *Shiba states*.

List of Publications

Some parts covered in this work have already been published:

I. *"Excitation of single quasiparticles in a small superconducting Al island connected to Normal-Metal Leads by Tunnel Junctions"* [partly covered in chapter 2 and 3]
V. F. Maisi, S. V. Lotkhov, A. Kemppinen, A. Heimes, J. T. Muhonen, and J.P. Pekola, Phys. Rev. Lett. **111**, 147001 (2013).

II. *"Tunneling and relaxation of single quasiparticles in a normal-superconductor-normal single-electron transistor"* [covered in chapter 3]
A. Heimes, V. F. Maisi, D. S. Golubev, M. Marthaler, G. Schön, and J.P. Pekola, Phys. Rev. B **89**, 014508 (2014) Editors' Suggestion.

III. *"Majorana fermions from Shiba states in an antiferromagnetic chain on top of a superconductor"* [covered in chapter 5]
A. Heimes, P. Kotetes, and G. Schön, Phys. Rev. B **90**, 060507 (2014) Rapid Communication.

IV. *"Interplay of topological phases in magnetic adatom-chains on top of a Rashba superconducting surface"* [covered in chapter 5]
A. Heimes, D. Mendler, and P. Kotetes, arXiv:1410.6367 (2014), submitted.

Further publications not covered in this work:

V. *"Electronic dispersion anomalies in iron pnictide superconductors"*
A. Heimes, R. Grein, and M. Eschrig, Phys. Rev. Lett. **106**, 047003 (2011).

VI. *"Effect of spin fluctuations on the electronic structure in iron-based superconductors"*
A. Heimes, R. Grein, and M. Eschrig, Phys. Rev. B **86**, 064528 (2012).

Acknowledgements

First I would like to thank Gerd Schön for offering me a PhD-position and supporting me in various ways over the past three years. I hope I was a student worth investing in.

Furthermore I want to thank Jukka Pekola for being the *opponent* of this thesis and for involving me in his work. I have benefited a lot from our discussions together with Ville Maisi.

Special thanks goes to Panagiotis Kotetes and Dima Golubev for their scientific guidance. Most of the results presented in this work I owe to your support. Our discussions always have been very enlightening.

The working environment at the Institut für Theoretische Festkörper always has been very supportive. I acknowledge discussions with all the other PhD students and postdocs. Special thanks go to Christian Karlewski, Daniel Mendler and Sebastian Zanker for reading parts of this thesis and providing valuable suggestions. Furthermore Andreas Poenicke for his IT-support and his collaboration in the organization of the exercise course for Quantummechanics I. Last but not least I thank Thomas Hellmuth for having been a good and reliable climbing partner.

During all the years my family has proven to be an invaluable support. In particular I thank Theresa to stand by my side and support me in every situation of life. I thank my parents, Gabriele and Günter, for their financial support during my undergraduate physics studies and their help whenever I need it.

Theoretical Background

1. Microscopic theory of superconductivity

The microscopic theory of phonon mediated superconductivity is well established since the early breakthrough by Bardeen, Cooper and Schriefer (BCS) in 1957. According to Cooper (1956) the superconducting phase can be understood as a condensate of electron pairs (so called Cooper-pairs), which form a bound-state due to a weak attraction among each other. In *conventional* superconductors the pairing instability is caused by the virtual exchange of phonons, which is a retarded and an effectively local interaction. As a consequence the Cooper-pair wavefunction assumes its most symmetric form, i.e. vanishing relative orbital angular momentum and spin-singlet configuration – so called s-wave pairing.

On top of the superconducting condensate there exist quasiparticle excitations. They are combinations of electrons and holes which are separated from the ground state energy by an excitation gap Δ. They may be thermally excited or injected by an external source. Their relaxation is maintained by quasiparticle-phonon scattering and quasiparticle recombination processes, which essentially determine the quasiparticle dynamics. The first main part of this thesis will be devoted to the study of non-equilibrium quasiparticles in driven single electron transistors. In order to understand the pairing instability as well as the quasiparticle relaxation processes in more detail, we will start with a short discussion of the microscopic equilibrium theory of phonon-mediated superconductivity in the following section 1.1.

After that, in section 1.2, we will talk about the effect of magnetic atoms in *conventional* superconductors. Their presence leads to the emergence of quasiparticle states below the continuum excitation gap Δ, so-called *Shiba-states*, whose wavefunctions are localized close to the magnetic atoms' position. The hybridization of a number of such states leads to the formation of bands. In the second main part of the thesis we will show that under certain conditions these *Shiba-bands* have the properties of a topological superconductor. Accordingly section 1.2 is targeted to give a conceptional discussion of magnetic atoms in conventional superconductors and the emergence of Shiba-states.

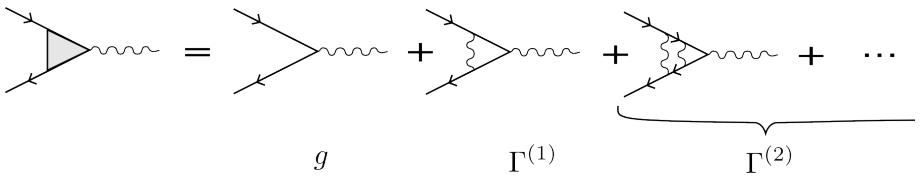

Figure 1.1.: Vertex correction to the electron-phonon interaction. Full lines are electron propagators, wiggly lines are phonon propagators.

1.1. Strong-coupling theory

The Born-Oppenheimer approximation is an essential step towards the decoupling of electronic degrees of freedom and lattice dynamics. It states that the electronic wave-functions follow adiabatically the ionic movement and corrections of the wave functions scale with a factor $\sqrt{m/M}$, where M is the mass of the ion and m is the mass of the electron. Equivalently one could say that the electron-phonon interaction is retarded, i.e. if an electron emits a phonon it is long out of reach until a second electron absorbs this phonon. This process scales with the relation of Fermi-velocity v_F and phonon-velocity c, i.e. $c/v_F \sim \sqrt{m/M}$. The electron-phonon interaction is described by the Hamiltonian

$$H_{e-ph} = \sum_{\boldsymbol{q}\boldsymbol{k}\sigma} g_{\boldsymbol{k}+\boldsymbol{q},\boldsymbol{k}} c^\dagger_{\boldsymbol{k}+\boldsymbol{q}\sigma} c_{\boldsymbol{k}\sigma} (b_{\boldsymbol{q}} + b^\dagger_{-\boldsymbol{q}}), \tag{1.1}$$

where $c^\dagger_{\boldsymbol{k}\sigma}$ creates an electron with energy ξ_k in the state with momentum k and spin σ. Furthermore $b^\dagger_q$ is the creation operator for a phonon with momentum q (we neglected its polarization for simplicity) and $g_{\boldsymbol{k}+q,\boldsymbol{k}}$ is a momentum-dependent coupling strength. The retardation effect, mentioned before, has direct consequences on the electron-phonon interaction. It implies that vertex corrections may be neglected. The leading vertex corrections can be calculated in a diagrammatic fashion (see Fig. 1.1). Here the straight and wiggly lines correspond to electron and phonon propagators respectively A straightforward estimation can be found in standard textbooks [21] and shows that the first order vertex correction is typically given by

$$\Gamma^{(1)} \sim g\sqrt{\frac{m}{M}}. \tag{1.2}$$

with $g = g_{\boldsymbol{k}+\boldsymbol{q},\boldsymbol{k}}$. This means that vertex corrections in the electron-phonon interaction can be generally neglected because $m \ll M$. This approximation is known as *Migdal's theorem*. Concerning the superconducting paring instability we will show that it allows a perturbative treatment of electron-phonon coupling in terms of a large-N expansion of the corresponding electronic self-energy, which falls under the concept of the Eliashberg equations of superconductivity.

Eliashberg equations

Within Migdal's approximation we can proceed to calculate the electronic energy corrections due to the electron phonon interaction, in particular we discuss the emergence of

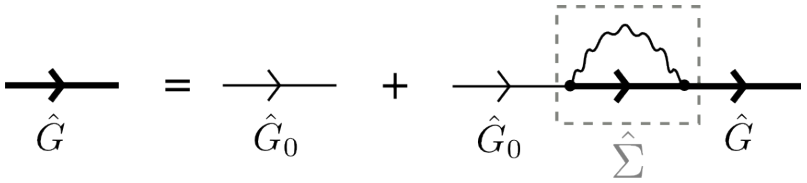

Figure 1.2.: Dyson equation for the Gor'kov Nambu Green's function $\hat{G}$ together with the selfenergy $\hat{\Sigma}$ in the large N approximation.

superconductivity. It is convenient to write the electron-phonon interaction (1.1) in terms of the Gor'kov Nambu spinors $\psi^\dagger_{\boldsymbol{k}} = (c^\dagger_{\boldsymbol{k}\uparrow},\, c_{-\boldsymbol{k}\downarrow})$, i.e.

$$H_{\mathrm{e-ph}} = \frac{1}{2}\sum_{\boldsymbol{q}\boldsymbol{k}\sigma} g_{\boldsymbol{k}+\boldsymbol{q},\boldsymbol{k}}\psi^\dagger_{\boldsymbol{k}+\boldsymbol{q}}\tau_z\psi_{\boldsymbol{k}}(b_{\boldsymbol{q}} + b^\dagger_{-\boldsymbol{q}}), \tag{1.3}$$

where τ_i ($i = x, y, z$) are the Pauli-matrices acting in particle-hole space. The fact that electrons can condense into Cooper pairs manifests itself in a finite s-wave pairing amplitude $\langle\psi^\dagger_{\boldsymbol{k}}\tau_x\psi_{\boldsymbol{k}}\rangle$. According to that the Matsubara Green's functions in the Gor'kov Nambu representation has off-diagonal components $F(\boldsymbol{k},\tau) = -\mathrm{T}\,\langle c_{\boldsymbol{k}\uparrow}(\tau)c_{-\boldsymbol{k}\downarrow}(0)\rangle$, i.e.

$$\hat{G}(\boldsymbol{k}, i\varepsilon_n) = \begin{pmatrix} G(\boldsymbol{k}, i\varepsilon_n) & F(\boldsymbol{k}, i\varepsilon_n) \\ F^*(-\boldsymbol{k}, -i\varepsilon_n) & -G^*(-\boldsymbol{k}, -i\varepsilon_n)\end{pmatrix}. \tag{1.4}$$

This Green's function is renormalized due to the electron-phonon interaction as shown by the Dyson series in Fig. 1.2. Note that vertex corrections are neglected due to Migdal's theorem and the full Green's function enters in a self-consistent way. The selfenergy is given by

$$\hat{\Sigma}_{ph}(\boldsymbol{k}, i\varepsilon_n) = -g^2 k_{\mathrm{B}}T\sum_{\varepsilon'_n}\int\frac{d\boldsymbol{k}'}{(2\pi)^3}\,\tau_z\,\hat{G}(\boldsymbol{k}', i\varepsilon'_n)\,\tau_z\,D(\boldsymbol{k}-\boldsymbol{k}', i\varepsilon_n - i\varepsilon'_n) \tag{1.5}$$

Here $\hat{G}(\boldsymbol{k}, i\varepsilon_n) = [i\varepsilon_n - \xi_{\boldsymbol{k}}\tau_z - \hat{\Sigma}_{ph}(\boldsymbol{k}, i\varepsilon_n)]^{-1}$ is the renormalized electronic Green's function and $D(\boldsymbol{q}, i\omega_n) = -\omega_{\boldsymbol{q}}/(\omega^2_{\boldsymbol{q}} + \omega^2_n)$ is the phonon propagator. It turns out that it is convenient to parametrize the selfenergy (1.5) in terms of a renormalization function Z and the off-diagonal pairing amplitude ϕ, i.e. $\hat{\Sigma}_{ph}(\boldsymbol{k}, i\varepsilon_n) = [1 - Z(\boldsymbol{k}, i\varepsilon_n)] + \phi(\boldsymbol{k}, i\varepsilon_n)\tau_x$. Selfenergy corrections proportional to τ_z can be generally neglected because of particle-hole symmetry. In a metal we have $\omega_D \ll v_F k_F$ and because of that the electronic dispersion can be essentially linearized around the Fermi-surface, i.e. $\int\frac{d\boldsymbol{k}'}{(2\pi)^3} \to \mathcal{N}_{\mathcal{F}}\int d\xi\int\frac{d\Omega'_F}{4\pi}$, where the latter integral denotes an angle average over the whole Fermi surface and $\mathcal{N}_F$ is the density of states. For many conventional superconductors it turns out that the electronic spectral function and consequently the selfenergy corrections are nearly isotropic. To this end one can perform a Fermi-surface average $\langle\cdot\rangle_F = \int\frac{d\Omega_F}{4\pi}(\cdot)/\int\frac{d\Omega_F}{4\pi}$ of (1.5) yielding the exclusively energy dependent expressions for the renormalization function Z and the off-diagonal component ϕ. Together with a analytical continuation of the Matsubara sum to an energy integral over the real axis we obtain the so-called *Eliashberg*

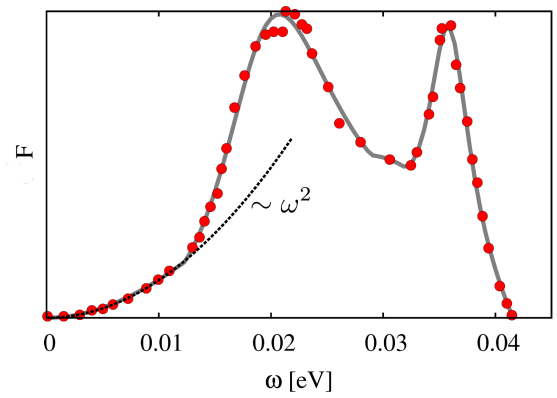

Figure 1.3.: Phonon density of states $F(\omega)$ of Aluminum (Al). The experimental data (red points) was extracted from inelastic neutron scattering [24].

equations [22, 23]

$$\begin{aligned}\left\langle \hat{\Sigma}_{ph}(\boldsymbol{k},\varepsilon)\right\rangle_F &= (1-Z(\varepsilon))\varepsilon + \phi(\varepsilon)\tau_x = \\ &\int_{-\infty}^{\infty} dz \int_{-\infty}^{\infty} d\omega\, \alpha^2(\omega)F(\omega)\mathrm{Re}\left\{\frac{zZ(z)-\phi(z)\tau_x}{\sqrt{z^2Z^2(z)-\phi^2(z)}}\right\}\mathrm{sign}(z)\mathrm{sign}(\omega) \\ &\times \frac{1}{2}\frac{\tanh(\frac{z}{2k_BT}) + \coth(\frac{\omega}{2k_BT})}{\varepsilon-\omega-z+i0}.\end{aligned} \tag{1.6}$$

In Eq. (1.6) we have introduced the α^2F-spectrum

$$\alpha^2(\omega)F(\omega) = \frac{1}{\mathcal{N}_F V}\sum_{\boldsymbol{k}\boldsymbol{k}'} |g_{\boldsymbol{k},\boldsymbol{k}'}|^2 \delta(\xi_{\boldsymbol{k}})\delta(\xi_{\boldsymbol{k}'})\delta(\omega-\omega_{\boldsymbol{k}-\boldsymbol{k}'}). \tag{1.7}$$

For many metals one finds that the energy dependence of α^2F approximately follows the phonon density of states $F(\omega) = \sum_{\boldsymbol{q}} \delta(\omega-\omega_{\boldsymbol{q}})$. This is in particular true for the low energy sector, where the density of states assumes a quadratic form (see Fig. 1.3). Both the phonon density of states as well as the α^2F-spectrum are peaked at two energies which can be attributed to transversal and longitudinal phonon-modes at the Brillouin-zone respectively.

In general the solution of Eq. (1.6) is not sufficient to explain the experimental situation. In fact electrons which feel the attractive phonon mediated interaction can not completely avoid the Coulomb repulsion among each other. Under the assumption that on average the electrons feel a Coulomb repulsion $V_C(\boldsymbol{k},\boldsymbol{k})$, which for the sake of simplicity shall be constant for $\xi_{\boldsymbol{k}}$, $\xi_{\boldsymbol{k}'} < E_F$ and zero elsewhere, the interaction enters via an additional off-diagonal self-energy, given by [22, 23]

$$\phi_c(\varepsilon) = -\mu^* \int_0^{\omega_c} dz \tanh\left(\frac{z}{2k_BT}\right)\mathrm{Re}\left\{\frac{\phi(z)}{\sqrt{z^2Z^2(z)-\phi^2(z)}}\right\}. \tag{1.8}$$

Here the generally complicated Coulomb interaction is hidden in the phenomenological parameter $\mu^* = \mathcal{N}_F\mathcal{V}V_C/[1+\mathcal{N}_F\mathcal{V}V_C\ln(E_F/\omega_c)]$. It is renormalized by a high-energy cutoff ω_c that has to be introduced for numerical reasons.

Eq. (1.6) together with Eq. (1.8) can be solved numerically in a iterative and self-consistent fashion. The result for the renormalization function Z as well as the superconducting gap

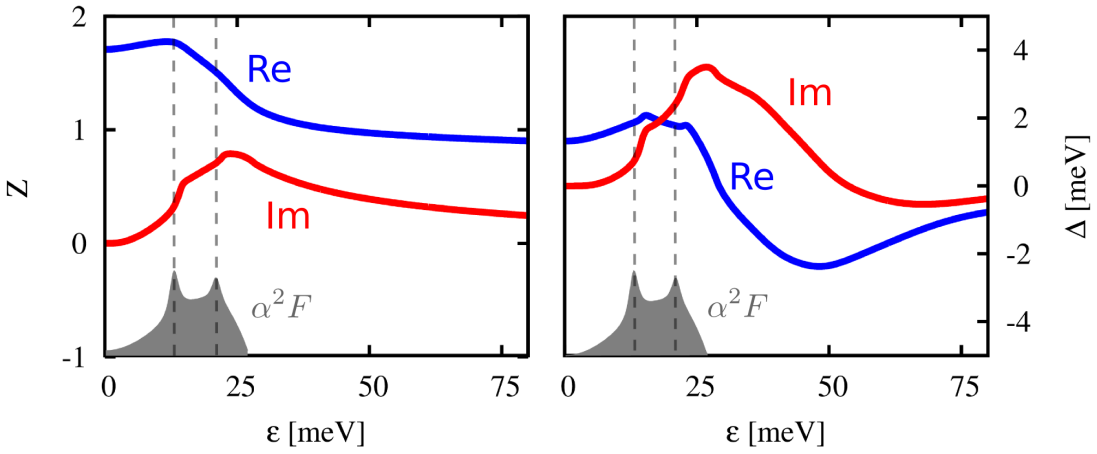

Figure 1.4.: The real and imaginary parts of the renormalization function Z and the superconducting gap Δ for the material Nb at a temperature $T = 2\,K$. The α^2F-spectrum used in the calculations is indicated by the gray shaded area and follows the data of Ref. [25].

$\Delta = \phi/Z$ are presented in Fig. 1.4 for the material niobium (Nb) and a temperature of $T = 2\,\mathrm{K}$. A comparison with the α^2F-spectrum shows that the phonon spectrum most dominantly imprints in the real and imaginary parts of the self-energies at energies $\Delta_0+\omega_i$ where now $\Delta_0 = \mathrm{Re}[\Delta(\Delta_0)]$ is the excitation gap of the superconductor and ω_i are the energy-peaks indicated by gray dashed lines in Fig. 1.4. These features also imprint on the *normalized* density of states,

$$\rho(\varepsilon) = \mathrm{Re}\left\{\frac{\varepsilon}{\sqrt{\varepsilon^2 - \Delta^2(\varepsilon)}}\right\}. \tag{1.9}$$

Fig. 1.5 shows the density of states 1.9 that corresponds to the selfenergies in Fig. 1.4. A close-up of the density of states illustrates the imprint of the phonon-spectrum. This can be especially seen from a comparison with the BCS density of states where the superconducting gap has been replaced by the energy independet gap Δ_0. By measuring for instance the density of states in a tunneling experiment, one can inversely extract the α^2F spectrum and by that the effective coupling between electrons and phonons. In particular for low energies the α^2F-spectrum is well parametrized by a single parameter, b, i.e. $\alpha^2(\omega)F(\omega) = b\omega^2$. A list of b for diverse superconductors can be for instance found in Ref. [26].

BCS limit and quasiparticle lifetimes

As long as energies are concerned which are of the order of Δ_0 the leading order of the real parts of both, the superconducting gap Δ as well as the renormalization function is approximately energy independent (see Fig. 1.4). The BCS approximation is accomplished by approximating the kernel

$$\Lambda(\varepsilon - z) = \int_0^\infty dz\, \frac{\alpha^2(\omega)F(\omega)\,2\omega}{\omega^2 - (\varepsilon - z + i0)^2} \tag{1.10}$$

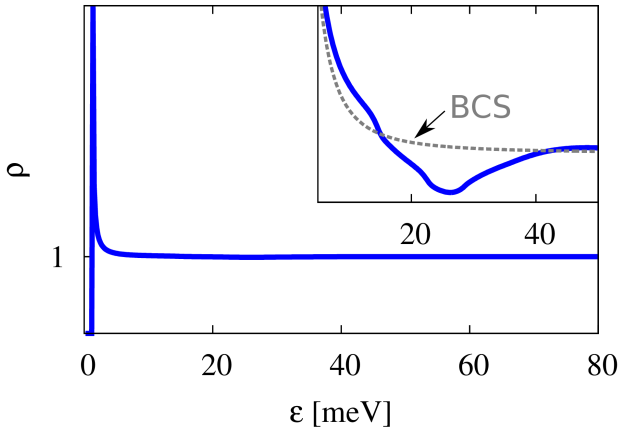

Figure 1.5.: The density of states Eq. (1.9) corresponding to the self-energies in Fig. 1.4. The inset shows a close-up comparison to BCS density of states.

in Eq. (1.6) by a finite constant, $\lambda = \Lambda(0)$, as long as the two energies ϵ and z are within a energy-range $(-\omega_c, \omega_c)$ around the Fermi surface. For convenience we have chosen the cutoff to agree with the one introduced for the Coulomb interaction (1.8). Within this approximation the renormalization function reduces to

$$Z_0 = 1 + \lambda. \tag{1.11}$$

Furthermore for the superconducting gap we obtain the BCS equation

$$\Delta_0 \approx \frac{\lambda - \mu^*}{2Z_0} \int_0^{\omega_c} dz \mathrm{Re}\left\{ \frac{\Delta_0}{\sqrt{z^2 - \Delta_0^2}} \right\} \tanh(\frac{z}{2k_\mathrm{B}T}). \tag{1.12}$$

Typically for conventional superconductors the effective coupling constant λ is smaller than one. In the weak coupling limit $T_c \ll \omega_c$ the linearized version of Eq. (1.12) can be solved, yielding the superconducting transition temperature

$$k_\mathrm{B}T_c = 1.13\,\omega_c \exp\left(-\frac{1+\lambda}{\lambda - \mu^*}\right). \tag{1.13}$$

Mind that all the information about the phonon-spectrum is hidden in the mass enhancement factor λ as well as ω_c which is meant to be a characteristic phonon energy.

Whereas the real parts of renormalization function as well as the superconducting gap remain finite at small temperatures, their imaginary parts are exponentially suppressed. The leading order of the imaginary part $\Delta_2 = \mathrm{Im}(\Delta)$ is given by

$$\Delta_2(\varepsilon) = \frac{1}{Z_0}\big[\phi_2(\varepsilon) - \Delta_0 Z_2(\varepsilon)\big], \tag{1.14}$$

For low temperatures $k_\mathrm{B}T \ll \Delta_0$ it turns out that the energy integrals for the imaginary parts of Eq. (1.6) can be carried out by replacing $\Delta = \phi/Z$ by its leading order Δ_0. Furthermore the phonon energies ω are restricted to small energies, where the α^2F-spectrum assumes the quadratic form $\alpha^2(\omega)F(\omega) = b\omega^2$. In particular we find an analytic approximation for Δ_2 right at the continuum gap $\varepsilon = \Delta_0$, i.e.

$$\Delta_2(\Delta_0) \approx -\frac{(\Delta_0)^3\pi b}{Z_0}\left[\frac{15\sqrt{\pi}}{8}\zeta(7/2)\left(\frac{k_\mathrm{B}T}{2\Delta_0}\right)^{7/2} + \sqrt{\pi}\left(\frac{k_\mathrm{B}T}{2\Delta_0}\right)^{1/2} e^{-\Delta_0/T}\right] \tag{1.15}$$

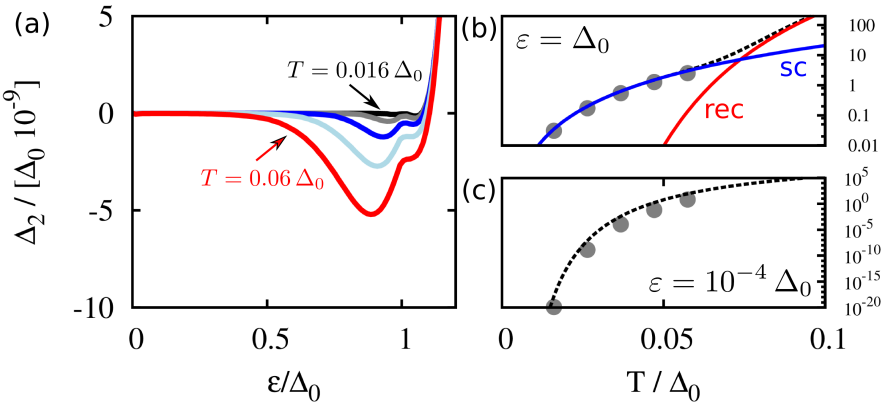

Figure 1.6.: (a) The imaginary part Δ_2 as obtained from the numerical solution of the Eliashberg equations for different temperatures. (b) Δ_2 at $\varepsilon = \Delta_0$: Gray dots are the numerical result extracted from (a), lines are the analytical approximations in Eq. (1.15). The contribution from electron-phonon scattering and recombination is shown by the blue and red line respectively. (c) Δ_2 deep inside the gap. Like in (b) the gray dots are numerical results, whereas the line represents the analytical approximation of Eq. (1.16).

The first term proportional to $(k_\mathrm{B}T/2\Delta_0)^{7/2}$ originates from the inelastic scattering of quasiparticles with phonons, a process which conserves the quasiparticle number, whereas the second term is proportional to the thermally excited number of quasiparticles $N_{qp} \approx \mathcal{N}_F\mathcal{V}\sqrt{2\pi}\sqrt{\Delta_0 k_\mathrm{B}T}\exp(-\Delta_0/k_\mathrm{B}T)$ [9] and corresponds to the recombination with other quasiparticles into Cooper-pairs. Deep inside the gap we find

$$\Delta_2(\varepsilon \ll \Delta) \approx -\frac{(\Delta_0)^3\pi b}{Z_0}\frac{\sqrt{\pi}\Delta_0}{8\,\varepsilon}\left(\frac{k_\mathrm{B}T}{2\Delta_0}\right)^{1/2} e^{-(\Delta_0-\varepsilon)/T}. \tag{1.16}$$

Consequently the density of states $\rho(\varepsilon) = -\Delta_2\varepsilon/\Delta_0^2$ remains finite, even at the Fermi-energy $\varepsilon = 0$. The latter approximations (1.15) and (1.16) agree well with the numerical solution of Δ_2 as shown in Fig. 1.6. Finally we summarize the electron-phonon coupling b in (1.1), as well as the prefactor $(\Delta_0)^3\pi b/Z_0$, that appears in Eqs. (1.15) and (1.16), for various materials in table 1.1.

In the literature the finite broadening of the density of states, which is among other things a direct consequence of a non-vanishing Δ_2, is often parameterized by a finite lifetime τ, i.e.

$$\rho(\varepsilon) = \mathrm{Re}\left\{\frac{\varepsilon + i/\tau(\varepsilon)}{\sqrt{(\varepsilon + i/\tau(\varepsilon))^2 - \Delta_0^2}}\right\}. \tag{1.17}$$

The parameter $1/\tau(\varepsilon)\Delta_0$ is often referred to as Dynes parameter [27]. In particular we identify $1/\tau(\Delta_0) = \Delta_2(\Delta_0)$, consistent with the quasiparticle scattering rates derived by Kaplan *et al.*[26]. In tunneling experiments a finite density of states within the gap leads to a leakage current, which however can be as well attributed to mechanisms other than a subgap density of states. The smallest Dynes parameter that has been observed so far is of the order 10^{-7} and was measured for the superconductor aluminum [28].

Comparison to the mean-field BCS-theory

The mean-field theory of superconductivity introduced by Bardeen, Cooper and Schriefer [1] neglects the finite life-time broadening that has been discussed in the previous section.

	$10^3\, b$	T_C [K]	$(\Delta_0)^3\pi b/Z_0[10^{-4}\,\mathrm{eV}]$
Al	0.317	1.19	4.22×10^{-4}
Nb	4.0	9.2	1.19
Pb	5.72	7.19	1.24

Table 1.1.: Electron-phonon coupling b, transition temperature T_C, and prefactor in Eqs. (1.15) and (1.16) for different materials taken from Ref. [26].

.

Assuming an effectively attractive interaction between electrons the electronic Hamiltonian can be written as

$$H = \sum_{\boldsymbol{k}\sigma} \xi_{\boldsymbol{k}\sigma} c^\dagger_{\boldsymbol{k}\sigma} c_{\boldsymbol{k}\sigma} - \eta^2 \sum_{\boldsymbol{k},\boldsymbol{k}'} c^\dagger_{\boldsymbol{k}\uparrow} c^\dagger_{-\boldsymbol{k}\downarrow} c_{-\boldsymbol{k}'\downarrow} c_{\boldsymbol{k}'\uparrow}. \tag{1.18}$$

Here the parameter η accounts for phonon mediated interaction. A mean-field decoupling of the interaction term yields

$$c^\dagger_{\boldsymbol{k}\uparrow} c^\dagger_{-\boldsymbol{k}\downarrow} c_{-\boldsymbol{k}'\downarrow} c_{\boldsymbol{k}'\uparrow} \approx - \left\langle c^\dagger_{\boldsymbol{k}\uparrow} c^\dagger_{-\boldsymbol{k}\downarrow} \right\rangle \left\langle c_{-\boldsymbol{k}'\downarrow} c_{\boldsymbol{k}'\uparrow} \right\rangle + \left\langle c^\dagger_{\boldsymbol{k}\uparrow} c^\dagger_{-\boldsymbol{k}\downarrow} \right\rangle c_{-\boldsymbol{k}'\downarrow} c_{\boldsymbol{k}'\uparrow} + c^\dagger_{\boldsymbol{k}\uparrow} c^\dagger_{-\boldsymbol{k}\downarrow} \left\langle c_{-\boldsymbol{k}'\downarrow} c_{\boldsymbol{k}'\uparrow} \right\rangle \tag{1.19}$$

such that the Hamiltonian assumes the form

$$\begin{aligned} H &= -\frac{2|\Delta|^2}{\eta^2} + \sum_{\boldsymbol{k}\sigma} \xi_{\boldsymbol{k}} c^\dagger_{\boldsymbol{k}\sigma} c_{\boldsymbol{k}\sigma} - \sum_{\boldsymbol{k}} \Delta^* c_{-\boldsymbol{k}\downarrow} c_{-\boldsymbol{k}\uparrow} + \Delta c^\dagger_{\boldsymbol{k}\uparrow} c^\dagger_{-\boldsymbol{k}\downarrow}, \\ &= -\frac{2|\Delta|^2}{\eta^2} + \sum_{\boldsymbol{k}\sigma} \xi_{\boldsymbol{k}} - \frac{1}{2} \sum_{\boldsymbol{k}\sigma} \psi^\dagger_{\boldsymbol{k}} [\xi_{\boldsymbol{k}} \tau_z + \mathrm{Re}\Delta \tau_x + \mathrm{Im}\Delta \tau_y] \psi_{\boldsymbol{k}}, \\ &= -\frac{2|\Delta|^2}{\eta^2} + \frac{1}{2} \sum_{\boldsymbol{k}\sigma} \psi^\dagger_{\boldsymbol{k}} [\xi_{\boldsymbol{k}} \tau_z - \Delta \tau_x] \psi_{\boldsymbol{k}}\,. \end{aligned} \tag{1.20}$$

Here we have chosen a real gauge for the superconducting gap

$$\Delta = \eta^2 \sum_{\boldsymbol{k}} \left\langle c_{-\boldsymbol{k}\downarrow} c_{\boldsymbol{k}\uparrow} \right\rangle, \tag{1.21}$$

introduced the spinor $\psi^\dagger_{\boldsymbol{k}} = (c^\dagger_{\boldsymbol{k}\uparrow}, c_{-\boldsymbol{k}\downarrow})$ and assumed particle-hole symmetry such that $\sum_{\boldsymbol{k}\sigma} \xi_{\boldsymbol{k}} = 0$. The Hamiltonian can be diagonalized by a so called Bogolioubov - transformation $\psi_{\boldsymbol{k}} = U_{\boldsymbol{k}} \widetilde{\psi}_{\boldsymbol{k}}$ with

$$U_{\boldsymbol{k}} = \begin{pmatrix} u_{\boldsymbol{k}} & v_{\boldsymbol{k}} \\ -v_{\boldsymbol{k}} & u_{\boldsymbol{k}} \end{pmatrix}, \qquad u^2_{\boldsymbol{k}} = \frac{1}{2}\left[1 + \frac{\xi_{\boldsymbol{k}}}{\sqrt{\xi^2_{\boldsymbol{k}} + \Delta^2}}\right], \quad v^2_{\boldsymbol{k}} = \frac{1}{2}\left[1 - \frac{\xi_{\boldsymbol{k}}}{\sqrt{\xi^2_{\boldsymbol{k}} + \Delta^2}}\right]. \tag{1.22}$$

By introducing the quasiparticle-operators $\widetilde{\psi}^\dagger_{\boldsymbol{k}} = (\gamma^\dagger_{k\uparrow}, \gamma_{-\boldsymbol{k}\downarrow})$ and the corresponding quasiparticle energy $E_{\boldsymbol{k}} = \sqrt{\Delta^2 + \xi^2_{\boldsymbol{k}}}$ the Hamiltonian assumes the diagonal form

$$H_{qp} = H + \frac{2|\Delta|^2}{\eta^2} = \sum_{\boldsymbol{k}\sigma} E_{\boldsymbol{k}} \gamma^\dagger_{\boldsymbol{k}\sigma} \gamma_{\boldsymbol{k}\sigma}. \tag{1.23}$$

Furthermore the the self-consistency gap-equation (1.21) is given by the familiar form of Eq. (1.12)

$$\Delta = \eta^2 \sum_{\boldsymbol{k}} u_{\boldsymbol{k}} v_{\boldsymbol{k}} (1 - \langle \gamma^\dagger_{\boldsymbol{k}\uparrow} \gamma_{\boldsymbol{k}\uparrow} \rangle - \langle \gamma^\dagger_{\boldsymbol{k}\downarrow} \gamma_{\boldsymbol{k}\downarrow} \rangle) = \eta^2 \sum_{\boldsymbol{k}} \frac{\Delta}{2E_{\boldsymbol{k}}} [1 - 2f(E_{\boldsymbol{k}})]. \tag{1.24}$$

Here the quasiparticle occupations $\langle \gamma^\dagger_{\boldsymbol{k}\uparrow} \gamma_{\boldsymbol{k}\uparrow} \rangle = \langle \gamma^\dagger_{\boldsymbol{k}\downarrow} \gamma_{\boldsymbol{k}\downarrow} \rangle = f(E_{\boldsymbol{k}})$ are expressed by the Fermi-Dirac function $f(E) = [\exp(E/k_{\mathrm{B}}T) + 1]^{-1}$. In particular we identify $\eta^2 = (\lambda - \mu^*)/Z_0 \mathcal{N}_F V$ by comparison with Eq. (1.12).

Within the BCS mean-field approach the finite life-time broadening as derived in Eq. (1.15) can be equivalently inferred from a perturbative treatment of the electron-phonon interaction (1.1). Technically, if the largest spectral weight of phonons lies at energies way greater than 2Δ (see for instance Fig. 1.3, where $\Delta \sim 2 \times 10^{-4}\,\mathrm{eV}$), one can absorb the high energy contribution in the coupling constant λ and therewith in the mean field order parameter Δ. The new quasiparticles $\gamma_{\boldsymbol{k}}$ then interact with the low-energy phonons leading to a finite relaxation rate which can be derived from simple golden-rule arguments [9]. In section 3.2.1 we will follow this approach in order to derive the quasiparticle relaxation rates of non-equilibrium quasiparticles in a superconducting single electron transistor.

1.2. Magnetic atoms in conventional superconductors

According to the pioneering work of Abrikosov and Gor'kov [29] magnetic impurities reduce the superconducting order parameter and lead to the appearance of quasiparticle states within the superconducting gap. The influence of magnetic atoms in superconductors has been widely discussed in the context of superconducting alloys and related subgap features have been measured in tunneling experiments with planar junctions [30]. With state of the art scanning tunneling microscopy (STM) it is even possible to probe the local effect of single impurities on top of a superconducting surface [31]. In this chapter we derive the energy of a bound-state that arises from a single magnetic atom. We follow an approach which will be used in chapter 5, where we derive the energy spectrum for many magnetic atoms. Later we will consider bound-state energies that lie deep inside the superconducting excitation gap. In this regime a *quantum phase transition* may occur. Furthermore, we comment on the large-coupling regime and the importance of the *Kondo effect*.

Single magnetic atom

Experimentally single magnetic atoms have been probed by STM spectroscopy, like for instance manganese (Mn) on niobium (Nb). The Hamiltonian of a three-dimensional superconductor including the local impurity potential of a single atom can be written as

$$H = \frac{1}{2} \sum_{\boldsymbol{k}} \psi^\dagger_{\boldsymbol{k}} [\xi_{\boldsymbol{k}} \tau_z - \Delta \tau_x] \psi_{\boldsymbol{k}} + \frac{1}{2} \sum_{\boldsymbol{k}\boldsymbol{k}'} \psi^\dagger_{\boldsymbol{k}} V_{\boldsymbol{k}-\boldsymbol{k}'} \psi_{\boldsymbol{k}'}. \tag{1.25}$$

Here $\psi^\dagger_{\boldsymbol{k}} = (c^\dagger_{\boldsymbol{k}\uparrow},\, c_{-\boldsymbol{k},\downarrow})$ is the spinor containing the particle and hole creation operators and τ_i are Pauli-matrizes in this particle-hole space. The momentum dependent potential $V_{\boldsymbol{k}-\boldsymbol{k}'} = U(\boldsymbol{k}-\boldsymbol{k}')\tau_z + J(\boldsymbol{k}-\boldsymbol{k}')S$ contains a non-magnetic contribution U and a magnetic

exchange energy J. In the following we assume that the spin is classical, meaning its amplitude is large, i.e. $S \to \infty$, and its direction is fixed. At the same time the exchange energy is small, i.e. $J \to 0$, however leaving the product JS finite. This assumption has been proven to be at least a qualitatively good approximation [32].

The Hamiltonian (1.25) can be diagonalized by applying a Bogolioubov transformation as done in (1.22). This sets a constraint to the particle and hole amplitudes $u_{\boldsymbol{k}}$ and $v_{\boldsymbol{k}}$ which are contained in the spinor $\Phi_{\boldsymbol{k}}^{\mathrm{T}} = (u_{\boldsymbol{k}},\, v_{\boldsymbol{k}})$,

$$[\xi_{\boldsymbol{k}}\tau_z - \Delta\tau_x]\Phi_{\boldsymbol{k}} + \sum_{\boldsymbol{k}'} V_{\boldsymbol{k}-\boldsymbol{k}'}\Phi_{\boldsymbol{k}'} = \varepsilon\Phi_{\boldsymbol{k}}. \tag{1.26}$$

This equation is commonly known as Bogolioubov-de Gennes (BdG) equation [32]. For the case of a point-like impurity and and under the assumption that it is spherical symmetric (s-wave scattering) the Fourier components entering the impurity potential can be replaced by constant coefficients, i.e. $U_{\boldsymbol{k}} = U$ and $J_{\boldsymbol{k}} = J$. By an additional summation over continuum states $\boldsymbol{k}$ the Eq. 1.26 can be recast in the form

$$\left\{1 - \hat{G}(\varepsilon)\big[U\tau_z + JS\big]\right\}\Phi = \hat{M}(\varepsilon)\Phi = 0. \tag{1.27}$$

Here we introduced the integrated Green's-function

$$\hat{G}(\varepsilon) = \sum_{\boldsymbol{k}}[\varepsilon - \xi_{\boldsymbol{k}}\tau_z + \Delta\tau_x]^{-1} = -i\pi\nu_F\frac{\varepsilon - \Delta\tau_x}{\sqrt{\varepsilon^2 - \Delta^2}} \tag{1.28}$$

with the density of states $\nu_F = \mathcal{N}_F V$. Furthermore the two-component spinor $\Phi = \sum_{\boldsymbol{k}}\Phi_{\boldsymbol{k}} = (u,\, v)^{\mathrm{T}}$ contains the particle and hole components u and v. Eq. (1.20) has a non-trivial solution if the determinant of $\hat{M}(\varepsilon)$ is zero, yielding an expression for the bound-state energy [32],

$$\frac{\varepsilon}{\Delta} = \frac{1 + (\pi\nu_F U)^2 - (\pi\nu_F JS)^2}{\sqrt{[1 + (\pi\nu_F U)^2 - (\pi\nu_F JS)^2]^2 + 4(\pi\nu_F JS)^2}}\,. \tag{1.29}$$

In the limit of $U = 0$ it reduces to

$$\frac{\varepsilon}{\Delta} = \pm\frac{1 - (\pi\nu_F JS)^2}{1 + (\pi\nu_F JS)^2}\,. \tag{1.30}$$

These energies lie energetically within the superconducting gap and have been first discussed by Yu, Shiba and Rusinov [15, 16, 17]. They are commonly known as *Shiba states* and we will stick to this denotation in the following.

The dependence of ε on coupling strength is shown in Fig. 1.8. With increasing coupling strength J the Shiba-states move deeper into the gap. Finally at $J^* = [(\pi\nu_F)^{-2} + U^2]^{1/2}$ they cross the Fermi level, having an important implication on the ground-state of the system (see next paragraph).

According to Eq. (1.27), for $U = 0$, the particle-hole amplitudes Φ are eigenfunctions of τ_x, meaning that the particle- and hole-components have the same weight. However, this is not completely compatible with experimental observations: Fig. 1.7 shows a STM

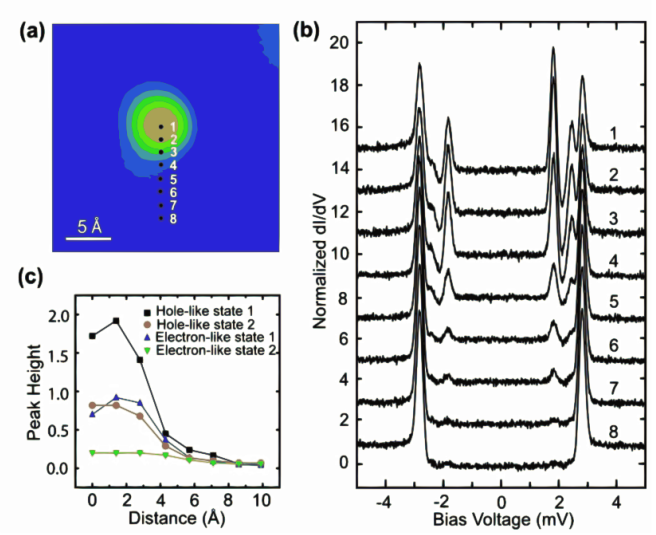

Figure 1.7.: (a) Spatially resolved STM figure of Mn on a Pb-surface. (b) dI/dV curves measured at the respective positions indicated in (a). Shiba states appear close to the magnetic atom. (c) Electron- and hole-like amplitudes for the two observed binding energies. (Figure from Ref. [33] with slight modifications)

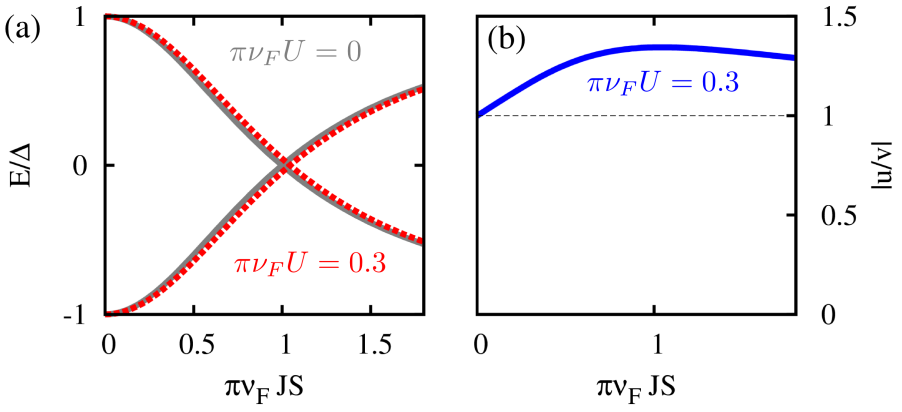

Figure 1.8.: (a) Bound-state energy (1.29) with and without considering the particle-hole asymmetric contribution U as a function of exchange energy J. At $\pi\nu_F JS = 1$ the system undergoes a quantum phase transition. (b) Difference in the electron-like and hole-like amplitudes u and v.

probe of a Mn atom on top of a Pb surface. The electron and hole-like local density of states show an asymmetry which can be for instance deduced from a finite local potential U. For finite U the relation between particle and hole-amplitudes is given by

$$\left|\frac{u}{v}\right| = \frac{1 + (\pi\nu_F JS + \pi\nu_F U)^2}{\sqrt{4(\pi\nu_F JS)^2 + [1 - (\pi\nu_F JS)^2 + (\pi\nu_F U)^2]^2}}. \tag{1.31}$$

In Fig. 1.8(a) we compare (1.30) with (1.29) and find that the particle-hole asymmetric local potential U has little influence on the energy of the Shiba-state. Though, it leads

to an observable particle-hole asymmetry in the amplitudes u and v [see Fig. 1.8(b)]. Alternatively a proper treatment of the particle-hole asymmetry in the substrate leads to a similar effect. In the *Shiba*-model with $U = 0$ this can be taken into account by phenomenologically adding an additional term to the Green's function, which accounts for the particle-hole asymmetry, i.e. $G(\varepsilon) \to G(\varepsilon) - i\alpha\tau_z$ [34].

Quantum phase transition

For small coupling strength J the BCS ground-state is given by

$$|\Psi_0\rangle \sim \prod_n [u_n + v_n c^\dagger_{n\uparrow} c^\dagger_{-n\downarrow}] \, |0\rangle \, . \tag{1.32}$$

Here $|0\rangle$ is the vacuum state corresponding to the completely filled Fermi-sea. The quasiparticle operators $\gamma_{n\uparrow} = u_n c_{n\uparrow} - v_n c^\dagger_{-n\downarrow}$ and $\gamma_{-n\downarrow} = u_n c_{-n\downarrow} + v_n c^\dagger_{n\uparrow}$ corresponds to the two time reversed quasiparticle states $(n, \uparrow)$ and $(-n, \downarrow)$. We denote $n = 1$ as the localized Shiba-state and subscribe the continuum excitations with the indeces $n > 1$. One finds that the energy of the state $|\Psi_{-1\downarrow}\rangle = \gamma^\dagger_{-1\downarrow} |\Psi_0\rangle$, which has an additional quasiparticle excitation $(-1, \downarrow)$, is higher than the ground-state energy as long as the coupling strength J does not exceed the critical value J^*. The situation is different for $J > J^*$: In this case the state $|\Psi_{-1\downarrow}\rangle$ is energetically lower than the original ground-state $|\Psi_0\rangle$. One finds that the new ground-state is no longer a spin-singlet, but that the average electronic spin is given by $\langle\Psi_{-1\downarrow}|S^{el}_z|\Psi_{-1\downarrow}\rangle = -1/2$. This means that the excited quasiparticle in the ground-state screens the impurity spin in favor of the gain in exchange energy [35].

The role of Kondo screening

So far we exclusively discussed the effect of classical spins, i.e. static spins in a superconducting host. However, if the spin quantum number S is small and the coupling J is large the spin couples dynamically to the conduction electrons. In the normal state strong coupling leads to qualitatively different results discussed in terms of the Kondo problem [36]. There, within the poor man's scaling approach, the coupling constant J becomes renormalized,

$$\bar{J} \sim \frac{J}{1 - J\nu_F \ln(D/k_\mathrm{B}T)}, \tag{1.33}$$

where D is the band-width of the conduction electrons [37]. In the case of antiferromagnetic coupling, $J > 0$, there exist a divergent energy-scale $k_\mathrm{B}T_K = D\exp(-1/\nu_F J)$ known as the Kondo-temperature. For $T \lesssim T_K$ the conduction electrons screen the impurity spin. This bound-state, e.g., leads to an enhanced resistivity at low temperatures. However, for ferromagnetic coupling, $J < 0$, the renormalized coupling $\bar{J}$ goes to zero as T is lowered, such that conduction electron and impurity decouple.

Now, in the superconducting state the density of states around the Fermi-level is depleted due to the opening of a gap, i.e. $\nu_F\rho(\varepsilon < \Delta) \ll \nu_F$, and there is a competition between the Kondo effect and superconducting phenomena. For anti-ferromagnetic coupling $J > 0$ and $T_K \gg T_c$ the conduction electrons screen the impurity like in the normal state. In this limit approximate values for the bound-state energies that emerges like in the classical case have been found [38],

$$\frac{\varepsilon}{\Delta} = \frac{1-\zeta^2}{1+\zeta^2} \tag{1.34}$$

where $\zeta \approx \frac{\pi\Delta}{4k_\mathrm{B}T_K} \ln\left(\frac{4ek_\mathrm{B}T_K}{\pi\Delta}\right)$ depends on the ratio of Kondo temperature T_K and superconducting gap Δ. The ground-state has an extra quasiparticle which screens the impurity spin. For $T_K \ll T_c$ Kondo-screening is suppressed due to the reduced density of states at the Fermi-level. A proper treatment of the intermediate regime has been performed with the help of a numerical renormalization group (NRG) analysis [38]. At $T_K \gtrsim 0.3T_c$ the authors of Ref. [38, 39] found a quantum-phase transition from a spin-singlet ground state to the doublet with an extra exited quasiparticle – just as discussed for the single classical impurity in section 1.2. Experimentally this transition was observed at $T_K \sim T_c$ for magnetic MnPc molecules absorbed on Pb [40].

For ferromagnetic coupling $J < 0$ the effective coupling (1.33) is reduced as well. The bound-state energy is approximately given by [32]

$$\frac{\varepsilon}{\Delta} = 1 - \frac{\pi^2}{8}\left(\frac{J/D}{1+(J/D)\ln(D/\Delta)}\right)^2, \tag{1.35}$$

therefore the bound-state energy is close to the quasiparticle continuum.

Later in this thesis, when we discuss Shiba-bands in chains of magnetic atoms, we will neglect the Kondo-effect. This is reasonable because, apart from the renormalization of the coupling constant, the energy-spectrum of the Shiba-bound states behaves qualitatively similar to the case of a classical magnetic moment, if the magnetic exchange, J, is antiferromagnetic. Furthermore, experiments on adatoms on metallic surfaces indicate that the Kondo-effect play a minor role [13, 14, 41, 42].

Part I.

Quasiparticle dynamics in hybrid superconducting single-electron transistors

2. Basics: Single-electron tunneling

The first part of this thesis will be devoted to the dynamics of non-equilibrium quasiparticles in a single-electron transistor. To this end we will give a short introduction into single-electron effects in mesoscopic devices in the following chapter. We start with a discussion about sequential tunneling and charging effects. In particular we introduce the single-electron transistor and related physical effects that are important later in our theoretical analysis in chapter 3.

Modern lithographic techniques allow for the fabrication of small metallic electrodes with widths of several 10 nm as well as tunneling junctions consisting of two electrodes that are separated by a thin, approximately $\sim 0.1\,\mathrm{nm}$ thick, insulating barrier. Although the overall number of electrons in such devices is large, the tunneling of just a single charge leads to so called *charging effects*, which considerably influence macroscopic observables like the current through the tunneling barrier.

Quantum tunneling of charge from one electrode to the other appears due to the leakage of wave functions and their overlap in the classically forbidden insulating barrier. This allows for a finite electrical current to pass through the junction. The Hamiltonian describing the electrodes and the tunneling junctions assumes the general form

$$H = H_L + H_R + H_T, \tag{2.1}$$

where $H_r = \sum_{\boldsymbol{k}} \xi_{\boldsymbol{k}} c^\dagger_{r\boldsymbol{k}} c_{r\boldsymbol{k}}$ with $r = L, R$ corresponds to the left and right electrode respectively and

$$H_T = \sum_{\boldsymbol{k}\boldsymbol{k}'} t_{\boldsymbol{k}\boldsymbol{k}'}\, c^\dagger_{L\boldsymbol{k}} c_{R\boldsymbol{k}'} + \mathrm{H.c.} \tag{2.2}$$

is the tunneling Hamiltonian with the tunneling matrix element $t_{\boldsymbol{k}\boldsymbol{k}'}$ between the states $\boldsymbol{k}$ and $\boldsymbol{k}'$. Here $c^\dagger_{r\boldsymbol{k}}$ creates an electron in the state with momentum $\boldsymbol{k}$ and energy $\xi_{\boldsymbol{k}}$ in the r-th electrode (for convenience we skip the spin-index).

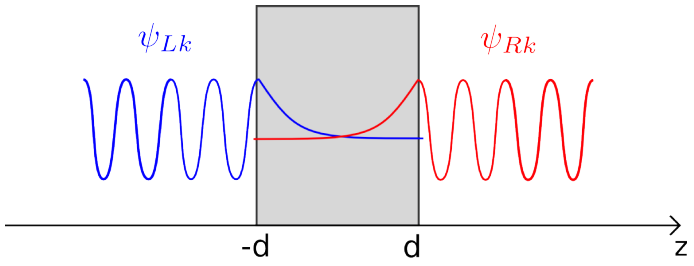

Figure 2.1.: Planar tunnel junction

For simplicity let us consider a planar junction as depicted in Fig. 2.1. The electronic wave-functions $\psi_{L\boldsymbol{k}}$ and $\psi_{R\boldsymbol{k}}$ leak into the classically forbidden and exhibit a small but finite overlap. The tunneling-rate of an electron incident from the left to the right lead can be inferred from Fermi's goldon rule,

$$\Gamma_{L\to R} = \frac{2\pi}{\hbar}\sum_{\boldsymbol{k}\boldsymbol{k}'} |t_{\boldsymbol{k}\boldsymbol{k}'}|^2 \left\langle c^\dagger_{L\boldsymbol{k}} c_{L\boldsymbol{k}}\right\rangle \left\langle c_{R\boldsymbol{k}'} c^\dagger_{R\boldsymbol{k}'}\right\rangle \delta(\xi_{\boldsymbol{k}} - \xi_{\boldsymbol{k}'} - eV)\,, \tag{2.3}$$

where V is a small bias voltage applied across the junction. The tunneling matrix element $t_{\boldsymbol{k}\boldsymbol{k}'}$ depends on microscopic details. For the simple planar junction geometry it can be derived in terms of Bardeen's tunneling model [43], yielding the approximation

$$t_{\boldsymbol{k}\boldsymbol{k}'} = -\frac{\hbar^2}{2m}\int d\boldsymbol{r}_\parallel \left[\psi^*_{R\boldsymbol{k}'}(\boldsymbol{r})\partial_z\psi_{L\boldsymbol{k}}(\boldsymbol{r}) - \psi_{L\boldsymbol{k}}(\boldsymbol{r})\partial_z\psi^*_{R\boldsymbol{k}'}(\boldsymbol{r})\right]_{z=d}. \tag{2.4}$$

For a rectangular potential (see Fig. 2.1) the wavefunctions can be readily derived. The exponentially decaying parts are given by are given by

$$\psi_{L\boldsymbol{k}}(\boldsymbol{r}) = \frac{1}{\sqrt{L}}\phi_{L\boldsymbol{k}_\parallel}(\boldsymbol{r}_\parallel)e^{-\kappa(z+d)}. \tag{2.5}$$

Here $\kappa = \frac{\sqrt{2m(U_0-E_z)}}{\hbar}$ is the inverse penetration depth, U_0 is the barrier hight and $E_z = \xi_{\boldsymbol{k}} - \hbar^2\boldsymbol{k}^2_\parallel/2m \ll U_0$ and one immediately finds that

$$t_{\boldsymbol{k}\boldsymbol{k}'} \approx -\frac{\hbar^2}{m}\delta_{\boldsymbol{k}_\parallel,\boldsymbol{k}'_\parallel}\kappa e^{-2\kappa d}, \tag{2.6}$$

where we used the orthogonality condition for the wave-functions $\phi_{r\boldsymbol{k}_\parallel}$. Most electrons that contribute to the transport are those with a wave vector $\boldsymbol{k} = k_z\hat{z}$ perpendicular to the barrier, because of the exponential suppression of $t_{\boldsymbol{k}\boldsymbol{k}'}$ with E_z . In equilibrium, the rate (2.3) can be expressed in terms of the Fermi-Dirac function $f(\xi_{\boldsymbol{k}}) = [\exp(\xi_{\boldsymbol{k}}/k_\mathrm{B}T)+1]^{-1}$ such that

$$\Gamma_{L\to R} = \int d\xi \int d\xi' \mathcal{M}(\xi,\xi') f(\xi)[1-f(\xi')]\delta(\xi-\xi'-eV). \tag{2.7}$$

In the spirit of the Landauer-Büttiker formalism we introduced the transmission function $\mathcal{M}(\xi,\xi') = \frac{2\pi}{\hbar}\sum_{\boldsymbol{k}\boldsymbol{k}'}\delta(\xi-\xi_{\boldsymbol{k}})\delta(\xi'-\xi_{\boldsymbol{k}'})|t_{\boldsymbol{k}\boldsymbol{k}'}|^2$. Because we act on the assumption that

$k_{\mathrm{B}}T,\, eV \ll \xi, \xi' \sim E_F$ the energy dependence of $\mathcal{M}$ in (2.7) can be neglected. Moreover, because electrons in forward direction contribute most we may apply the approximation

$$\mathcal{M}(\xi,\xi') \sim \sum_{\boldsymbol{k}_\parallel} e^{-4d\sqrt{\frac{2m}{\hbar^2}(U_0-E_F+\hbar^2\boldsymbol{k}_\parallel^2/2m)}} \approx \sum_{\boldsymbol{k}_\parallel} e^{-4d\sqrt{\frac{2m}{\hbar^2}(U_0-E_F)}} e^{-2d\sqrt{\frac{\hbar^2}{2m(U_0-E_F)}}\boldsymbol{k}_\parallel^2}. \tag{2.8}$$

The transmission function may be expressed by an effective transmission coefficient

$$\mathcal{T} = \frac{2^2 R_K}{4\pi} e^{-4d\sqrt{\frac{2m}{\hbar^2}(U_0-E_F)}}, \tag{2.9}$$

where $R_K = 2\pi\hbar/e^2 \approx 25.8\,\mathrm{k\Omega}$ is the von Klitzing constant. Then, the number of associated transmission channels of the barrier is given by

$$N \approx \sum_{\boldsymbol{k}_\parallel} e^{-2d\sqrt{\frac{\hbar^2}{2m(U_0-E_F)}}\boldsymbol{k}_\parallel^2} \approx \frac{A}{4\pi d}\sqrt{\frac{2m}{\hbar^2}(U_0-E_F)}\,, \tag{2.10}$$

Here A is the area of junction and d its thickness. Therewith the transmission function can be written as

$$\mathcal{M} = \frac{4\pi}{e^2 R_K} N\mathcal{T}\,. \tag{2.11}$$

In the following we will exclusively consider the weak tunneling limit, i.e. $N\mathcal{T} \ll 1$ or equivalently $R_T^{-1} \ll R_K^{-1}$. Here $R_T = R_K/4\pi N\mathcal{T}$ defines the effective tunneling-resistance. The number of channels per unit area can be estimated assuming that $(U_0 - E_F) \sim \mathrm{eV}$ and $d \sim \mathrm{nm}$ giving $N/A \sim 0.5\,\mathrm{nm}^{-2}$. Though, the experimentally determined effective number of channels per unit area N/A may be an order of magnitude smaller. Variations in the barrier thickness are plausible explanations for this observation [44].

2.1. Charging effects

In this chapter we will discuss setups involving small metallic islands, where the change of the electrostatic potential due to the tunneling of a single-electron onto it can be large enough to affect the tunneling-rates. This *charging effect* has been first observed in granular metallic films [45] where the tunneling from grain to grain is blocked, if the charging energy

$$E_C = \frac{e^2}{2C} \tag{2.12}$$

of a single-electron on a grain with capacitance C exceeds the thermal energy $k_{\mathrm{B}}T$. The characteristic time-scale for such a tunneling process is given by $\tau = R_T C$. The time-uncertainty associated with (2.12) has to be smaller than this time-scale, i.e. $\tau E_C \gg 1$, which is equivalent to the weak-tunneling condition $R_T^{-1} \ll R_K^{-1}$.

Nowadays metallic islands can be produced with known geometry and controlled system parameters. Islands with a capacitance $C \sim 10^{-15}\,\mathrm{F}$ are accessible, which corresponds to a temperature-scale of $E_C/k_{\mathrm{B}} \sim 1\,\mathrm{K}$ below which charging effects can be observed [46]. By capacitively coupling an island to control gates the charge on the island can be

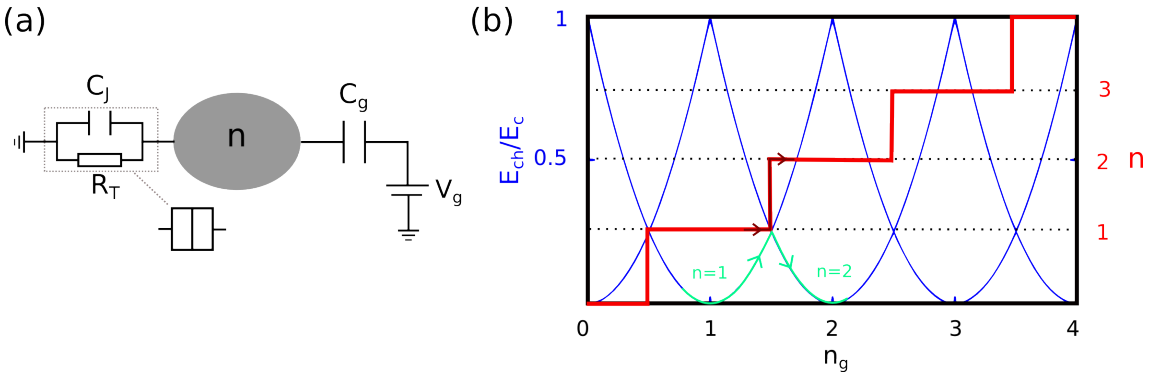

Figure 2.2.: (a) Circuit diagram of the single-electron box. (b) Charging energy E_{ch} and excess charge n as a function of normalized gate voltage n_g.

changed in a reliable way. Moreover imposing a voltage to leads that are attached by tunneling junctions permits a controllable sequential transfer of single-electrons.

An illustrative example of a controllable single-electron device is the *single-electron box*. A small island is coupled at the left hand site to a lead via a tunnel junction with capacitance C_J and resistance R_T [see Fig. 2.2(a)]. At the right hand site it is capacitively coupled to a gate-voltage V_g via the gate-capacity C_g. The net excess charge on the island in units of the elementary charge e is given by $-ne = Q_L + Q_R$, where $Q_{L,R}$ are the charges on the left and right capacitor plates. The voltage applied from the voltage source is given by $V_g = Q_L/C_J - Q_R/C_g$. The free energy of the system results from the charging energy as well as the work applied by the voltage source, i.e.

$$F(n) = \frac{Q_L^2}{2C_J} + \frac{Q_R^2}{2C_g} + Q_g V_g = \frac{(ne - Q_g)^2}{2C} - \frac{Q_g^2}{2C} + \frac{C_J Q_g V_g}{2C}. \tag{2.13}$$

We will neglect the terms independent of excess charge n in the following and refer to

$$E_{ch}(n) = \frac{(ne - Q_g)^2}{2C} \tag{2.14}$$

as the charging energy. Here $C = C_J + C_g$ is the total island-capacitance and $Q_g = C_g V_g$ is the *gate-charge*. Because $Q_g = n_g e$ is only a redefinition of the gate-voltage it can be varied in a continuous fashion leading to the energy-landscape shown in Fig. 2.2(b). If we are originally in the *charging state* $n = 1$ and we ramp up the gate voltage a transition into the charging state $n = 2$ happens right at the degeneracy-point $n_g = 1.5$, where $E_{ch}(n = 1) = E_{ch}(n = 2)$. Increasing the gate-voltage even further leads to the step-like increase of the excess charge n on the island, the so-called *Coulomb-staircase*.

2.2. Single-electron transistor

A controlled transport of single charges can be achieved with the *single-electron transistor* setup shown in Fig. 2.3(a). A metallic island is connected to a left (L) and right metallic lead (R) via tunnel junctions and is capacitively coupled to a gate. First let us consider

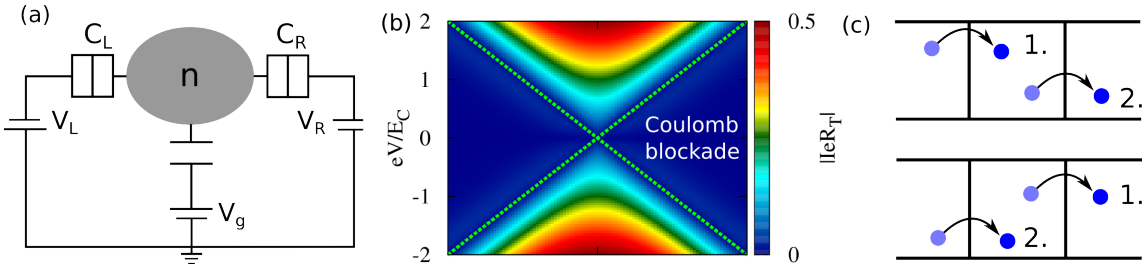

Figure 2.3.: (a) Circuit diagram of the single-electron transistor. (b) Current 2.18 as a function of gate-voltage n_g for symmetric bias $V_L = -V_R = V/2$. Green lines indicate the condition (2.15). (c) Cotunneling processes that become important in the Coulomb-blockade region.

the case, where the island and the leads are normal metals. At $T = 0$ electronic transport from left to right is prohibited unless it is energetically allowed,

$$eV_L > E_{ch}(n+1) - E_{ch}(n) > eV_R \tag{2.15}$$

This phenomenon is called *Coulomb blockade* and it has significant impact on the transport characteristics. The difference $E_{ch}(n+1) - E_{ch}(n) = 2E_C\left(n + \frac{1}{2} - n_g\right)$ depends on gate-voltage providing an handle on the single-electron transport.

The corresponding rate for the tunneling of a single electron from the lead $r\,(= L,\, R)$ onto the island, changing the charging state from n to $n+1$, can be derived in terms of Fermi's golden rule, yielding [46]

$$\Gamma^r_{n+1,n} = \frac{1}{e^2 R^r_T} \frac{\delta E^r_{ch}(n)}{\exp[\delta E^r_{ch}(n)/k_{\mathrm{B}}T] + 1}, \tag{2.16}$$

where $\delta E^r_{ch} = E_{ch}(n+1) - E_{ch}(n) - eV_r$ is the energy gain by the tunneling process. In order to derive the current-voltage characteristics let us assume that $ne < Q_g < (n+1)e$, meaning that only two charging states are important. From a statistical point of view the ratio of probabilities p_n to have n excess charges on the island is given by the detailed balance relation

$$\frac{p_{n+1}}{p_n} = \frac{\Gamma_{n+1,n}}{\Gamma_{n,n+1}}, \tag{2.17}$$

where $\Gamma_{n+1,n} = \sum_{r=L,R} \Gamma^r_{n+1,n}$. The current through the r-th lead can be derived from the occupation probabilities giving

$$I_r = -e(\Gamma^r_{n+1,n} p_n - \Gamma^r_{n,n+1} p_{n+1}) = -e \frac{\Gamma^{\bar{r}}_{n,n+1}\Gamma^r_{n+1,n} - \Gamma^{\bar{r}}_{n+1,n}\Gamma^r_{n,n+1}}{\Gamma_{n+1,n} + \Gamma_{n,n+1}}, \tag{2.18}$$

where $\bar{L} = R$ and vise versa. In Fig. 2.3(b) the current is shown as a function of gate voltage and bias voltage. Single-electron tunneling is suppressed within the Coulomb-blockade. The condition (2.15) is indicated by green lines. In this regime higher order processes like inelastic co-tunneling become important [47]. In this process an electron first tunnels from the left lead onto the island and then from the island to the right lead or it first tunnels to the right lead leaving behind a hole on the island before another electron from the left tunnels onto the island (see Fig. 2.3(c)). After the tunneling process an

electron-hole excitation is left on the island which is why this process is called *inelastic co-tunneling*. At $T = 0$ the corresponding tunneling rate can be derived analytically, [47]

$$\Gamma^{\mathrm{cot}}_{L\to R} = \frac{\hbar}{12\pi e^4 R_T^L R_T^R}\left[\frac{1}{\delta E^L_{ch}} + \frac{1}{\delta E^R_{ch}}\right]^2 (eV)^3\,, \tag{2.19}$$

where $\delta E^L_{ch}(n) = E_{ch}(n+1) - E_{ch}(n) - eV_L$ and $\delta E^R_{ch} = E_{ch}(n-1) - E_{ch}(n) + eV_R$ is the energy gain for each intermediate tunneling event and $eV = eV_L - eV_R$ is the voltage difference between left and right lead. Although co-tunneling is suppressed by an additional factor R_K/R_T it becomes important at small temperatures where sequential tunneling is prohibited.

Superconducting single-electron transistor

Now we consider a normal-metal – superconductor – normal-metal (NSN) single-electron transistor. In the case of a superconducting island things change. First of all one may expect that single electron tunneling is suppressed below a bias voltage 2Δ because of the gap in the superconducting density of states. However there are several contributions to the *subgap* current, such as the parity effect or the Andreev tunneling. The tunneling of charge is associated with the creation and annihilation of quasiparticles and corresponds to the tunneling Hamiltonian

$$H_T = \sum_{r\boldsymbol{k}\boldsymbol{k}'\sigma} t^r_{\boldsymbol{k}\boldsymbol{k}'}\, c^\dagger_{r\boldsymbol{k}'\sigma}(u_{\boldsymbol{k}}\gamma_{\boldsymbol{k}\sigma} + \sigma v_{\boldsymbol{k}}\overline{\gamma}^\dagger_{\boldsymbol{k}\sigma}) + H.c. \tag{2.20}$$

where we introduced the *time-reversed* quasiparticle operator $\overline{\gamma}_{\boldsymbol{k}\sigma} = \gamma_{-\boldsymbol{k},-\sigma}$. The excitation of quasiparticles and holes comes along with respective coherence factors $u^2_{\boldsymbol{k}}$ and $v^2_{\boldsymbol{k}}$. The sequential tunneling-rates for the tunneling of an electron from lead r on the island are given by

$$\begin{aligned}\Gamma^r_{n+1,n} = &\frac{1}{2e^2R^r_T}\int_{-\infty}^{\infty} d\xi\,\left(1+\frac{\xi}{E}\right) f^r[E+\delta E^r_{ch}(n)](1-f_\xi)\\ &+\frac{1}{2e^2R^r_T}\int_{-\infty}^{\infty} d\xi\,\left(1-\frac{\xi}{E}\right) f^r[-E+\delta E^r_{ch}(n)]f_{-\xi}.\end{aligned} \tag{2.21}$$

Here we introduced the energy dependent quasiparticle distribution function

$$f_\xi = \frac{1}{\mathcal{N}_F\mathcal{V}}\sum_{\boldsymbol{k}\sigma}\langle\gamma^\dagger_{\boldsymbol{k}\sigma}\gamma_{\boldsymbol{k}\sigma}\rangle\,\delta(\xi-\xi_{\boldsymbol{k}}). \tag{2.22}$$

Furthermore $E = \sqrt{\xi^2+\Delta^2}$ are the quasiparticle energies. In the most general case $f_\xi \neq f_{-\xi}$, meaning that the superconductor has more quasiparticle than hole excitations or vise versa, known as *charge imbalance*. Considering the total electronic charge on the island, i.e.

$$Q = -e\sum_{\boldsymbol{k}\sigma}\langle c^\dagger_{\boldsymbol{k}\sigma}c_{\boldsymbol{k}\sigma}\rangle = -e\sum_{\boldsymbol{k}\sigma}v^2_{\boldsymbol{k}} - e\sum_{\boldsymbol{k}\sigma}[u^2_{\boldsymbol{k}}-v^2_{\boldsymbol{k}}]\,\langle\gamma^\dagger_{\boldsymbol{k}\sigma}\gamma_{\boldsymbol{k}\sigma}\rangle\,, \tag{2.23}$$

the first term corresponds to the charge of Cooper pairs whereas the latter term is the *quasiparticle charge density*

$$Q^* = \mathcal{N}_F\mathcal{V}\int_{-\infty}^{\infty} d\xi\frac{\xi}{E}f_\xi. \tag{2.24}$$

If the charge relaxation is fast the charge imbalance vanishes, i.e. $Q^* \approx 0$. This is for instance the case in equilibrium, where f_ξ is given by the Fermi-distribution $f(E) = [\exp(E/k_\mathrm{B}T)+1]^{-1}$. In this case Eq. (2.21) can be recast in the form

$$\Gamma^r_{n+1,n} = \frac{1}{e^2 R^r_T}\int_{-\infty}^{\infty} dE\,\rho(E) f^r[E+\delta E^r_{ch}(n)](1-f(E)), \tag{2.25}$$

where $\rho(E) = \mathrm{sgn}(E)\mathrm{Re}\{E/\sqrt{E^2-\Delta^2}\}$ is the normalized density of states. Eq. (2.25) tells that for $T=0$ sequential tunneling is prohibited if $\Delta + \delta E^r_{ch}(n) > 0$. Nevertheless there are other phenomena contributing an additional subgap current, such as the parity effect which will be the topic of the next paragraph.

Parity effect

Generally parity effects matter in systems, where the number of degrees of freedoms is small, like for instance concerning the binding energy of nuclei. Furthermore parity effects are important even in small superconducting islands, although the number of electrons is large ($N \gtrsim 10^7$) [11, 48, 49, 50]. Here the charging energy fixes the number of electrons to be even or odd. At low temperatures this has the apparent consequence that in the odd charging state there is always one remaining quasiparticle which cannot recombine into a Cooper-pair. In the NSN single-electron transistor this leads to a non-vanishing quasiparticle current $I = \delta/eR_T$, where $\delta = 1/\mathcal{N}_F\mathcal{V}$ is the mean level spacing.

In order to treat this problem in an accurate way one would have to work in the canonical statistical ensemble. However, because the number of electrons in a metallic island is so large and therefore the level spacing δ so small, all thermodynamic quantities just depend on the parity of the electron number. Therefore it is sufficient to keep track of the parity by applying a grand-canonical ensemble.

The quasiparticle distribution

Starting from the quasiparticle Hamiltonian (1.23) the density of quasiparticles in a grand-canonical ensemble is given by

$$\hat{\rho}_{qp} = \exp\left(-\frac{H_{qp}}{k_B T}\right) = \prod_{\boldsymbol{k}\sigma}\left[(1-f(E_{\boldsymbol{k}}))(1-\hat{n}_{\boldsymbol{k}\sigma}) + f(E_{\boldsymbol{k}})\hat{n}_{\boldsymbol{k}\sigma}\right]. \tag{2.26}$$

Here the occupation-operator of the state with momentum $\boldsymbol{k}$ and spin σ is given by $\hat{n}_{\boldsymbol{k}\sigma} = \gamma^\dagger_{\boldsymbol{k}\sigma}\gamma_{\boldsymbol{k}\sigma}$ and $f(E)$ is the Fermi-Dirac distribution. Mind that the parity of the electron-number $\hat{N}_\mathrm{el} = \sum_{\boldsymbol{k}\sigma} c^\dagger_{\boldsymbol{k}\sigma}c_{\boldsymbol{k}\sigma}$ and quasiparticle-number $\hat{N}_\mathrm{qp} = \sum_{\boldsymbol{k}\sigma}\hat{n}_{\boldsymbol{k}\sigma}$ is the same. Therefore we may define the operator

$$\hat{P}^\pm = \frac{1}{\sqrt{2}}\left[1\pm(-1)^{\hat{N}_\mathrm{qp}}\right] = \frac{1}{\sqrt{2}}\left[1\pm\prod_{\boldsymbol{k}\sigma}(1-2\hat{n}_{\boldsymbol{k}\sigma})\right] \tag{2.27}$$

which is a projection-operator onto even $(+)$ and odd $(-)$ parity subspace. According to that the *parity projected* density matrix is given by [51],

$$\hat{\rho}^{n=\mathrm{even/odd}}_{qp} = \frac{\hat{P}^\pm\hat{\rho}_{qp}}{\mathrm{Tr}(\hat{P}^\pm\hat{\rho}_{qp})}. \tag{2.28}$$

As a next step we calculate the quasiparticle distribution in the even and odd parity state, i.e.

$$\langle \hat{n}_{\boldsymbol{k}\sigma} \rangle_{\mathrm{even/odd}} = \mathrm{Tr}(\hat{n}_{\boldsymbol{k}\sigma} \hat{\rho}_{qp}^{\mathrm{even/odd}}). \tag{2.29}$$

To this end mind that the projection operator $\hat{P}^{\pm}$ does not commute with the occupation operator $\hat{n}_{\boldsymbol{k}\sigma}$ and gives

$$\hat{P}^{\pm} \hat{n}_{\boldsymbol{k}\sigma} = \hat{n}_{\boldsymbol{k}\sigma} \frac{1}{\sqrt{2}} \left[1 \mp \prod_{\boldsymbol{q}\alpha \neq \boldsymbol{k}\sigma} (1 - 2\hat{n}_{\boldsymbol{q}\alpha}) \right]. \tag{2.30}$$

With this the parity dependent quasiparticle occupation is given by

$$\langle \hat{n}_{\boldsymbol{k}\sigma} \rangle_{\mathrm{even/odd}} = f(E_{\boldsymbol{k}}) \mathcal{A}_{\mathrm{even/odd}}^{\boldsymbol{k}\sigma} \tag{2.31}$$

The parity dependent coefficient $\mathcal{A}_n^{\boldsymbol{k}\sigma}$ can be directly derived from (2.30) yielding

$$\mathcal{A}_{\mathrm{even/odd}}^{\boldsymbol{k}\sigma} = \frac{1 \mp \prod_{\boldsymbol{p}\alpha \neq \boldsymbol{k}\sigma} (1 - 2f(E_{\boldsymbol{p}}))}{1 \pm \prod_{\boldsymbol{p}\alpha} (1 - 2f(E_{\boldsymbol{p}}))}. \tag{2.32}$$

Because in a metallic island the level-spacing δ is typically much smaller than the thermal energy $k_{\mathrm{B}}T$, the dependence of $\mathcal{A}_n^{\boldsymbol{k}\sigma}$ on the state $(\boldsymbol{k}\sigma)$ can be neglected. Furthermore the temperatures that we are considering are small, such that $f(E_{\boldsymbol{k}}) \ll 1$. This gives the rather simple expression

$$\mathcal{A}_n = \begin{cases} \tanh\left[\sum_{k\sigma} f(E_{\boldsymbol{k}})\right], & n = \text{even} \\ \coth\left[\sum_{k\sigma} f(E_{\boldsymbol{k}})\right], & n = \text{odd} \end{cases}, \tag{2.33}$$

which exclusively depends on the number of thermally excited quasiparticles,

$$\begin{aligned} N_{\mathrm{qp}} &= \sum_{\boldsymbol{k}\sigma} f(E_{\boldsymbol{k}}) \\ &\approx \sqrt{2\pi} \mathcal{N}_F \mathcal{V} \sqrt{\Delta k_{\mathrm{B}} T} \exp(-\Delta / k_{\mathrm{B}} T). \end{aligned} \tag{2.34}$$

The last line is a valid approximation as long as the temperature is low, i.e. $T \ll \Delta / k_{\mathrm{B}}$. Mind that for $T \to 0$ the number of thermal excitations N_{qp} goes to zero. Accordingly the coefficient $\mathcal{A}_n$ either diverges or it vanishes, depending on whether n is odd or even. Nevertheless the number of quasiparticles remains finite. In the zero temperature limit we find

$$\begin{aligned} \sum_{\boldsymbol{k}\sigma} \langle \hat{n}_{\boldsymbol{k}\sigma} \rangle_{\mathrm{even}} &\approx \sum_{\boldsymbol{k}\sigma} f(E_{\boldsymbol{k}}) N_{\mathrm{qp}} = N_{\mathrm{qp}}^2 \,, \\ \sum_{\boldsymbol{k}\sigma} \langle \hat{n}_{\boldsymbol{k}\sigma} \rangle_{\mathrm{odd}} &\approx \sum_{\boldsymbol{k}\sigma} f(E_{\boldsymbol{k}}) N_{\mathrm{qp}}^{-1} = 1 \,. \end{aligned} \tag{2.35}$$

This means that there is always one quasiparticle remaining in the odd parity subspace. At finite temperature the quasiparticle distribution (2.31) may be parametrized by a shift of the chemical potential [46]. For $T \ll \Delta / k_{\mathrm{B}}$ we obtain $f_{\boldsymbol{k}} \mathcal{A}_{\mathrm{odd}} \approx \exp(-[E_{\boldsymbol{k}} - \mu_n]/k_{\mathrm{B}}T)$ and with this

$$\mu_{\mathrm{odd}} = k_{\mathrm{B}} T \, \ln(\mathcal{A}_{\mathrm{odd}}). \tag{2.36}$$

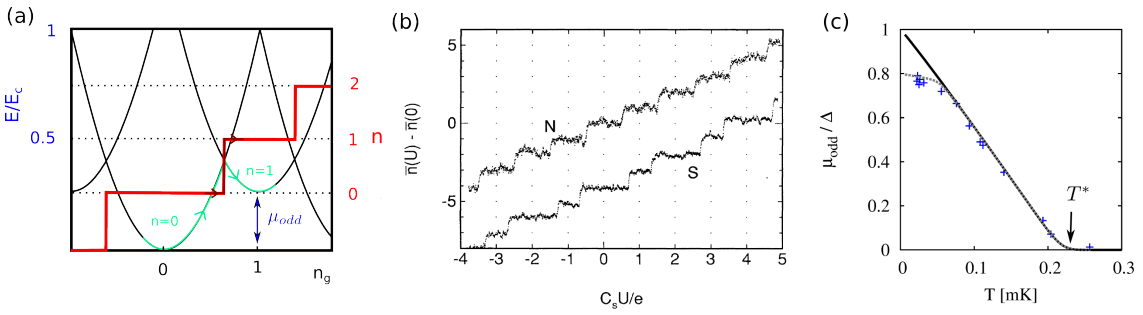

Figure 2.4.: (a) Coulomb staircase in the superconducting case. Due to the additional shift by μ_{odd} the width of the associated plateau in the odd charging sate decreases. (b) Measured coulomb staircase for the normal (N) and superconducting case (S). Figure from Ref. [48]. (c) μ_{odd} as a function of temperature: The black line only incorporates thermally excited quasiparticles above gap, whereas the gray dashed line incorporates an additional energy level at $\varepsilon_b = 0.8\,\Delta$. The experimental data points as well the material parameters for the theoretical lines are adopted from Ref. [48].

This shift of the chemical potential exactly corresponds to the difference of the grand canonical potential in the even and odd state. To see this, we observe that the partition function in the even and odd state is given by $Z_{\text{even/odd}} = \text{Tr}(\hat{P}^{\pm}\hat{\rho}_{qp})\, Z_0/\sqrt{2}$, where $Z_0 = \text{Tr}[\exp(H_{qp}/k_\text{B}T)]$ is the partition function in the parity unprojected case. With this we obtain

$$\begin{aligned}\Omega_\text{odd} - \Omega_\text{even} &= -k_\text{B}T\ln(Z_\text{odd}) + k_\text{B}T\ln(Z_\text{even}) \\ &= -k_\text{B}T\ln\left(\frac{1+\prod_{\boldsymbol{k}\sigma}(1-2f(E_{\boldsymbol{k}}))}{1-\prod_{\boldsymbol{p}\alpha}(1-2f(E_{\boldsymbol{p}}))}\right) \\ &\approx k_\text{B}T\ln\left(\mathcal{A}_\text{odd}\right), \end{aligned} \tag{2.37}$$

which is identical to Eq. (2.36).

One of the first experiments identifying the parity effect was performed by Lafarge *et al.*[48] using a superconducting single electron box. In Fig. 2.4(a) we illustrate the measuring principle: As discussed before the difference in the energies of the even and odd charging state is given by μ_odd in Eq. (2.36). This shift becomes visible in a variation of the step-widths in the Coulomb-stairs from which μ_odd can be directly inferred. Fig. 2.4(b) shows the respective data of Ref. [48] and panel (c) the extracted potential shift. Furthermore we compare μ_odd (black line) with the experimental data but find a mismatch at low temperatures. The authors of Ref. [48] argue that this deviation may be attributed to a two-fold subgap state with energy $\varepsilon_b = 0.8\Delta$. In order to incorporate this additional level in our model we recapitulate the approximation done right after Eq. (2.32). Because $\delta \ll k_\text{B}T \ll \Delta - \varepsilon_b$ the coefficient (2.32) now explicitly depends on the subgap energy-state, i.e.

$$\mathcal{A}^b_{odd} \approx \frac{\cosh(N_\text{qp})}{\sinh(N_\text{qp}) + 2e^{-\varepsilon_b/k_\text{B}T}e^{-N_\text{qp}}}. \tag{2.38}$$

The corresponding shift in chemical potential is shown by the gray dashed line in Fig. 2.4(c) and reproduces the theoretical results derived in Ref. [48]. The parity effect disappears at a characteristic crossover-temperature T^*.

The superconducting gap

So far we ignored the effect of parity on the superconducting gap. Concerning the BCS gap-equation the parity should also imprint on the value of the superconducting gap [51, 52], i.e.

$$\Delta_{\mathrm{even/odd}} = g^2 \sum_{\boldsymbol{k}} \frac{\Delta_{\mathrm{even/odd}}}{2E_{\boldsymbol{k}}} \left[1 - 2f(E_{\boldsymbol{k}})\mathcal{A}_{\mathrm{even/odd}}\right].$$

In the limit $k_{\mathrm{B}}T/\Delta \ll 1$, linearizing the parity dependent gap, i.e. $\Delta_{\mathrm{even/odd}} = \Delta + \delta\Delta_{\mathrm{even/odd}}$, where Δ is the BCS-gap solution for $T = 0$, we approximately obtain

$$\frac{\delta\Delta_{\mathrm{even/odd}}}{\Delta} \approx -\frac{2N_{\mathrm{qp}}}{\mathcal{N}_F\mathcal{V}\Delta}\left[\tanh(N_{\mathrm{qp}})\right]^{\pm 1} \approx -\begin{cases} 4\pi\mathcal{N}_F\mathcal{V}k_{\mathrm{B}}T\exp\left(-\frac{2\Delta}{k_{\mathrm{B}}T}\right) + \cdots \\ \frac{2}{\mathcal{N}_F\mathcal{V}\Delta} + \frac{4}{3}\pi\mathcal{N}_F\mathcal{V}k_{\mathrm{B}}T\exp\left(-\frac{2\Delta}{k_{\mathrm{B}}T}\right) + \cdots \end{cases} \tag{2.39}$$

in agreement with Refs. [51, 52]. Due to the small level-spacing $\delta \sim 1/\mathcal{N}_F\mathcal{V} \ll 1$ this correction is negligible small and we can ignore it in the following.

Single-electron tunneling rates

Due to the modulation of the quasiparticle distribution, which now depends on the parity of the charging state (see Eq. (2.31)) the tunneling-rates are given by

$$\begin{aligned}\Gamma^r_{n+1,n} &= \frac{1}{e^2R^r_T}\int_{-\infty}^{\infty} dE\,\rho(E)f^r[E + \delta E^r_{ch}(n)]\{1 - f[E - \mathrm{sgn}(E)\mu_n]\},\\ \Gamma^r_{n,n+1} &= \frac{1}{e^2R^r_T}\int_{-\infty}^{\infty} dE\,\rho(E)\{1 - f^r[E + \delta E^r_{ch}(n)]\}f[E - \mathrm{sgn}(E)\mu_{n+1}].\end{aligned} \tag{2.40}$$

For $T \to 0$ one observes a non-vanishing contribution to the odd to even transition rate and therefore a finite current which is carried by the unpaired quasiparticle, i.e.

$$I_{\mathrm{parity}} = \frac{1}{2\mathcal{N}_F\mathcal{V}eR^r_T}. \tag{2.41}$$

In experiment this additional contribution appears as a finite current plateau at odd gate charge and at subgap bias voltage.

I-V characteristics

In Fig. 2.5(a) we show the current versus bias and gate-voltage characteristics that has been recently measured for a NSN transistor with $\Delta < E_C$ [9]. It bears several features that can be attributed to different tunneling processes. First of all, single-electron tunneling is suppressed for $\Delta + \delta E^r_{ch}(n) > 0$. This condition is indicated by the Coulomb diamonds for charging states with $n = 0$ and $n = 1$ (dashed white curves).

At odd gate offsets the quasiparticle in the odd charging state leads to an additional, 2e-periodic, current in the subgap region with the amplitude I_{parity} given in Eq. (2.41). In this process an unpaired electron tunnels from the island into the right lead with an escape-rate $\gamma_{\mathrm{esc}} = I_{\mathrm{parity}}/e$, changing the charging state of the island from odd to even. The expense of charging energy is reflected in the tunneling rate $\Gamma^L_{\mathrm{even}\to\mathrm{odd}}$ which is much larger than the escape rate γ_{esc}. This means that an quasiparticle state on the island is immediately

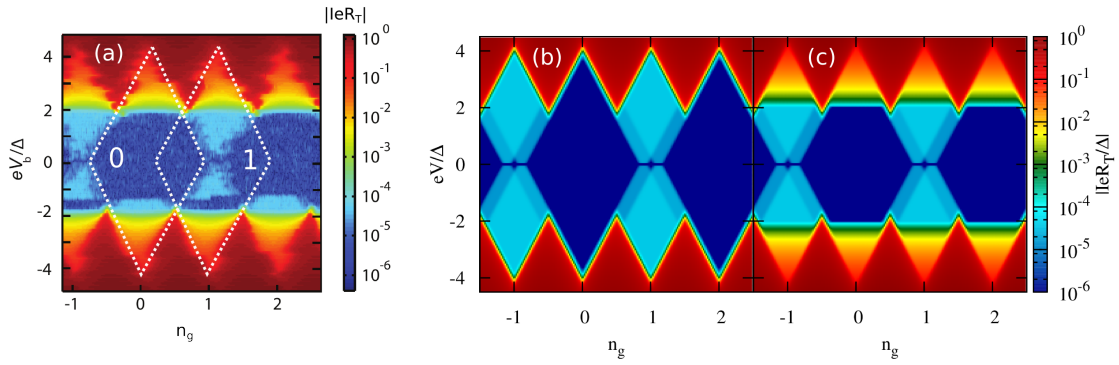

Figure 2.5.: Stability diagram: Current I versus bias eV and gate-charge en_g. (a) Stability diagram from Ref. [9] with slight modifications: The current clearly shows the 2-e periodicity in the subgap region $|eV| < 2\Delta$. (b) Single-electron tunneling: Simulated current using the sequential tunneling-rates (2.40) and experimental parameters from Ref. [9] ($\Delta = 210\,\mu\text{eV}$, $E_C = 240\,\mu\text{eV}$, $R_T \sim 0.1\,\text{M}\Omega$, $T = 60\,\text{mK}$). (c) Cotunneling: Simulated current including the incoherent co-tunneling rate (2.43).

filled by an electron tunneling from the left lead onto it once the quasiparticle escaped from the island. Thus, one could say that a quasiparticle is trapped in the odd-charging state.

In Fig. 2.5(b) the corresponding theoretical curves are shown that rely on the sequential tunneling approximation (2.40) (experimental parameters have been taken from Ref. [9], furthermore we introduced a lower cutoff for the current $I \sim 10^{-6}\,\Delta/eR_T$ corresponding to the residual current observed in experiment). Indeed the simulations account for the current that can be attributed to single-electron tunneling events. Nevertheless, the data shows an additional current within the Coulomb-blockaded region at bias voltages $eV > 2\Delta$. Incoherent co-tunneling is a process, which can lead to such a contribution and happens at a rate

$$\Gamma^{\text{cot}} \sim \frac{\hbar}{2\pi e^4 R_T^L R_T^R} \int_{-\infty}^{\infty} d\xi_1 \int_{-\infty}^{\infty} dE_2 \int_{-\infty}^{\infty} dE_3 \int_{-\infty}^{\infty} d\xi_4 \left[\frac{1}{E_2 - \xi_1 + \delta E_{ch}^L} + \frac{1}{\xi_4 - E_3 + \delta E_{ch}^R} \right]^2 \times f(\xi_1)[1 - f(E_2)] f(E_3)[1 - f(\xi_4)]\, \rho(E_2)\rho(E_3)\, \delta(\xi_1 - \xi_4 + E_3 - E_2 + eV). \tag{2.42}$$

In order to give a rough estimate we neglect coherence factors. At $T = 0$ this rate is suppressed at $0 < eV < 2\Delta$. Slightly above this threshold the co-tunneling rate at $n_g \in \mathbb{Z}$ is approximately given by

$$\Gamma^{\text{cot}} \sim \frac{R_K}{e^2 R_T^L R_T^R} \sqrt{2} \frac{\Delta^{3/2}(eV - 2\Delta)^{3/2}}{E_C^2} \tag{2.43}$$

Fig. 2.5(c) shows the simulated current including this additional contribution (2.43).

In single-electron transistors where the charging energy is small, i.e. $E_C < \Delta$, single-charge tunneling is suppressed for bias voltages $eV < 2(\Delta - E_C)$. Nonetheless higher-order processes like Andreev-reflection become important. In such a process an incident

electron from the left lead is reflected into a hole changing the charging state on the island from n to $n+2$. This process happens predominantly at odd gate-charge offset where the two even charging states states n and $n+2$ are degenerate. For small temperatures and bias voltage, $k_{\mathrm{B}}T,\ eV \ll E_C$ the associated rate is given by [53]

$$\Gamma_L^A = \frac{G_A}{e^2} \frac{\delta E_{ch}^{(2)}}{\exp(\delta E_{ch}^{(2)}/k_{\mathrm{B}}T) - 1}\,, \tag{2.44}$$

This is similar to the normal state result in Eq. (2.16) but with a different prefactor. The Andreev-conductance $G_A \sim (R_K/R_T^2 N)$ explicitly depends on the number of independent parallel channels, N [see Eq. (2.10)]. At $n_g = \mathrm{odd}$ the current increases linearly in bias voltage, but suddenly drops down to I_{parity} when single quasiparticle tunneling becomes allowed. This happens at the threshold $eV = 2(\Delta - E_C)$. Above this threshold the even to odd transition rate $\Gamma_{\mathrm{even}\to\mathrm{odd}}$ is way larger than the Andreev-rate (2.44), i.e. $\Gamma_{\mathrm{even}\to\mathrm{odd}} \gg \Gamma^A$. According to that a quasiparticle becomes trapped in the odd charging state, contributing with the escape-rate γ_{esc} to the current.

Another co-tunneling process which is important in the subgap-regime, even if $\Delta < E_C$ is the coherent tunneling of a Cooper-pair via Andreev-reflection at one junction and a tunneling of an electron at the other, which appears at a threshold-voltage of $eV = \frac{2}{3}[\Delta + E_{ch}(n+1) - E_{ch}(n)]$ [54]. The associated conductance scales with $G_{\mathrm{CPE}} \sim (R_K^2/R_T^3 N)$. These estimates will be important in the next chapter and we will come back to this point, when we discuss the potential error-sources that limit the accuracy of single-electron turnstiles.

3. Non-equilibrium quasiparticles in a hybrid single-electron turnstile

The excitation of non-equilibrium quasiparticles in superconducting devices by external fields has been investigated already for decades. For instance, it has been shown that by applying strong ac-radiation the quasiparticle distribution $f_{\boldsymbol{k}\sigma} = \langle \gamma^{\dagger}_{\boldsymbol{k}\sigma} \gamma_{\boldsymbol{k}\sigma} \rangle$ of a superconductor can be modified in such a way both the critical current [55] and the superconducting gap [56, 57, 58] may be enhanced [see Fig. 3.1(a)]. Here quasiparticles living at the gap-edge populate higher states by absorption of ac-radiation. This reduces the population at the gap and according to Eq. (1.24) favors an increase of the superconducting order parameter. Furthermore, it has been demonstrated in Refs. [59, 60] that the application of a dc bias voltage to a normal-metal – superconductor (NS) junction leads to electronic cooling of the normal metallic side and therewith to *overheating* of the superconductor (see Fig. 3.1).

More recently, the issue of non-equilibrium quasiparticles has drawn renewed attention in the context of superconducting qubits [2, 3, 5, 6]. Here quasiparticle-tunneling through Josephson-junctions couples to the phase of the qubit and leads to decoherence. It is straightforward to show that the relaxation rate is proportional to the density of quasiparticles, $n_{qp} = N_{qp}/\mathcal{V}$, i.e.

$$\Gamma_{\downarrow} \sim \frac{\Delta}{e^2 R_T} \frac{n_{qp}}{n_{cp}}. \tag{3.1}$$

Recently Wenner *et al.*[3] demonstrated experimentally that this proportionality holds approximately well in a wide range of quasiparticle densities [see e.g. Fig. 3.1 (c)].

Similarly non-equilibrium quasiparticles limit the accuracy of hybrid single-electron turnstiles that are promising candidates for a future current standard [7, 8, 9]. In these setups the excitation of quasiparticles unavoidably comes along with the tunneling of charge. One can distinguish two different configurations: In a SNS turnstile the normal conducting island is electronically cooled by the superconducting leads, whereas the NSN turnstile suffers from weak quasiparticle relaxation in the small superconducting island. Because of that the SNS-turnstile is the preferred device for metrological applications. The ultra sensitive counting scheme used in turnstile experiments allows for tracking of

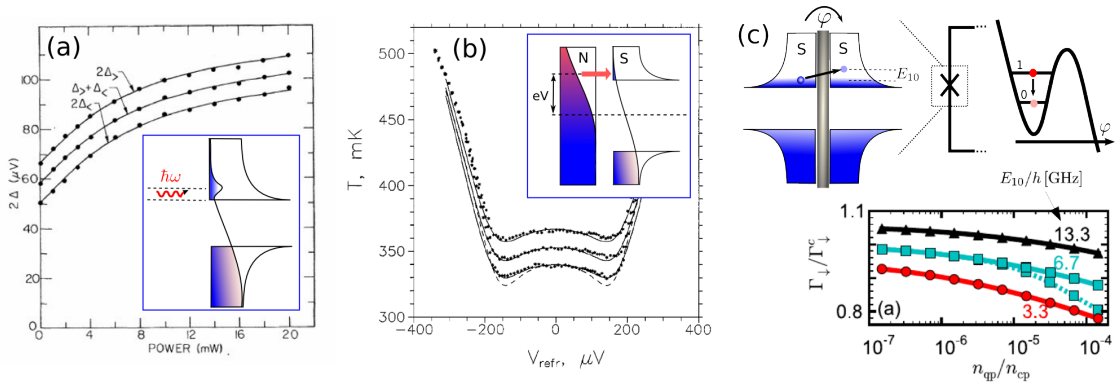

Figure 3.1.: Non-equilibrium quasiparticles in superconducting devices: (a) Ac-radiation with energy $\hbar\omega$ leads to a population of states at energies $\sim \Delta + \hbar\omega$. The suppression of the quasiparticle population close to the gap favours an increase of the superconducting gap. The experimental plot shows the superconducting gap as a function of radiation power. (The Figure is taken from Ref. [56] and the illustration has been added). (b) An applied dc bias voltage at an NS tunnel-junction leads to an extraction of *hot* quasiparticles from the normal side. The experimental curves show the measured electronic temperature as a function of bias voltage. (The Figure is taken from Ref. [60] and the illustration has been added) (c) Quasiparticle-tunneling in Josephson-junctions couples to the superconducting phase and thus to the qubit degrees of freedom. A qubit relaxes from the excited to the ground-state and simultaneously the quasiparticle gains energy. The bottom Figure is taken from Ref. [3] and shows the measured relaxation rate (3.1) depending on quasiparticle density n_{qp} in units of the Cooper-pair density $n_{cp} = 2\mathcal{N}_F\Delta$.

tunneling events by which quasiparticles are created. This makes the NSN turnstile in particular interesting as a probe to measure the quasiparticle kinetics. Experimentally this has been demonstrated very recently by Maisi *et al.*[9].

In this part of the thesis we will introduce a theoretical model that accounts for the single quasiparticle dynamics in a NSN turnstile, starting from the microscopic theory of superconductivity but including the effect of single-electron charges and Coulomb blockade. First we will shortly introduce the thematic background of single electron sources in the context of metrology. Then we will explain the working principle of a hybrid single electron turnstile and discuss potential error sources that limit its accuracy. After that we will present the model describing the quasiparticle dynamics in a NSN-turnstile and the results which have been published in Ref. [61].

3.1. Turnstiles as single-electron sources

The Josephson effect (JE) [62] and the Quantum Hall effect (QHE) [63] not only initiated new prosperous research areas like the field of solid state based quantum information or the emerging field of topology. First of all these physical phenomena provided a fundamental definition of resistance and voltage by elementary constants. In the framework of the *metrological triangle* the von Klitzing constant $R_K = h/e^2$ and the Josephson constant $K_J = e/h$ offer on the one hand a direct link between voltage and current and on the other hand between voltage and frequency [see Fig. 3.2(a)]. Checking the consistency of these constants in terms of the Planck constant h and the elementary charge e requires a

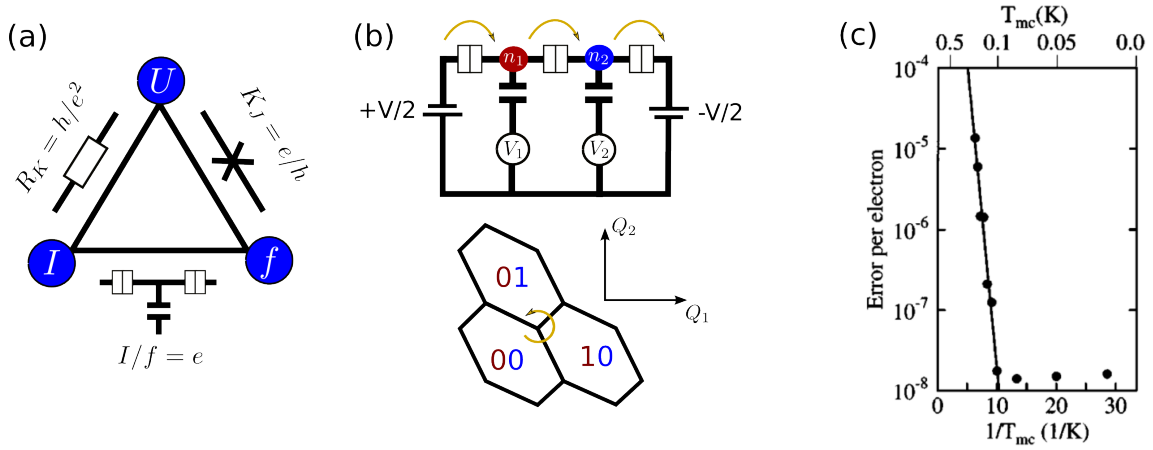

Figure 3.2.: (a) The metrological triangle: The quantum resistance obtained from the hall effect offers a relation between U and I, the ac Josephson-effect gives a relation between voltage applied to a junction and oscillatory frequency of the superconducting phase. Single electron devices may offer a relation between I and f down to metrological accuracy. (b) (Top) NNNN-single electron turnstile. (Bottom) stability diagram of the double-dot device as a function of gate-charge $Q_i = C_i V_i$. By sweeping the gate-voltages in a periodic fashion through the charging states $00 \rightarrow 10 \rightarrow 01$ one charge can be ideally transfered from left to right. (c) Figure from Ref. [65]: Experimental accuracy of the seven-junction device by Keller *et al.*

quantum current standard which measures the amount of integer elementary charges that have been transported through a single electron device by a operation frequency f, i.e. $I = Nef$. According to the fidelity of JE and QHE experiments this requires a metrological accuracy of 10^{-8} [64]. In addition to that the current has to be at least a tenth of nano-ampere [10].

Early proposals

Since the early proposals of the metrological triangle and *Coulomb-blockade* related phenomena [66] several experimental realizations of single electron turnstiles have been put forward. In these devices a voltage bias is imposed between external leads but the single electron tunneling is controlled by the Coulomb blockade. Among them are devices based on semiconducting quantum-dots [67], as well as normal metal devices [68] and hybrid ones involving superconducting leads or islands [7]. The first devices were based on normal metallic islands connected by several junctions. The simplest example, a double-island device is schematically presented in Fig. 3.2(b) and was first realized in Ref. [68]. By choosing an optimal gate offset in between the charging states $(n_1, n_2) = 00, 10, 01$ and by changing the gate voltages in an appropriate way – as indicated in the Coulomb-diamond picture – an electron can be transfered sequentially from island to island corresponding to the protocol $00 \rightarrow 10 \rightarrow 01$. However, this double-dot device suffers from co-tunneling which can be suppressed by increasing the number of islands. The relative accuracy of a seven-junction device by Keller *et al.*[65] is presented in Fig. 3.2(c), showing that metrological accuracy can be indeed reached, though the measured currents are too small to serve as a current standard.

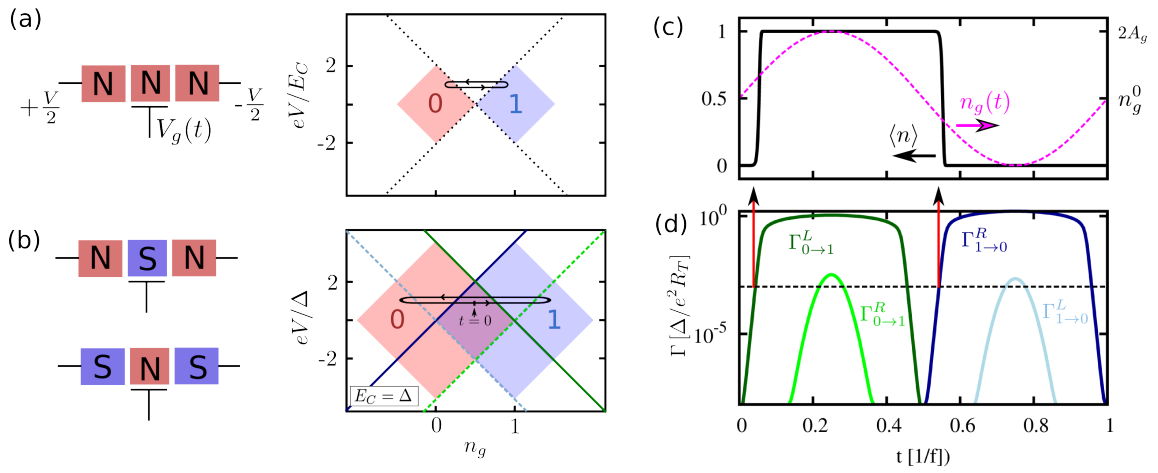

Figure 3.3.: (a) Stability diagram for the NNN single electron transistor. The turnstile protocol indicated by the black loop crosses the region of finite current. (b) Stability diagram for the hybrid-turnstile for the case $E_C = \Delta$. The turnstile protocol works within the region of Coulomb-blockade. The colored lines indicate the thresholds for the transition rates which are shown by same color coding in panel (d) as a function of time for $A_g = 0.7$ and assuming that both, leads and island are thermalized to a temperature of $T = 0.02\,\Delta$. (c) Sinusoidal gate-offset $n_g(t)$ and average excess charge $\langle n \rangle$ on the island. Transitions between the charging states occur when the transition rates become of the order of the driving frequency f which is indicated by the dashed black line.

Hybrid single electron turnstile

Another promising single-electron source has been proposed by Pekola *et al.*[7] which is based on hybrid normal-metal – superconductor junctions. Interestingly these devices have a simple geometry, namely consist of a single island which is either a superconducting or normal metal and leads which are normal or superconducting. It has been shown that the NSN turnstile suffers from overheating of the island [9], whereas for the SNS turnstile uncertainties below 10^{-8} have been predicted by a careful analysis of higher-order tunneling processes [69].

The working principle of the turnstile protocol is illustrated in Fig. 3.3: Two external leads are biased in a symmetric fashion by a voltage V. Furthermore, a gate-voltage is varied periodically $V_g(t) = V_g^0 + eA_g/C_g \sin(2\pi f t)$. Here the normalized offset gate-charge $n_g^0 = 2C_g V_g^0/e$ is set between two charging states. In our example the charging states are 0 and 1 and the gate-offset is $n_g = 0.5$. Applying the turnstile-cycle in the normal state would lead to an unavoidable current flow in the region outside the Coulomb-blockade regime (see stability diagram in Fig. 3.3(a)). However, if the island or the leads are superconducting the combination of Coulomb-blockade and superconducting gap leads to the suppression of single-electron tunneling in the red and blue shaded region of Fig. 3.3(b).

In this case, driving the turnstile cycle leads to the following scenario:

1. Starting at $t = 0$ and ramping up the sinusoidal gate-voltage [see magenta curve in Fig. 3.3(c)] leads to an increase of the transition-rate $\Gamma^L_{0\to1}$ for the an electron to tunnel through the left junction by simultaneously changing the charging state from 0 to 1 [see solid dark-green curve in Fig. 3.3(d)] .

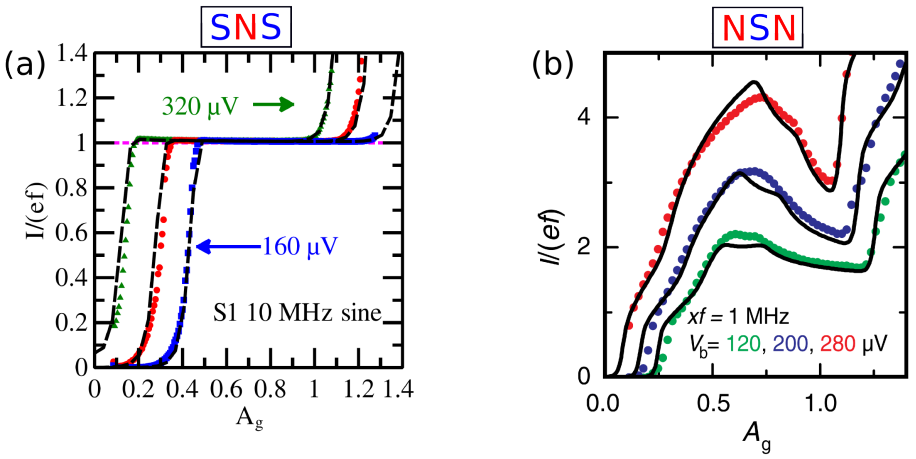

Figure 3.4.: Period averaged current as a function of dimentsionless gate-amplitude A_g for different bias voltages for (a) Figure from Ref. [71] with slight modifications: SNS-turnstile by Aref *et al.* (b) Figure from Ref. [9] with slight modifications: NSN-turnstile by Maisi *et al.*

2. Once the rate $\Gamma^L_{0\to1}$ is of the same order as the driving frequency f [see dashed black line Fig. 3.3(d)] tunneling of an electron occurs changing the average charge $\langle n\rangle$ from 0 to 1 [see black curve Fig. 3.3(c)].

3. Similarly, in the second half of the turnstile protocol the tunneling rate $\Gamma^R_{1\to0}$ becomes large enough to release the extra charge to the right lead changing the charging state back to 0.

Within one turnstile cycle ideally one charge should be transferred from the left to the right. This would correspond to a current of $I = ef$. However, this ideal case is impeded by several error sources summarized in Ref. [7]: First of all there is the possibility of back-tunneling. If the leads and island are well thermalized, this occurs with an error of $\exp(-eV/k_\mathrm{B}T)$, extra forward tunneling would occur with a probability of $\exp(-(2\Delta - eV)/k_\mathrm{B}T)$. The minimization of the joint probability leads to the optimal operation point $eV = \Delta$ of bias voltage. Furthermore working at high frequencies would allow for higher current but on the expense of tunneling events which can be missed with a probability $\exp(-\Delta/2\pi f e R_T)$. Therefore the driving frequency f is always chosen to be much smaller than the characteristic rate $\Gamma^0 = \Delta/e^2R_T$ (see Fig. 3.3(d)). On top of that, higher order tunneling is the major limiting factor of turnstile experiments. As discussed at the end of section 2.2 these happen at a rate $\Gamma^A \sim R_K/R_TN$ for Andreev-tunneling and $\Gamma^\mathrm{CPE} \sim R_K^2/R_T^2N$ for coherent three-electron tunneling. An sufficient suppression of these effects require low-transparent barriers, which on the other hand reduces the current. In Ref. [69] it was argued that metrological accuracy can be reached with a current of maximal order $\sim 10\,\mathrm{pA}$. This necessitates the parallelization for future applications [70]. In Fig. 3.4(a) the period-averaged current of SNS-turnstile [71] is shown as a function of the dimensionless gate-amplitude A_g for various bias voltage. The state of the art metrological accuracy of these devices is of the order of 10^{-4}[10].

3.2. Quasiparticle-dynamics in the NSN turnstile

As mentioned before the NSN-turnstile suffers from quasiparticle excitations when not efficiently depleted from the the superconductor. Fig. 3.4(c) shows the experimental data measured in Ref. [9]. Here the NSN-turnstile was used as a quasiparticle probe, e.g. the single quasiparticle escape rate $\gamma_{esc} = I_{\rm parity}/e$ was determined in good agreement with the prediction (2.41). In addition, the quasiparticle recombination-rate has been inferred for the particular case that only two quasiparticles reside on the island. The control of the number of excitations ultimately follows from the turnstile protocol that has been explained before. Each tunneling-process is accompanied by the creation of quasiparticles or holes. These energetically relax via electron-phonon or electron-electron interaction and escape via recombination into the superconducting condensate or by tunneling into the normal electrodes. In the following sections we will introduce a model which accounts for the excitation of quasiparticles by single-charge tunneling as well as their relaxation due to the interaction with a phonon-bath. We would like to mention that a similar theoretical model has been used by Maisi *et al.* [9] in order to model the experimental data therein (see black lines in Fig. 3.4). The equivalence of the two approaches has been presented in the appendix of Ref. [61].

3.2.1. Model

We consider a superconducting island (S) coupled to a left (L) and right (R) normal metallic lead via tunneling barriers. The total Hamiltonian is given by

$$H = \sum_{r=L,\,R} H_r + H_S + H_T. \tag{3.2}$$

The normal metal leads are assumed to be reservoirs of noninteracting electrons,

$$H_r = \sum_{k\sigma} \left(\xi_{rk\sigma} - \mu_r\right) c^\dagger_{rk\sigma} c_{rk\sigma}. \tag{3.3}$$

Here $\xi_{rk\sigma}$ is the energy of an electron with momentum k and spin σ, and $c^\dagger_{rk\sigma}$ are the corresponding creation operators. The applied voltage shifts the electro-chemical potentials by $\mu_{L(R)} = (-)eV/2$. Furthermore we assume that leads are equilibrated, such that the density matrices of the leads are given by

$$\hat{\rho}_r = \frac{e^{-\beta H_r}}{\mathrm{Tr}(e^{-\beta H_r})}. \tag{3.4}$$

Here $\beta = 1/k_{\rm B}T$ is the inverse temperature. The Hamiltonian of the superconducting island is given by

$$H_S = \underbrace{\sum_{k\sigma} E_k\, \gamma^\dagger_{k\sigma}\gamma_{k\sigma}}_{H_{qp}} + \underbrace{E_C(\hat{n} - n_g)^2}_{H_{ch}} + \underbrace{\sum_q \omega_q b^\dagger_q b_q}_{H_{ph}} + H_{\rm e-ph}. \tag{3.5}$$

The first term accounts for Bogoliubov quasiparticles (see Eq. (1.24)) with energy E_k, where $\gamma^\dagger_{k\sigma}$ and $\gamma_{k\sigma}$ are the corresponding creation and annihilation operators, which are connected to the electronic ones by the transformations

$$\begin{aligned} d_{k\sigma} &= u_k\gamma_{k\sigma} + \sigma v_k \overline{\gamma}^\dagger_{k\sigma}, \\ d^\dagger_{k\sigma} &= u_k\gamma^\dagger_{k\sigma} + \sigma v_k \overline{\gamma}_{k\sigma}. \end{aligned} \tag{3.6}$$

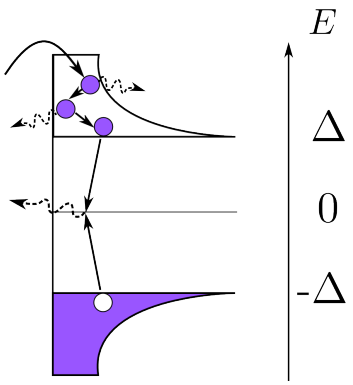

Figure 3.5.: Illustration of the electron-phonon-interaction: an electron-like quasiparticle injected to the island is initially scattered by phonons quickly relaxing to an energy just above Δ, where it finally recombines with a hole.

The coherence factors u_k and v_k are defined in Eq. (1.22). The second term in (3.5) corresponds to the charging energy (2.14) of the island modeled by an effective capacitance C, i.e. $E_C = e^2/2C$. The number of excess-charges on the island is given by the operator $\hat{n}$. Furthermore, $en_g = C_g V_g$ is the capacitively induced gate-charge. The third term, H_{ph}, is the Hamiltonian of the phonon-bath which we will assume to be thermalized as well, i.e. the phonon density matrix is given by

$$\hat{\rho}_{\mathrm{ph}} = \frac{e^{-\beta H_{\mathrm{ph}}}}{\mathrm{Tr}(e^{-\beta H_{\mathrm{ph}}})}. \tag{3.7}$$

According to Eq. (1.3) and Eq. (1.22) the electron-phonon interaction can be expressed in terms of the phonon operator, b_q and $b_q^\dagger$ and the Bogolioubov quasiparticle operators, i.e.

$$\begin{aligned} H_{e-ph} = &\sum_{qk\sigma} \underbrace{g_{k+q,k}\,(u_{k+q}u_k - v_{k+q}v_k)\gamma^\dagger_{k+q,\sigma}\gamma_{k\sigma}}_{S^\sigma_{k+q,k}}(b_q + b^\dagger_{-q}) \\ &+ \sum_{qk\sigma} \underbrace{g_{k+q,k}\,(u_{k+q}v_k + v_{k+q}u_k)\gamma^\dagger_{k+q,\sigma}\overline{\gamma}^\dagger_{k\sigma}}_{R^\sigma_{k+q,k}}(b_q + b^\dagger_{-q}) + H.c. \end{aligned} \tag{3.8}$$

Here we define the "time-reversed" operators $\overline{\gamma}_{k\sigma} \equiv \gamma_{-k-\sigma}$ and assume that σ can take the values ± 1 corresponding to spin up and down. Later it will be convenient to introduce the combinations $S^\sigma_{k+q,k}$ and $R^\sigma_{k+q,k}$ corresponding to the scattering or recombination and pair-breaking of quasiparticles respectively. As illustrated in Fig. 3.5 a quasiparticle initially injected into the island through one of the junctions is inelastically scattered by phonons, relaxing to an energy close to the gap-edge, before it recombines together with a hole. The first and second line of (3.8) account for these processes respectively.

Finally, in order to model the coupling to the leads we introduce the tunnel Hamiltonian

$$H_T = \sum_{rkk'\sigma} t^r_{kk'}\,\hat{T}\,e^{-i\phi} c^\dagger_{rk'\sigma}(u_k\gamma_{k\sigma} + \sigma v_k \overline{\gamma}^\dagger_{k\sigma}) + H.c. \tag{3.9}$$

The operator $\hat{T} = \sum_n |n\rangle\langle n+1|$ accounts for changes of the number of electrons in the island, and $\phi(t) = \int_{t_0}^t dt'\, eV_\phi(t')$ is the phase associated with the time-dependent gate

voltage that is capacitively applied to the island,

$$V_\phi(t) = -\frac{eA_g}{C_g}\sin(2\pi f t). \tag{3.10}$$

Parity effect

Following the discussion in section (2.2) we will include the parity effect in our calculation by assuming a grand canonical ensemble, i.e. we allow for fluctuations of the number of quasiparticles and project onto the subspace with even or odd number of electrons on the island. The corresponding density matrix for the even and odd subsector is given by

$$\hat{\rho}_{qp}^{\text{even/odd}} = \frac{\hat{P}^{\pm}\hat{\rho}_{qp}}{\text{Tr}(\hat{P}^{\pm}\hat{\rho}_{qp})}, \tag{3.11}$$

with the unprojected quasiparticle density matrix

$$\hat{\rho}_{qp} = \prod_{k\sigma}\left[(1-F_{k\sigma})(1-\hat{n}_{k\sigma}) + F_{k\sigma}\hat{n}_{k\sigma}\right]. \tag{3.12}$$

Here the distribution function $F_{k\sigma} = \text{Tr}(\hat{n}_{k\sigma}\hat{\rho}_{qp})$ with $\hat{n}_{k\sigma} = \gamma^\dagger_{k\sigma}\gamma_{k\sigma}$ is expressed by a capital letter in order to distinguish it from its equilibrium value $f_{k\sigma} = [\exp(E_k/k_\text{B}T) + 1]^{-1}$. In analogy to (2.31) the quasiparticle distribution in the even and odd state is given by

$$\text{Tr}(\hat{n}_{k\sigma}\hat{\rho}_{qp}^{\text{even/odd}}) = F_{k\sigma}\mathcal{A}_{\text{even/odd}}. \tag{3.13}$$

For a given number of excess charges n on the island, the factor $\mathcal{A}_{\text{even/odd}}$ can be written as

$$\mathcal{A}_n = [\tanh(N_{qp})]^{(-1)^n}. \tag{3.14}$$

In contrast to the equilibrium situation the number of quasiparticle excitations $N_{qp} = \sum_{k\sigma} F_{k\sigma}$ is a non-equilibrium quantity and we have to derive a kinetic equation for it.

Sequential tunneling master equation and kinetic Boltzmann equation

We treat both the tunneling Hamiltonian H_T as well as the electron-phonon interaction H_{e-ph} within a second order perturbation theory. Thus we separate the Hamiltonian (3.2) into $H_0 = H_S + \sum_r H_r + H_{ph}$ and a perturbation $H_I = H_T + H_{e-ph}$. After changing into the interaction picture the Liouville equation for the density matrix of the system within the Markov approximation reads

$$\frac{d}{dt}\hat{\rho}(t) = -\int_{-\infty}^{t} dt' \,[H_I(t),[H_I(t'),\hat{\rho}(t)]], \tag{3.15}$$

where $H_I(t) = \exp(iH_0t)H_I\exp(-iH_0t)$. We are interested in the time-evolution of the probability to find n excess charges on the island, i.e. $p_n = \text{Tr}\{|n\rangle\langle n|\,\hat{\rho}\}$, and the occupation of the quasiparticle state with momentum k and spin σ, i.e. $F_{k\sigma} = \text{Tr}\{\hat{n}_{k\sigma}\,\hat{\rho}\}$.

We assume that the density matrix factorizes into the density matrices of the leads, the phonon-bath and the quasiparticles,

$$\hat{\rho} = \hat{\rho}_L \hat{\rho}_R \hat{\rho}_{ph} \left(\sum_n p_n \hat{\rho}^n_{qp} \left| n \right\rangle \left\langle n \right| \right). \tag{3.16}$$

Here $\hat{\rho}^n_{qp}$ is the parity projected density matrix (3.11). Mind that we separated the density matrix of the superconductor's electronic degrees of freedom into charge and quasiparticles, although these are directly connected quantities. The separation of quasiparticle and charge degrees of freedom is a valid approximation as long as we can neglect the dependence of the quasiparticle-distribution function $F_{k\sigma}$ on the total number of charges. This is true if the level-spacing is small [72] which is the case for the metallic island considered here. Furthermore the parity projection appropriately accounts for the parity dependence of the quasiparticle distribution (see Eq. (3.13)).

In order to keep track of the charge and quasiparticles on the island we decompose the tunneling Hamiltonian into terms

$$\begin{aligned} H^{++}_{k\sigma} &= \sum_{rk'} (t^r_{kk'})^* u_k \, \hat{T}^\dagger e^{i\phi} \gamma^\dagger_{k\sigma} c_{rk'\sigma} \, , \\ H^{+-}_{k\sigma} &= \sum_{rk'} (t^r_{kk'})^* \sigma \, v_k \, \hat{T}^\dagger e^{i\phi} \gamma_{-k-\sigma} c_{rk'\sigma}, \end{aligned} \tag{3.17}$$

with $H^{\alpha\beta}_{k\sigma} = (H^{-\alpha,-\beta}_{k\sigma})^\dagger$ and $\alpha, \beta = \pm$. The total tunneling Hamiltonian is given by $H_T = \sum_{k\sigma} \sum_{\alpha\beta} H^{\alpha\beta}_{k\sigma}$. For instance, $H^{--}_{k\sigma}$ removes a charge and an excitation with momentum $-k$ and spin $-\sigma$ from the island, whereas $H^{-+}_{k\sigma}$ would remove a charge but add a quasiparticle excitation k, σ. With Eq. (3.15) we find for the charge occupation p_n

$$\frac{d}{dt} p_n = 2\mathrm{Re} \int_{-\infty}^{t} dt' \sum_{\alpha\beta} \sum_{k\sigma} \mathrm{Tr} \left[H^{\alpha\beta}_{k\sigma}(t) H^{\bar{\alpha}\bar{\beta}}_{k\sigma}(t') \hat{\rho}_{n+\alpha}(t) - H^{\bar{\alpha}\bar{\beta}}_{k\sigma}(t') H^{\alpha\beta}_{k\sigma}(t) \hat{\rho}_n(t) \right] \tag{3.18}$$

where $\bar{\alpha} = -\alpha$. Using Wick's theorem and carrying out the traces we are now able to express the transition rates in terms of distribution functions $f_{rk\sigma}$ of the leads and $F_{k\sigma}$, e.g. for the transition from $n+1$ to n with the simultaneous annihilation of a quasipartile we get

$$\begin{aligned} I^{--} &= 2\mathrm{Re} \sum_{k\sigma} \int_{-\infty}^{t} dt' \mathrm{Tr} \big(H^{++}_{k\sigma}(t) H^{--}_{k\sigma}(t') \hat{\rho}_{n+1}(t) \big) \\ &= \sum_{rkk'\sigma} |t^r_{kk'}|^2 u_k^2 (1 - f_{rk'\sigma}) \mathcal{A}_{n+1} F_{k\sigma} p_{n+1} \\ &\quad \times 2\mathrm{Re} \int_{-\infty}^{t} dt' e^{-i(\xi_{rk'\sigma} + eV_r - eV_\phi(t) - E_{n+1} + E_n - E_k)(t-t')}. \end{aligned} \tag{3.19}$$

Here we introduced the charging energy $E_n = E_C (n - n_g^0)^2$ with respect to the dc offset charge n_g^0. In the spirit of Markov's approximation we further linearized the time-dependence of ϕ, i.e. $\phi(t') = \phi(t) - eV_\phi(t)(t-t')$. In this case the time-integral in (3.19)

can be carried out explicitly, yielding

$$I^{--} = 2\pi \sum_{rkk'\sigma} |t^r_{kk'}|^2 u_k^2 \big[1 - f_{rk'\sigma}\big] \mathcal{A}_{n+1} F_{k\sigma} p_{n+1} \delta(\xi_{rk'\sigma} + eV_r - eV_\phi(t) - E_{n+1} + E_n - E_k). \tag{3.20}$$

Introducing the energy dependent quasiparticle distributions $f_{rk'\sigma} = [\exp(\xi_{k'}/k_\mathrm{B}T) + 1]^{-1}$ and $F_{\xi\sigma} = \frac{1}{\mathcal{N}_F \mathcal{V}} \sum_k \delta(\xi - \xi_k) F_{k\sigma}$ and further expressing the tunneling amplitude by an effective energy-independent tunneling resistance,

$$2\pi \sum_{kk'} |t^r_{kk'}|^2 \delta(\xi - \xi_k)\delta(\xi' - \xi_{k'}) \approx \frac{1}{e^2 R^r_T}\,, \tag{3.21}$$

Eq. (3.20) can be written as

$$I^{--} = \sum_r \frac{1}{e^2 R^r_T} u_\xi^2 \big[1 - f(E - eV_r + eV_\phi(t) + E_{n+1} - E_n)\big] \mathcal{A}_{n+1} F_{\xi\sigma} p_{n+1}. \tag{3.22}$$

All other contributions in (3.18) have to be treated in the same way. Here we will only mention the final result, given by the *sequential tunneling master equation*

$$\frac{d}{dt} p_n(t) = \Gamma_{n,n-1}(t) p_{n-1}(t) + \Gamma_{n,n+1}(t) p_{n+1}(t) - [\Gamma_{n-1,n}(t) + \Gamma_{n+1,n}(t)] p_n(t). \tag{3.23}$$

Here the transition rates from charging state n to m, i.e. $\Gamma_{m,n} = \sum_{r=L,R} \Gamma^r_{m,n}$, are given by

$$\begin{aligned}
\Gamma^r_{n+1,n}(t) &= \sum_\sigma \int d\xi \left[w^r_{n+1,n}(E,t) \frac{1 - \mathcal{A}_n F_{\xi\sigma}}{2} \left(1 + \frac{\xi}{E}\right) + w^r_{n+1,n}(-E,t) \frac{\mathcal{A}_n F_{\xi\sigma}}{2} \left(1 - \frac{\xi}{E}\right) \right], \\
\Gamma^r_{n-1,n}(t) &= \sum_\sigma \int d\xi \left[w^r_{n-1,n}(-E,t) \frac{1 - \mathcal{A}_n F_{\xi\sigma}}{2} \left(1 - \frac{\xi}{E}\right) + w^r_{n-1,n}(E,t) \frac{\mathcal{A}_n F_{\xi\sigma}}{2} \left(1 + \frac{\xi}{E}\right) \right].
\end{aligned} \tag{3.24}$$

They depend on the non-equilibrium distribution $F_{\xi\sigma}$ which has to be determined by a kinetic equation. The parity effect enters by the factor $\mathcal{A}_n$. Furthermore we introduced the combinations

$$\begin{aligned}
w^r_{n+1,n}(E,t) &= \frac{f^r\left(E_{n+1} - E_n + eV_\phi(t) - \mu_r + E\right)}{e^2 R^r_T}, \\
w^r_{n-1,n}(E,t) &= \frac{1 - f^r\left(E_n - E_{n-1} + eV_\phi(t) - \mu_r + E\right)}{e^2 R^r_T},
\end{aligned} \tag{3.25}$$

that contain the distribution functions of the leads, f^r, as well as the tunneling resistance R^r_T. We do not take into account second-order cotunneling as it is suppressed by additional factors (R_K/R_T). In the non-equilibrium situation that is considered here single-electron tunneling will be the most dominant tunneling-process.

In a similar way we derive the time-evolution of the quasiparticle occupation of a state $k\sigma$ under the condition that n charges reside on the island, i.e.

$$\frac{d}{dt}\left\langle \hat{n}_{k\sigma}\hat{\mathcal{P}}_n\right\rangle = i\left\langle [H_I,\hat{n}_{k\sigma}]\hat{\mathcal{P}}_n + \hat{n}_{k\sigma}[H_I,\hat{\mathcal{P}}_n]\right\rangle \tag{3.26}$$

where $\hat{\mathcal{P}}_n = |n\rangle\langle n|$ is the projection operator onto charging state n. By summing over all charging states the second term vanishes because of conservation of probability and we obtain

$$\frac{d}{dt}\left\langle \hat{n}_{k\sigma}\hat{\mathcal{P}}_n\right\rangle = \underbrace{i\left\langle [H_T,\hat{n}_{k\sigma}]\hat{\mathcal{P}}_n\right\rangle}_{tun} + \underbrace{i\left\langle [H_{e-ph},\hat{n}_{k\sigma}]\hat{\mathcal{P}}_n\right\rangle}_{e-ph} \tag{3.27}$$

The first term corresponds to quasiparticle-tunneling and in accordance to (3.18) gives

$$\frac{d}{dt}\sum_n \left\langle \hat{n}_{k\sigma}\hat{\mathcal{P}}_n\right\rangle\Big|_{tun} = -2\mathrm{Re}\int_{-\infty}^{t} dt' \sum_n\sum_{\alpha\beta}\mathrm{Tr}\left(\beta H^{\alpha\beta}_{k\sigma}(t)H^{\bar{\alpha}\bar{\beta}}_{k\sigma}(t')\hat{\rho}_n(t)\right). \tag{3.28}$$

The second term accounts for the interaction of quasiparticles and phonons, i.e.

$$\begin{aligned}&\frac{d}{dt}\sum_n \left\langle \hat{n}_{k\sigma}\hat{\mathcal{P}}_n\right\rangle\Big|_{e-ph}\\ &= -2\mathrm{Re}\int_{-\infty}^{t} dt' \sum_{nq}\mathrm{Tr}\Big(h^{\sigma}_{k,k-q}(t)[h^{\sigma}_{k,k-q}(t')]^{\dagger}\hat{\rho}_n(t) - [h^{\sigma}_{k,k-q}(t)]^{\dagger}h^{\sigma}_{k,k-q}(t')\hat{\rho}_n(t)\Big).\end{aligned} \tag{3.29}$$

with the combinations $h^{\sigma}_{k+q,k} = \left(S^{\sigma}_{k+q,k} + R^{\sigma}_{k+q,k}\right)(b_q + b^{\dagger}_{-q})$ and $S(R)^{\sigma}_{k+q,k}$ defined in (3.8). In contrast to (3.28) the scattering integrals in (3.29) now also contain combinations $\hat{n}_{k\sigma}(1-\hat{n}_{q\beta})$, corresponding to a quasiparticle scattering from state $k\sigma$ into the state $q\alpha$ and combinations which account for the recombination of a quasiparticle and a hole, i.e. $\hat{n}_{k\sigma}\hat{n}_{q\beta}$. At this point we remind the reader on section 2.2, where we discussed the parity projection of the density matrix. We realized that the projection operator $\hat{P}^{\pm}$ did not commute with $\hat{n}_{\boldsymbol{k}\sigma}$. The same is true for the combinations mentioned before. With the parity-projected density matrix (3.11) we obtain

$$\begin{aligned}\langle \hat{n}_{k\sigma}\hat{n}_{q\beta}\rangle_{even/odd} &= F_{k\sigma}F_{q\beta}\frac{1\pm\exp(-2\sum_{p\alpha\neq k\sigma,q\beta}F_{p\alpha})}{1\pm\exp(-2\sum_{p\alpha}F_{p\alpha})},\\ \langle \hat{n}_{k\sigma}(1-\hat{n}_{q\beta})\rangle_{even/odd} &= F_{k\sigma}(1-F_{q\beta})\frac{1\mp\exp(-2\sum_{p\alpha\neq k\sigma,q\beta}F_{p\alpha})}{1\pm\exp(-2\sum_{p\alpha}F_{p\alpha})}.\end{aligned} \tag{3.30}$$

for $F_{k\sigma} \ll 1$. Because of the small level-splitting it is reasonable to approximate these expectation values by $\langle \hat{n}_{k\sigma}(1-\hat{n}_{q\alpha})\rangle_n \approx \mathcal{A}_n F_{k\sigma}(1-F_{q\alpha})$ and $\langle \hat{n}_{k\sigma}\hat{n}_{q\alpha}\rangle_n \approx F_{k\sigma}F_{q\alpha}$. After standard manipulations explained before, we finally arrive at the *kinetic Boltzmann*

equation for $F_{\xi\sigma}$,

$$\begin{aligned}
&\frac{d}{dt}\left[\sum_n p_n \mathcal{A}_n F_{\xi\sigma}\right] \qquad (3.31)\\
&= \frac{1}{\mathcal{N}_F \mathcal{V}} \sum_{rn} \sum_{s=\pm 1} p_n \left[w^r_{n+s,n}(sE,t) \frac{1-\mathcal{A}_n F_{\xi\sigma}}{2}\left(1+s\frac{\xi}{E}\right) - w^r_{n+s,n}(-sE,t)\frac{\mathcal{A}_n F_{\xi\sigma}}{2}\left(1-s\frac{\xi}{E}\right)\right]\\
&+ \pi \int d\xi' \alpha^2 F(E+E')^2 \left(1-\frac{\xi\xi'}{EE'}+\frac{\Delta^2}{EE'}\right)\left[(1-F_{\xi\sigma})(1-F_{\xi'\bar{\sigma}})n^B_{E+E'} - F_{\xi\sigma}F_{\xi'\bar{\sigma}}(1+n^B_{E+E'})\right]\\
&+ \pi \int d\xi' \alpha^2 F(E'-E)^2 \mathrm{sign}(E'-E)\left(1+\frac{\xi\xi'}{EE'}-\frac{\Delta^2}{EE'}\right)\\
&\times \left[F_{\xi'\sigma}(1-F_{\xi\sigma})(1+n^B_{E'-E}) - F_{\xi\sigma}(1-F_{\xi'\sigma})n^B_{E'-E}\right]\sum_n p_n \mathcal{A}_n.
\end{aligned}$$

Here $\bar{\sigma} = -\sigma$, and $n^B_\omega = [\exp(\omega/k_\mathrm{B}T)-1]^{-1}$ is the Bose-function. The first line describes the excitation via tunneling whereas the following lines account for the inelastic recombination, pair-breaking and scattering processes. Furthermore we introduced the α^2F-spectrum (see Eq. (1.7) in chapter 1). Since only low energies ω are concerned we approximate the energy dependence of the α^2F-spectrum by its form $\alpha^2F(\omega) \approx b\omega^2\theta(\omega)$. The electron-phonon coupling constant is well cataloged in the literature [26]. It can be expressed in terms of the experimentally more relevant parameter Σ, which appears in the heat current between electrons and phonons in the normal state [73], given by $P_{e-ph} = \Sigma\mathcal{V}(T_e^5 - T_{ph}^5)$, i.e.

$$b = \Sigma/48\pi\zeta(5)\mathcal{N}_F. \qquad (3.32)$$

According to (3.31) we introduce the characteristic scale for the electron-phonon coupling, $\Gamma_{e-ph} = \pi b\Delta^3$. For aluminum one has $\Sigma \approx 1.8\times10^9\mathrm{WK}^{-5}\mathrm{m}^{-3}$, $\Delta \approx 210\,\mu\mathrm{eV}$ and $\mathcal{N}_F \approx 2.32\times10^{28}\mathrm{eV}^{-1}\mathrm{m}^{-3}$[9], which gives $\Gamma_{e-ph} \approx 18\,\mathrm{MHz}$.

In general, the kinetic equation (3.31) should also contain collision integrals induced by the short range Coulomb interaction between the electrons. In our model we omit it because we will mostly focus on the regime where the current through our device merely depends on the total number of quasiparticles N_{qp}, and not on the specific form of the distribution function $F_{\xi\sigma}$. Since the electron-electron interaction does not cause recombination or creation of quasiparticles, it does not change N_{qp} and, hence, may be neglected.

3.2.2. Quasiparticle excitation and relaxation

Eqs. (3.23) and (3.31) are the main results of this chapter. They can be solved numerically yielding full information about the time and energy-dependence of the distribution function. In the following pages we will present the results of our simulations. In this context we discuss the events that contribute to the relaxation of quasiparticles, discuss the energy dependence of their distribution function and show that the rather lengthy kinetic equation (3.31) may be replaced by a much simpler equation for the total quasiparticle number. We furthermore assume spin-degeneracy, i.e. $F_{\xi\uparrow} = F_{\xi\downarrow} \equiv F_\xi$, because we neither have magnetic leads, nor do we consider any spin-flip processes. The parameters that we are using in our numerics are summarized in Table 3.1.

E_C	eV	T	$(e^2 R_T^L \mathcal{N}_F \mathcal{V})^{-1}$	$(e^2 R_T^R \mathcal{N}_F \mathcal{V})^{-1}$	$\mathcal{N}_F \mathcal{V} \Delta$
$8\Delta/7$	$4\Delta/3$	$\Delta/40$	$1.8 \times 10^{-2} \Gamma_{e-ph}$	$2.5 \times 10^{-2} \Gamma_{e-ph}$	22490

Table 3.1.: Parameters used in the simulations unless other values are specified. The chosen parameters produce the best fit to the experimental data of Ref. [9]. Here $\Gamma_{e-ph} = \pi b \Delta^3$ gives a characteristic scale for the rate of the electron-phonon relaxation (see text).

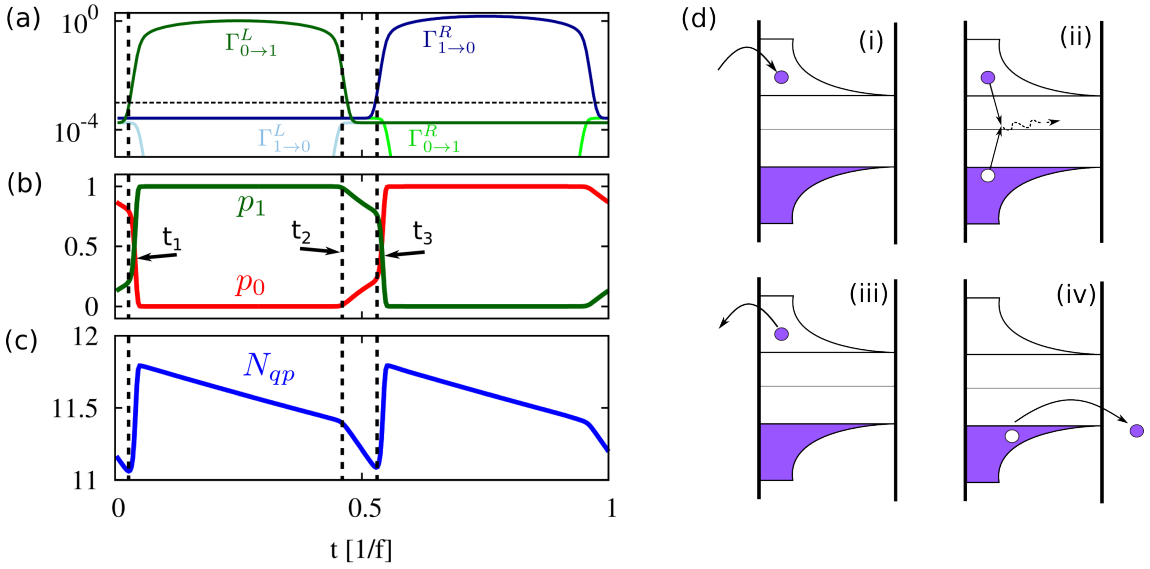

Figure 3.6.: Time-dependence of (a) the transition rates, plotted for an average quasiparticle number $N_{qp} \approx 11.5$, (b) the charge occupation probabilities p_0 and p_1, (c) the quasiparticle number N_{qp}. In panel (d) the different pictures show (i) the creation of electron-like quasiparticles at time t_1, (ii) the relaxation via recombination, (iii) their escape into the leads within the time intervall (t_2, t_3), and (iv) the creation of a hole-like quasiparticle at the time instant t_3. (For the simulations the gate offset is chosen in between the two charging states 0 and 1, i.e. $n_g^0 = 0.5$. The gate amplitude of the periodic gate charge is given by $A_g = 0.5$. The modulation frequency is $f = 5.56 \times 10^{-2} \Gamma_{e-ph}$.)

Quasiparticle distribution function

To start with we consider frequencies for which the parity effect can be neglected and $\mathcal{A}_n \approx 1$. In order to explain the relation between quasiparticle and charge dynamics we refer to Fig. 3.6. Among other things it shows the time-dependence of the occupation probability p_n as well as the quasiparticle number

$$N_{qp} = 2\mathcal{N}_F \mathcal{V} \int_{-\infty}^{\infty} d\xi \, F_\xi. \tag{3.33}$$

In the following we discuss the quasiparticle dynamics that follows from the various tunneling and relaxation events during the turnstile operation. Panel (d) depicts all these processes in an illustrative way.

1. Starting at the time-instant t_1 [see panel (b)] a charge tunnels onto the island changing the state from $n = 0$ to $n = 1$. The tunneling process also increases the quasiparticle number [panel (d)-(i)],

2. In the following quasiparticles relax due to recombination [panel (d)-(ii)] with the recombination-rate

$$\frac{1}{\tau_{rec}} = \kappa N_{qp}, \tag{3.34}$$

where $\kappa = 4\Gamma_{e-ph}/\mathcal{N}_F\mathcal{V}\Delta$ characterizes the rate of quasiparticle recombination and for the relevant experimental parameters is of the order $\kappa = 2 \times 10^{-4}\Gamma_{e-ph}$ [61].

3. Then at the time-instant t_2, do to the presence of non-equilibrium quasiparticles, the transition rates $\Gamma^{L,R}_{1\to 0}$ become significant leading to a back-flow of charge into the leads and an abrupt decay of the occupation probability p_1. According to this quasiparticles may also escape into the leads in the time-window (t_2, t_3) [see panel (d)-(iii)]. The corresponding escape-rate is given by

$$\gamma^r_{esc} = \frac{1}{2e^2 R^r_T \mathcal{N}_F \mathcal{V}}. \tag{3.35}$$

4. Next, at a time t_3 an electron leaves the dot when $\Gamma^R_{1\to 0}$ becomes of the order of the driving frequency. Simultaneously a hole-like quasiparticle is created [panel (d)-(iv)]. One observes that the decrease in electron-like quasiparticles in the time-interval (t_2, t_3) and the rapid increase of hole-like quasiparticles at t_3 sums up to 1, consistent with the total change of charge by one e.

Due to the fact that the tunneling resitance and the applied dc bias voltage used in the simulations is rather symmetric we expect that the imbalance between electron and hole-like quasiparticles is small. This is evident from the fact that in the turnstile cycle the same amount of them is generated on average. To confirm this assumption we introduce a quantity which measures the *charge-imbalance*, the so-called quasiparticle-charge density Q^* (see Eq. (2.24)), [74, 75]

$$Q^* = \mathcal{N}_F\mathcal{V}\int_{-\infty}^{\infty} d\xi \frac{\xi}{\sqrt{\Delta^2+\xi^2}} F_\xi. \tag{3.36}$$

If the number of particle-like excitations is larger than the number of hole-like excitations the charge imbalance is positive and vise versa (see Fig. 3.7(a)). A comparison of Q^* and N_{qp} shows that indeed the charge imbalance is small. It increases linearly for small junction asymmetry factors $\alpha = (R^R_T - R^L_T)/(R^R_T + R^L_T)$ [61], but remains of the same order of magnitude as long as the bias voltage remains symmetric. Thus we can generally neglect the charge imbalance.

As a next step we present the period averaged distribution function

$$\langle F_\xi \rangle = f\int_0^{1/f} dt\, F_\xi(t) \tag{3.37}$$

in Fig. 3.8. In order to understand the specific energy dependence we have to analyze the interplay of the different quasiparticle relaxation channels like tunneling, inelastic phonon scattering and recombination which enter the Boltzmann equation (3.31). The relaxation rate that results from inelastic scattering at phonons is given by,

$$\frac{1}{\tau_{sc}(E)} = \Gamma_{e-ph}\frac{\sqrt{2}(E-\Delta)^{7/2}}{E\Delta^{5/2}},. \tag{3.38}$$

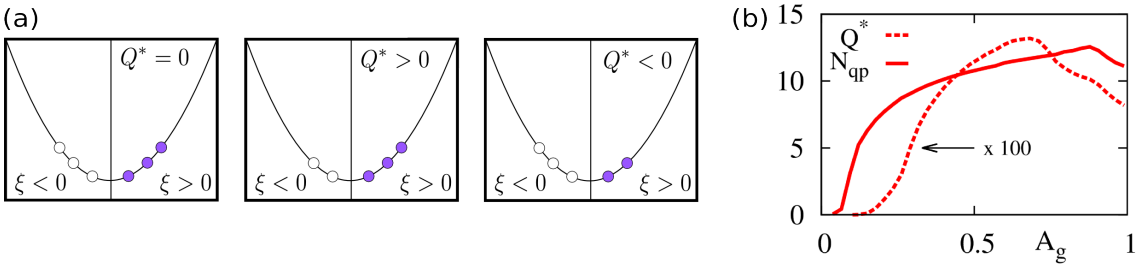

Figure 3.7.: (a) Illustration of charge imbalance. (b) Quasiparticle number N_{qp} and quasiparticle charge-density Q^* depending on gate-amplitude. Figure from Ref. [61].

This relaxation-process preserves the quasiparticle number and only modifies the energy dependence of the distribution function. The overall number of quasiparticles can be changed by recombination events that happen at a rate

$$\frac{1}{\tau_{rec}(E)} = \Gamma_{e-ph} \frac{(E+\Delta)^3}{2E\Delta^2} \frac{N_{qp}}{\mathcal{N}_F \mathcal{V} \Delta}\,, \tag{3.39}$$

which is proportional to N_{qp}. These rates are consistent with the temperature dependent lifetimes derived in Eq. (1.15). The energy dependence of (3.38) and (3.39) is shown in Fig. 3.8(a). At an energy $E_0 \approx \Delta(1 + 2(N_{qp}/2\mathcal{N}_F\mathcal{V}\Delta)^{2/7})$ both are equal, at $E > E_0$ inelastic scattering dominates, while at $E < E_0$ recombination becomes more important. For $N_{qp} \ll 1$ the energy E_0 is close to Δ, which leads to the following scenario: high energy quasiparticles are quickly equilibrated by inelastic phonon scattering, before they subsequently recombine at lower energies. This results in a local-equilibrium distribution $F_\xi^{\mathrm{loc}} = [\exp((E-\mu)/k_\mathrm{B}T) + 1]^{-1}$ where T is the phonon temperature. Within the relaxation time approximation the phonon-scattering term in Eq. (3.31) reads

$$\dot{F}_\xi\big|_{e-ph} = -\frac{F_\xi - F_\xi^{\mathrm{loc}}}{\tau(E)} \tag{3.40}$$

with $1/\tau = 1/\tau_{sc} + 1/\tau_{rec}$. This relaxation is balanced by the influx of new quasiparticles from the leads, approximately given by $I_{in} = f/2\mathcal{N}_F\mathcal{V}\Delta$. This phenomenological argument offers the energy dependence

$$F_\xi = \tau(E) I_{in} + F_\xi^{\mathrm{loc}}, \tag{3.41}$$

with N_{qp} being the only fitting parameter. The chemical potenial is fixed by Eq. (3.33). In Fig. 3.8(b) these fits are presented by the red lines and match the numerical data in blue quite well.

Rothwarf-Taylor equation

Based on the previous discussion we find that for the case at hand the electron-phonon interaction leads to a quasiparticle distribution which is nearly particle-hole symmetric and well peaked in a small energy-window around $\xi = 0$. Other scattering channels like electron-electron interaction would lead to an additional change of the energy dependence however most quasiparticles would still be distributed in the same energy-window. This encourages to employ the particular energy dependence of F_ξ and to express Eqs. (3.23)

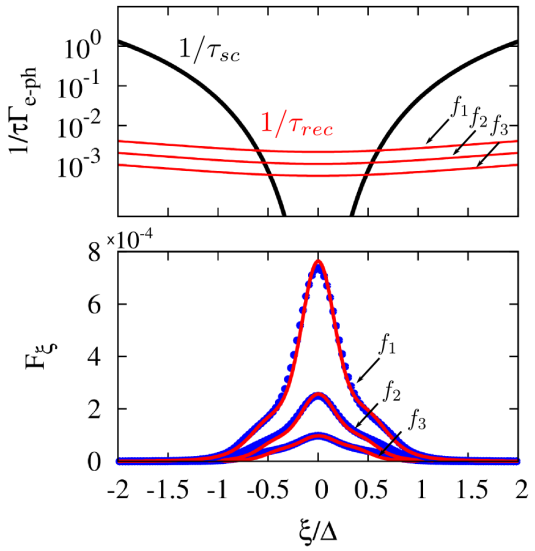

Figure 3.8.: Comparison of the relaxation rates in Eqs. (3.38) and (3.39) and the distribution function F_ξ for three different frequencies $f_{1,2,3} = 5.56,\ 1.11,\ 0.28 \times 10^{-2}\Gamma_{e-ph}$. In the bottom panel the blue dots show the numerical result, the red lines are fits corresponding to (3.41). (for the simulations we used $A_g = 0.5$)

and (3.31) in terms of the quasiparticle number, N_{qp}. In this spirit we find the approximate relations for charge-transition rates

$$\Gamma^r_{n\pm1,n} = \int d\xi w^r_{n\pm1,n}(\pm E) - [w^r_{n\pm1,n}(\pm\Delta) - w^r_{n\pm1,n}(\mp\Delta)]\frac{\mathcal{A}_n N_{qp}}{2\mathcal{N}_F\mathcal{V}}, \tag{3.42}$$

which enter the master-equation (3.23). In addition to that the integrated Boltzmann equation assumes a simplified form,

$$\frac{d}{dt}\left[N_{qp}\sum_n p_n\mathcal{A}_n\right] = \sum_n p_n\left[I^{qp}_n - \Gamma^{qp}_n N_{qp}\mathcal{A}_n - \kappa N^2_{qp}\right]. \tag{3.43}$$

Eq. (3.43) is often referred to as Rothwarf-Taylor equation [76]. It is composed of a quasiparticle injection rate

$$I^{qp}_n = \int d\xi \sum_r \left[w^r_{n+1,n}(E,t) + w^r_{n-1,n}(-E,t)\right], \tag{3.44}$$

which is independent on the quasiparticle number, furthermore an escape-rate which accounts for the tunneling of quasiparticles into the leads, i.e.

$$\Gamma^{qp}_n = \frac{1}{2\mathcal{N}_F\mathcal{V}}\sum_r\sum_{s=\pm1}[w^r_{n+s,n}(\Delta) + w^r_{n+s,n}(-\Delta)] \tag{3.45}$$

and a recombination rate given by κN_{qp}. As long as quasiparticles are injected close to the gap, Δ, and as long as the quasiparticle-number conserving relaxation channels are

fast enough, Eq. (3.43) accounts appropriately for the quasiparticle dynamics in the superconductor. This is true even in the regime where the parity effect becomes important, which will be discussed at the end of this chapter.

Superconducting gap

Although we consider a non-equilibrium situation we neglect variations of the superconducting gap. With regard to section 2.2 the correction of the gap due to the presence of quasiparticles is given by

$$\frac{\delta\Delta_{\mathrm{even/odd}}}{\Delta} \approx -\frac{2N_{\mathrm{qp}}}{\mathcal{N}_F\mathcal{V}\Delta}[\tanh(N_{\mathrm{qp}}]^{\pm 1}. \tag{3.46}$$

According to Table 3.1 the number of Cooper-pairs is of the order $\mathcal{N}_F\mathcal{V}\Delta \sim 2\times 10^4$, which is way larger than the average quasiparticle numbers N_{qp} considered here. Therefore the correction (3.46) is negligible.

3.2.3. Tunneling current

The experimental observable in the single turnstile experiment is the current through lead r given by the time-derivative of the electronic charge, i.e.

$$I_r = e\left\langle \frac{d}{dt}\sum_{k\sigma} c^\dagger_{k\sigma}c_{k\sigma}\right\rangle = ie\left\langle {\sum_{p,\alpha\beta}}' \alpha H^{\alpha\beta}_{p\sigma}\right\rangle \tag{3.47}$$

with $H^{\alpha\beta}_{k\sigma}$ as defined in (3.17). The prime indicates that exclusively tunneling events from and to lead r are considered. Within the Born-Markov approximation considered before we obtain

$$\begin{aligned} I_r(t) &= -e\int_{-\infty}^{t} dt' {\sum_{k\sigma,\alpha\beta}}' \mathrm{Tr}(\alpha H^{\alpha\beta}_{k\sigma}(t)[H^{\bar\alpha\bar\beta}_{k\sigma}(t'),\hat\rho(t)]),\\ &= -2e\mathrm{Re}\int_{-\infty}^{t} dt' {\sum_{k\sigma,\alpha\beta}}' \mathrm{Tr}(\alpha H^{\alpha\beta}_{k\sigma}(t)H^{\bar\alpha\bar\beta}_{k\sigma}(t')\hat\rho(t)). \end{aligned} \tag{3.48}$$

which is very similar to (3.18). This means that the current can be expressed in terms of the transition rates (3.42), i.e.

$$I_r(t) = e\sum_n [\Gamma^r_{n+1,n}(t) - \Gamma^r_{n-1,n}(t)]\, p_n(t). \tag{3.49}$$

According to Eq. (3.42) the current is directly related to the number of quasiparticle excitations. Therefore the current is a direct measure of the quasiparticle dynamics.

Frequency dependence

An important issue in the field of metrology and quantum information is the dependence of quasiparticle poisoning on the repetition-ration of performed operations. In the context of superconducting qubits this issue has been addressed for instance by Wenner *et al.*[3].

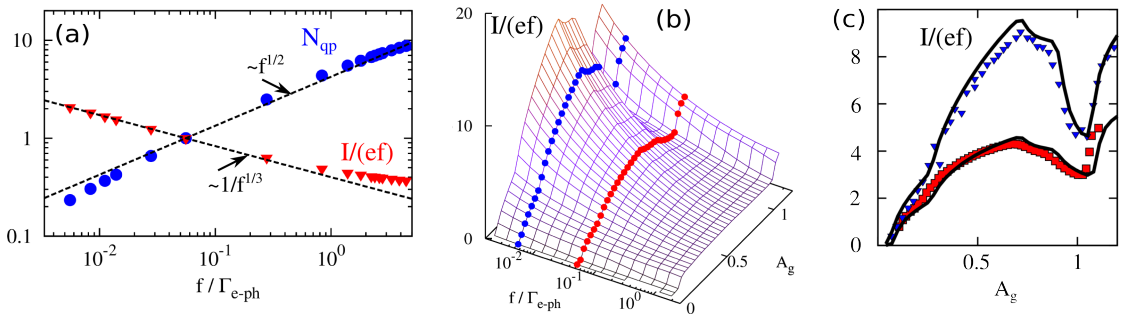

Figure 3.9.: (a) Frequency dependence of $\langle N_{qp}\rangle$ and $\langle I/(ef)\rangle$. (b) Variation of current with gate-amplitude. The red and the blue line indicate the two frequencies $f_1 = 5.56\times10^{-2}\Gamma_{e-ph}$ and $f_1 = 5.56\times10^{-3}\Gamma_{e-ph}$. The latter are compared to the experimental data of Ref. [9] presented by blue and red dots in (c). Here the black solid lines show the theoretical simulation. Figure from Ref. [61].

In their experiment quasiparticles were injected into a qubit circuit by a nearby squid. Fig. (3.1)(c) shows the dependence of qubit relaxation rate on the injected quasiparticle density. The advantage of the turnstile experiment certainly is the straight connection of tunneling current as the experimental observable and the injection of quasiparticles. As we have seen, this makes it easier to formulate a theoretical model based on which the comparison to experiment can be performed. In turnstile experiments there is an upper frequency for the turnstile experiments below which the error of missing a tunneling event is sufficiently suppressed. In the following we will stay well below this limit given by $2\pi f_c \sim \Delta/e^2R_T$.

In Fig. 3.9 we investigate the frequency dependence of $\langle N_{qp}\rangle$ and $\langle I/(ef)\rangle$: First of all, panel (a) shows that the quasiparticle number is limited by quasiparticle recombination at large frequency. Here the recombination term $\langle\kappa N_{qp}^2\rangle$ in (3.43) dominates over the escape rate $\langle\Gamma_n^{qp}\mathcal{A}_n N_{qp}\rangle$. Furthermore the injection of quasiparticles scales linearly with frequency, which leads to the result $\langle N_{qp}\rangle \propto f^{1/2}$ and agrees approximately well for frequencies $f \gtrsim 0.1\Gamma_{e-ph}$. Interestingly the normalized current $\langle I/(ef)\rangle$ tends to a constant in this frequency-limit, although the quasiparticle number is increased. The can be understood in the following way: The tunneling rates (3.42) that enter the expression for the current (3.48) consist of a term proportional to N_{qp} and a term independent on the quasiparticle number. The latter scales linearly with frequency leading to a constant fraction $\langle I/(ef)\rangle \approx 1$ in the ideal case of vanishing N_{qp}. The term proportional to N_{qp} scales with $\sim f^{-1/2}$ and is thus suppressed with increasing frequency.

In addition to that the normalized current assumes a step-like behavior as a function of gate-amplitude A_g in the high frequency limit (see Fig. 3.9(b)). This makes it interesting in particular for metrological purpose. With decreasing frequency the quasiparticle contribution becomes important rendering the single electron turnstile sensitive to the quasiparticle dynamics. In Fig. 3.9(c) we compare the theoretical predictions with experimental data from Ref. [9] for two different frequencies and indeed find good agreement with our model.

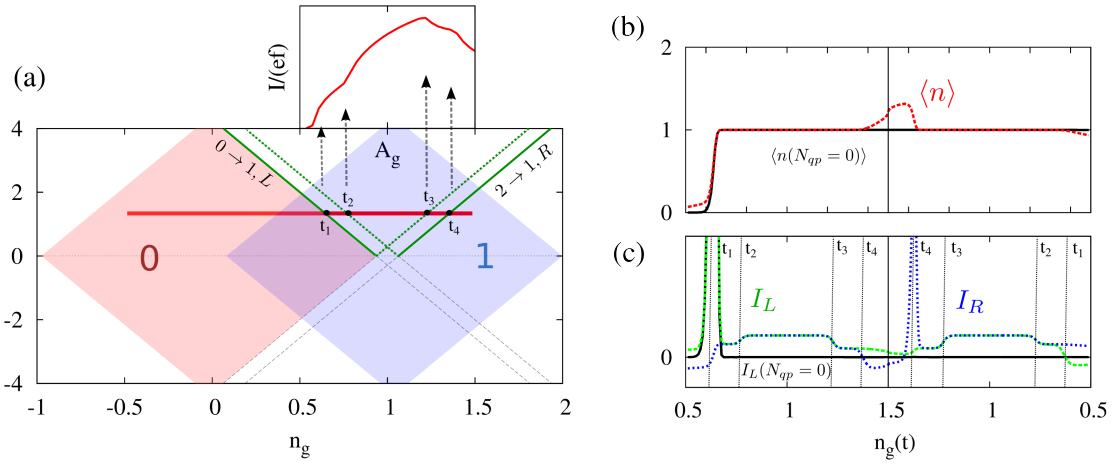

Figure 3.10.: (a) Stability diagram for $E_C > \Delta$. During the turnstile protocol the gate-offset crosses various thresholds beyond which tunneling processes are activated. This leads to the characteristic line-shape of the current, shown in the inset. (b) Average charge on the dot for finite (red) and vanishing (black) quasiparticle number as a function of normalized gate-charge within the first half of the turnstile cycle. (c) Current through the left (green) and the right (blue) lead for finite N_{qp} along the time-instances $t_1 - t_4$. The current I_L for vanishing quasiparticle is shown by the black curve.

Dependence on driving amplitude

In order to understand the characteristic dependence of the average current on gate - amplitude we refer to Fig. 3.10(a), which shows the stability diagram for the case $E_C > \Delta$. The gate charge is varied along the red line, which passes through the overlap of the Coulomb diamonds of charging state 0 and 1. The thresholds for the particular transition-rates (3.42) are indicated by green lines. In particular the thresholds for vanishing quasi-particle number are given by solid green lines. In panel (b) and (c) we follow the first half of the turnstile cycle along the time-instances $t_1 - t_4$ with a gate-amplitude $A_g = 1$:

1. At the time instant t_1 a charge is injected into the island changing the average charge $\langle n \rangle$ from zero to one. The rapid increase of the current I_L indicates that the charge tunnels through the left junction.

2. Assuming that the quasiparticle number is vanishing we find that the current through the left lead [black solid line in panel (c)] is zero for the rest of half the turnstile-cycle. The same is true for the current through the right lead. For a finite amount of quasiparticles the situation is different. The quasiparticle dependent term in the tunneling-rates (3.42) allows for additional forward-tunneling when the normalized gate-charge passes through the indicated threshold at t_2. This onset also imprints on the average current sketched in panel (a).

3. Later at $t = t_3$ the forward-tunneling is reduced leading to a decrease of the average current. Finally at the time t_4 there is a back-flow of charge through the right junction. This is also reflected in the negative current I_R as well as the slight increase of the average charge on the dot (see panel (b)).

4. Finally, at $n_g(t = 1/4f) = 1.5$ the gate-variation changes its direction. The time-instances now follow chronologically the order $t_4 < t_3 < t_2 < t_1$. At t_4 the

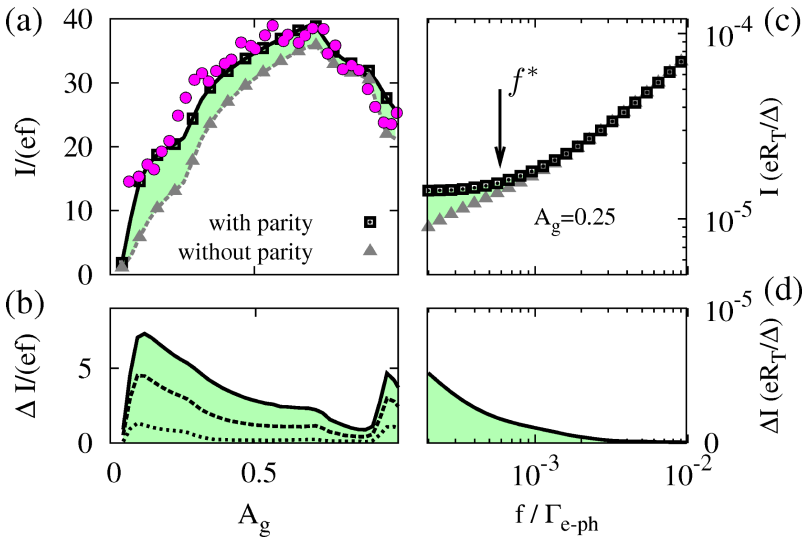

Figure 3.11.: The influence of the parity effect on the current. (a) Theoretical predictions for the current $\langle I\rangle$ with the parity effect included (black rectangles) and its value $\langle I^*\rangle$ obtained from setting $\mathcal{A}_n = 1$ (gray triangles). The simulations are compared with the experimental data of Ref. [9] (magenta dots) for a operation frequency $f = 2\times10^{-4}\Gamma_{e-ph}$. (b) The difference $\langle\Delta I\rangle = \langle I\rangle - \langle I^*\rangle$ for three different pumping frequencies $f = 2,\ 2.7,$ and $5.4\times10^{-4}\Gamma_{e-ph}$ (solid, dashed, and dotted lines, respectively). (c) and (d) show the frequency dependence of $\langle I\rangle$, $\langle I^*\rangle$ and $\langle\Delta I\rangle$. (Figure from [61])

gate-charge crosses the threshold of the transition rate $\Gamma^R_{2\to1}$ which explains the rapid increase of the current through the right lead which neutralizes the additional excess charge on the island.

We conclude that the characteristic line-shape of the average current through the turnstile follows from (i) the particular dependence of the quasiparticle independent transition rates on bias voltage and gate-charge and (ii) from the increase of forward and backward-tunneling due to the presence of non-equilibrium quasiparticles.

3.2.4. Parity effect

In this paragraph we draw attention to parity that has been discussed for the equilibrium situation in section 2.2. Remember that in this case the presence of an additional unpaired quasiparticle on the superconducting island led to a finite current plateau which is 2e-periodic in gate voltage [see Fig. 2.5].

In the case of the driven single-electron turnstile we find that the number of quasiparticles decreases with operation frequency f [see Fig. 3.9(a)]. For a characteristic frequency the injection of quasiparticles is compensated by their recombination and single-quasiparticle physics becomes important. In order to resolve the contribution of the parity effect to the average current, we first solve the master-equation (3.23) together with the kinetic equation (3.43) by setting $\mathcal{A}_n = 1$. The result is presented in Fig. 3.11(a) by the gray triangular dots. The disagreement with the experimental data indicates an additional current contribution. This can be accounted for by using the parity dependence of $\mathcal{A}_n$, which allows a much better fit of the experimental data (black rectangular dots). The difference between exact current $\langle I\rangle$ and its value $\langle I^*\rangle$ derived under the assumption that $\mathcal{A}_n = 1$,

i.e. $\langle \Delta I \rangle = \langle I \rangle - \langle I^* \rangle$, is presented in Fig. (3.11)(b) for three different frequencies. With decreasing frequency the parity effect first develops at small gate-amplitudes. In panels (c) and (d) the frequency dependence of the current is presented.

In analogy to the equilibrium experiments, where the quasiparticle number is controlled by temperature and a crossover to the parity effect is observed below a characteristic temperature T^* [see Fig. 2.4] we find such a transition at a frequency $f^* \sim 4\kappa$, which corresponds to the recombination rate of two quasiparticles.

Part II.

Topological superconductivity from magnetic adatoms on top of superconductors

4. Basics: Topological superconductivity

The second part of this thesis discusses aspects of topological superconductivity. More precisely we investigate the possibility to engineer a topological superconductor (TSC) by positioning adatoms on a superconducting surface. A minimal model for a TSC would be a p-wave superconductor with spin-triplet paring. In such a superconductor quasiparticle-excitations are combinations of electrons and holes and the quasiparticle excitation operator is given by

$$\gamma_k^\dagger = u_k c_k^\dagger + v_k c_{-k}. \tag{4.1}$$

Here, for the sake of simplicity, we only considered fully spin-polarized operators, $c_k^\dagger$, which create electrons with momentum k. Charge-conjugation symmetry implies that creating a quasiparticle with energy E_k by the operator $\gamma_k^\dagger(E_k)$, is equivalent to creating a hole with the energy $-E_k$ by the operator $\gamma_{-k}(-E_k)$. If we consider a *gap closing* at the inversion symmetric point $k = 0$, i.e. $E_0 = 0$, we obtain the relation

$$\gamma_0^\dagger = \gamma_0, \tag{4.2}$$

which is the defining condition for a *Majorana operator*. In fact, it turns out that closings of the excitation-gap between particle and hole bands are intimately related to the emergence of zero-energy states in real space. Each of these states decomposes into two fractions, which appear at the edges of a finite system and can be described by Majorana operators, e.g., γ_1 and γ_2. Together they constitute an ordinary quasiparticle excitation $d = \gamma_1 + i\gamma_2$. Although Majorana operators fulfill the fermionic commutator relations, they are by no means ordinary fermions. Nevertheless it has become established in the condensed matter community to call these excitations *Majorana fermions*.

In the following section we will provide a short introduction to the field of topological phases in condensed matter. For a more elaborate discussion we refer the reader to Refs. [77, 78]. We will start with the main concepts of topology in bandstructure theory and discuss the simplest low-dimensional examples of topological insulators and superconductors. Furthermore, we will explain the emergence of zero-energy states and Majorana fermions in these systems. Later, in chapter 5, we will discuss two alternative ways

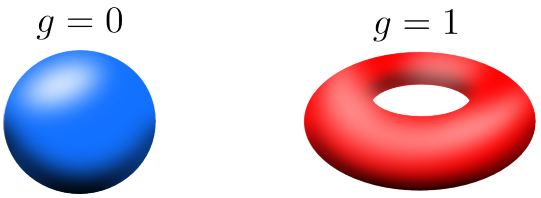

Figure 4.1.: Two-dimensional surfaces in three-dimensional space can be topologically classified by their genus g, which essentially counts the number of holes in the three-dimensional object.

how to realize Majorana fermions from collinear magnetic chains on top of conventional superconductors. This will constitute the second main part of this thesis.

4.1. Topology in condensed matter

In mathematics topology is the study of manifolds and mappings between them. A mapping is called homotopic if geometric objects can be continuously deformed into each other. Two-dimensional surfaces in a three-dimensional space, for instance, can be topologically classified by their genus, g, which essentially counts the number of holes in the three-dimensional object. Let us for instance consider the two objects in Fig. 4.1, a sphere and a torus. The sphere has no holes corresponding to a genus $g = 0$. We call the mapping from the two-dimensional parameter-space to the three-dimensional configuration space topologically *trivial*. On the other hand, the torus has one hole and therefore genus of $g = 1$. This object is topologically distinct from the sphere and we call it topologically *non-trivial*. Mathematically the surface integral over the Gauss-curvature $\varkappa$ offers a relation between the surface and its *topological index* g,

$$\oint dA\, \varkappa = 4\pi(1-g). \tag{4.3}$$

Obviously for the sphere $\varkappa$ equals $1/r^2$, where r is the radius of the sphere and the integral (4.3) gives 4π. Two objects are called *topologically equivalent* when they can be continuously deformed into one another without altering the number of holes. In condensed matter there exists a similar classification scheme in the theory of band-insulators. In this context gapped bandstructures are topologically equivalent if they can be continuously deformed into one another without closing the energy gap. The underlying ingredient of a bandstructure is a periodic lattice in real space. According to Bloch's theorem [79] an electron in a periodic potential has a wavefunction of the form

$$|\psi_{n\boldsymbol{k}}\rangle = e^{i\boldsymbol{k}\hat{r}}\,|u_{n\boldsymbol{k}}\rangle\,, \tag{4.4}$$

where the Bloch-functions $\langle r|u_{n\boldsymbol{k}}\rangle$ have the periodicity of the lattice and are eigenfunctions of the Bloch-Hamiltonian $H(\boldsymbol{k}) = \exp(-i\boldsymbol{k}r)\, H\, \exp(i\boldsymbol{k}r)$ with eigenvalues $E_n(\boldsymbol{k})$ and carry the band-index n. The information on whether the mapping from the Brillouin-zone (BZ) to $H(\boldsymbol{k})$ is topologically trivial or not, is hidden in the Bloch-functions $|u_{n\boldsymbol{k}}\rangle$ which acquire a Berry-phase

$$\gamma_n = \oint_{\partial\mathcal{S}} d\boldsymbol{k}\cdot\mathcal{A}_{n\boldsymbol{k}}, \tag{4.5}$$

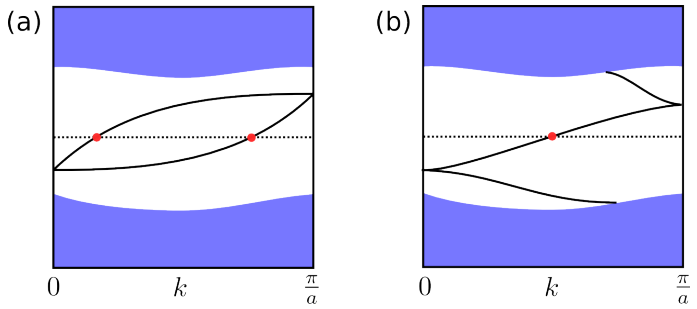

Figure 4.2.: Kramer's degeneracy at the inversion symmetric points $k = 0$ and $k = \pi/a$ implies two scenarios for the edge state of an insulator: (a) The edge-dispersion intersects at even number of points in-between 0 and π/a. This would be the topologically non-trivial case, as the bands could be pushed below the Fermi-surface. (b) The edge-dispersion intersect an odd number of times. The node can not vanish under any kind of smooth deformation of the bandstructure. Thus in this case one expects the appearance of a zero-energy edge state.

with the Berry vector potential $\mathcal{A}_{n\boldsymbol{k}} = \langle u_{n\boldsymbol{k}}| - i\nabla_k |u_{n\boldsymbol{k}}\rangle$. Under a closed path the Bloch-function remains single valued if the Berry phase is a multiple of $2\pi i$. In two dimensions, using Stokes theorem, Eq. (4.5) can be expressed by the Berry curvature $\mathcal{F}_{n\boldsymbol{k}} = \nabla_{\boldsymbol{k}} \times \mathcal{A}_{n\boldsymbol{k}}$, i.e.,

$$\mathcal{N}_n = \frac{1}{2\pi} \int_{\mathcal{S}} d^2\boldsymbol{k}\, \hat{n} \cdot \mathcal{F}_{n\boldsymbol{k}}. \tag{4.6}$$

$\mathcal{N}_n$ is quantized and defines a topological $\mathbb{Z}$-invariant. The prime example of a topological non-trivial insulator is the integer quantum Hall effect (IQHE). By comparing Eq. (4.6) with the Kubo-formula for the quantum Hall conductance

$$\sigma_{xy} = \frac{e^2}{h} \sum_n \frac{1}{2\pi} \int_{\mathrm{BZ}} d^2\boldsymbol{k}\, \hat{n} \cdot \mathcal{F}_n, \tag{4.7}$$

one immediately finds that the conductance must be a multiple of the conductance quantum e^2/h, i.e. $\sigma_{xy} = e^2\mathcal{N}/h$ with the *topological invariant* $\mathcal{N} = \sum_n \mathcal{N}_n$. At the interface of two topologically distinct materials the energy-gap has to be necessarily closed in order to pass from one topological phase to the other. This unavoidably leads to a zero-energy states at the interface. In the IQHE the number of these edge-modes is given by the *Chern number* (4.6). The direct relation between bulk invariant and the appearance of zero energy edge states is an important concept in the classification of topological insulators and superconductors and is termed *bulk-boundary correspondence*.

The quantum Hall insulator is a time-reversal (TR) symmetry breaking topological insulator. However there also exist TR *invariant* topological insulators. TR symmetry is represented by the anti-unitary operator

$$\Theta = e^{i\pi J_y} \mathcal{K}, \tag{4.8}$$

with the total angular momentum J_y ($\hbar = 1$) and the complex conjugation $\mathcal{K}$. For s-orbital electrons the TR operator is given by $\Theta = i\sigma_y \mathcal{K}$. According to that $\Theta^2 = -1$, which has the important implication that the band-structure at inversion-symmetric points in the BZ

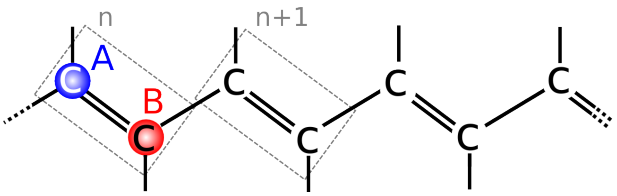

Figure 4.3.: Polyacetylene $[C_2H_2]_n$: We define a two-atomic unit-cell which accounts for different next-nearest neighbour hoppings induced by a Peierls' instability.

(for one dimension $k = 0$ and π/a) exhibits a two-fold degeneracy, known as Kramer's theorem. If a state $|\psi\rangle$ would not be degenerate this would imply that $\Theta^2 |\psi\rangle = t^2 |\psi\rangle$ for some real constant t, which contradicts with $t^2 = -1$. In the absence of spin-orbit coupling (SOC) Kramer's degeneracy is simply the degeneracy between spin-up and spin-down bands, which persists even away from the inversion symmetric points. In contrast *with* SOC the two spin-bands split away from inversion symmetric points. The latter is illustrated in Fig. 4.2 which shows two possible scenarios of edge-state dispersions between Kramer's degenerate points in the BZ. In (a) the dispersions intersect the Fermi-surface an even number of times. In the spirit of topological classification one could argue that a smooth deformation of these bands could push them above the Fermi-level. Consequently this would correspond to an ordinary insulator. However if the dispersions intersect an odd number of times like in (b) a deformation of the bandstructure would at least lead to one crossing and the existence of a zero energy bound state characterizing a topological insulator. We conclude that edge modes are protected from opening a gap by TR invariance if and only if their number is odd. This interpretation suggests that the topological invariant reflects this even-odd distinction and should be of $\mathbb{Z}_2$-type.

According to Fu and Kane [80] this invariant may be related to the matrix $\mathcal{W}_{mn}(\boldsymbol{k}) = \langle u_m(\boldsymbol{k})|\Theta|u_n(-\boldsymbol{k})\rangle$ which contains the TR operator Θ and is anti-symmetric at inversion symmetric points, i.e. $\mathcal{W}_{mn}(\boldsymbol{k}) = -\mathcal{W}_{nm}(-\boldsymbol{k})$ (in 1 dimension for $k = 0, \pi$). A skew-symmetric matrix has the property that one can define a Pfaffian which satisfies the relation $\mathrm{Pf}^2(\mathcal{W}) = \det(\mathcal{W})$. The topological $\mathbb{Z}_2$ invariant, e.g. for one dimension, is given by

$$\mathcal{M} = \frac{\mathrm{Pf}[\mathcal{W}(0)]}{\sqrt{\det[\mathcal{W}(0)]}} \frac{\mathrm{Pf}[\mathcal{W}(\pi)]}{\sqrt{\det[\mathcal{W}(\pi)]}}, \tag{4.9}$$

and changes sign when passing from a topological trivial to a non-trivial phase. Mind that the $\mathbb{Z}_2$-invariance is a direct consequence of Kramer's degeneracy which arises due to the fact that $\Theta^2 = -1$.

However there could be also a case where the Hamiltonian assumes TR symmetry but $\Theta^2 = 1$. In the following we will consider the prototype example of a topological insulator in one dimension, namely polyacetylene $[C_2H_2]_n$, which fulfills this condition and is sketched in Fig. 4.3. This consideration will be conceptually similar to the discussion that we will pursue in section 5.1.2. The Hamiltonian for this system reads [81],

$$H = \sum_n t\, c^\dagger_{An} c_{Bn} + t'\, c^\dagger_{An+1} c_{Bn} + H.c. \tag{4.10}$$

A Peierls' instability leads to a finite difference in hopping amplitude $\delta t = t - t'$. In momentum space the Hamiltonian can be written in the convenient form

$$H(k) = \boldsymbol{g}(k) \cdot \boldsymbol{\sigma}, \tag{4.11}$$

with σ being a Pseudo-spin which subscribes the two sublattices A and B and where the vector $\boldsymbol{g}$ decomposes into $g_x(k) = t + t' \cos(k)$ and $g_y(k) = t' \sin(k)$ and $g_z = 0$. The energy spectrum can be readily calculated, giving

$$E_k = \pm\sqrt{2}\sqrt{(t + t' \cos(k))^2 + t'^2 \sin^2(k)}. \tag{4.12}$$

A gap closing appears only at inversion symmetric points $k = 0, \pi$ for the particular condition $t = t'$. Therefore one expects that the two phases $\delta t > 0$ and $\delta t < 0$ are topologically distinct. The Berry functions can be readily obtained by defining the winding angle φ_k via $\tan(\varphi_k) = g_y(k)/g_x(k)$, i.e.

$$|u_\pm(k)\rangle = \frac{1}{\sqrt{2}} \begin{pmatrix} \pm 1 \\ e^{i\varphi_k} \end{pmatrix}. \tag{4.13}$$

The associated Berry vector potential is given by $\mathcal{A}_\pm = \langle u_\pm(k)| - i\partial_k |u_\pm(k)\rangle = \partial_k \varphi_k / 2$. With this it is possible to define a topological $\mathbb{Z}$ invariant

$$\mathcal{N} = \frac{1}{2\pi} \int_{-\pi}^{\pi} dk\, \partial_k \varphi_k = -\frac{1}{2\pi} \int_{-\pi}^{\pi} dk\, [\hat{\boldsymbol{g}}(k) \times \partial_k \hat{\boldsymbol{g}}(k)] \cdot \hat{z}. \tag{4.14}$$

This invariant counts how often the normalized vector $\hat{\boldsymbol{g}}(k) = \boldsymbol{g}(k)/|\boldsymbol{g}(k)|$ *winds* around the origin. In Fig. 4.4 we distinguish two scenarios:

1. For $\delta t > 0$ we find a winding of zero, which tells that the system is topologically trivial. This can be understood by considering the extreme case $t \gg t'$, when the energy-bands (4.12) are flat and $\hat{\boldsymbol{g}}(k) \approx (1,\, 0,\, 0)$.

2. In the other extreme limit $t \ll t'$ we have $\hat{\boldsymbol{g}}(k) \approx (\cos(k),\, \sin(k),\, 0)$, therefore the vector $\hat{\boldsymbol{g}}$ winds ones around the origin yielding $\mathcal{N} = 1$. More generally, because a topological phase transition can only occur at $\delta t = 0$, the topological invariant has to be one for $\delta t < 0$.

Mind that in the present case the TR operator is given by $\Theta = \mathcal{K}$ and therefore $\Theta^2 = 1$. Furthermore the Hamiltonian $H(k)$ assumes a charge-conjugation symmetry $\{\Xi, H\} = 0$, represented by the operator $\Xi = \sigma_z \mathcal{K}$. If both symmetries, time-reversal and charge-conjugation, are present one can define a new symmetry, $\{\Pi, H\} = 0$, which is called chiral symmetrya and represented by the unitary operator $\Pi = \Xi\Theta = \sigma_z$.

At this point it is reasonable to comment on the classification scheme of Hamiltonians by their symmetry and dimensionality [82]. The symmetry class is determined by the presence or absence of time-reversal, charge-conjugation and chiral symmetry. One can distinguish the cases $\Theta^2 = (0,\, \pm 1)$, $\Xi^2 = (0,\, \pm 1)$ and $\Pi^2 = (0,\, 1)$, where the zero indicates the absence of the respective symmetry. This defines ten symmetry classes, whose classification is specified by a $\mathbb{Z}$, $\mathbb{Z}_2$ or none invariant, depending on the dimension. We observe that in the case of polyacetylene $\Theta^2 = \Xi^2 = 1$ such that polyacetylene falls into class BDI which in 1D has a $\mathbb{Z}$ invariant as we have seen in Eq. (4.14).

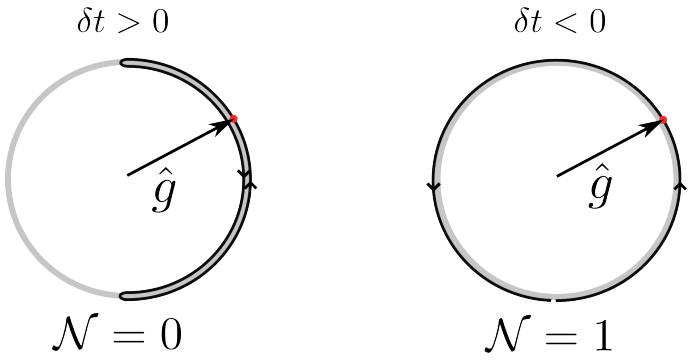

Figure 4.4.: *Winding* of the normalized vector $\hat{\boldsymbol{g}}$ in Eq. (4.11). There are two topologically distinct phases determined by $\delta t \lessgtr 0$.

4.2. One-dimensional topological superconductors

Topological superconductors fall into the same classification scheme like topological insulators. In this section we start with the basic example of a one-dimensional topological superconductor, namely the spinless p-wave superconductor. We will see that this system bears similarities with polyacetylene, which we have investigated earlier. This allows for a direct classification of this system and for the exploration of the different topological phases. In addition we discuss a very pedagogical illustration of the emergence of Majorana fermions in coordinate space, known as Kitaev's chain model. For the sake of completeness we give an overview of some Majorana platforms that have been proposed so far and which stimulated already a number of experiments. Thereafter we move on to the discussion of how to realize a topological superconductor from magnetic atoms placed on a conventional superconductor.

4.2.1. 1-D spinless p-wave superconductor

Let us consider a one-dimensional wire with spinless fermions. One could think of fermions which are fully spin-polarized due to the presence of a strong TR breaking magnetic field. In momentum space the Hamiltonian for a simple nearest-neighbour hopping model is given by

$$H = \frac{1}{2}\sum_k \psi_k^\dagger \big([2t\cos(k) - \mu]\tau_z - 2\Delta_p \sin(k)\tau_y\big)\psi_k, \tag{4.15}$$

where we introduced the spinor $\psi_k^\dagger = (c_k^\dagger, c_{-k})$ and the Pauli-matrices τ_i acting in particle-hole space. Furthermore t is the nearest-neighbor hopping amplitude, μ the on-site chemical potential and Δ_p the p-wave pairing amplitude. Mind that the p-wave symmetry manifests itself in the fact that $\Delta_p \sin(k)$ is odd under inversion. Because of the antisymmetry of the fermion wavefunction the spin-component is triplet. The bulk-dispersion can be readily calculated, giving

$$E_k = \pm\sqrt{[2t\cos(k) - \mu]^2 + 4\Delta_p^2 \sin^2(k)}. \tag{4.16}$$

We find that it has substantial similarity to the dispersion of polyacetylene given in Eq. (4.12). Furthermore, the Hamiltonian can be written in the convenient form

$$H(k) = [2t\cos(k) - \mu]\tau_z - 2\Delta_p \sin(k)\tau_y = \hat{\boldsymbol{g}}(k)\cdot\boldsymbol{\tau}, \tag{4.17}$$

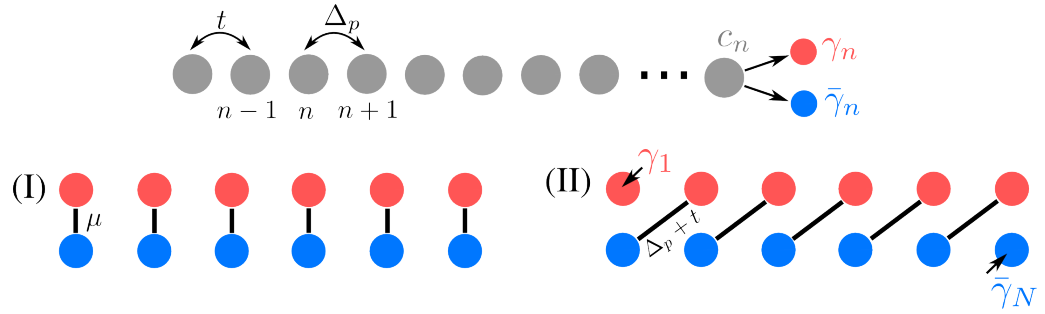

Figure 4.5.: Kitaev's chain: A decomposition of fermion operators c_n into Majorana operators γ_n and $\bar{\gamma}_n$ is performed. We consider two situations, (I) $\Delta_p = t = 0$ and $\mu \neq 0$ and (II) $\Delta_p = t \neq 0$ and $\mu = 0$. In the first case the chain is a conventional insulator and the Majorana-operators on each lattice cite pair and give a conventional fermion $c_n = (\gamma_n + i\bar{\gamma}_n)/2$. In the second case on-site pairing is omitted, but fermion operators $\tilde{c}_n = (\gamma_{n+1} + i\bar{\gamma}_n)/2$ can be defined, each such excitation contributing an on-site energy and pairing amplitude $\Delta_p + t$. Furthermore the two Majorana fermion operators γ_1 and $\bar{\gamma}_N$ remain unpaired. The occupation of the strongly delocalized fermion state with creation operator $d^\dagger = (\gamma_1 - i\bar{\gamma}_N)/2$ yields zero energy.

with $g_y(k) = -2\Delta_p \sin(k)$ and $g_z(k) = [2t\cos(k) - \mu]$. Just as in the case of polyacetylene we identify the TR symmetry $\Theta = \mathcal{K}$, the particle-hole symmetry $\Xi = \tau_x\mathcal{K}$ and the chiral symmetry $\Pi = \Xi\Theta = \tau_x$ with $\Theta^2 = \Xi^2 = \Pi^2 = 1$. Thus, the Hamiltonian (4.17) falls into the symmetry class BDI which has a $\mathbb{Z}$-invariant as defined in Eq. (4.14). Like before we identify two topological phases, the topological trivial phase with the topological invariant $\mathcal{N} = 0$ for $|\mu| > 2t$ and the non-trivial phase for $|\mu| < 2t$ with $\mathcal{N} = 1$. The phase-transition occurs at $\mu| = 2t$ and coincides with the gap closing of the dispersion (4.16) at $k = 0$.

In order to show that the topological non-trivial phase is related to the emergence of Majorana zero energy states, let us consider the finite system of the one-dimensional p-wave superconductor. On the real lattice the Hamiltonian (4.15) reads

$$H = -\mu \sum_{n=1}^{N} c_n^\dagger c_n + \sum_{n=1}^{N-1} \left[t c_{n+1}^\dagger c_n + \Delta_p c_{n+1} c_n + H.c. \right]. \tag{4.18}$$

Here $c_n^\dagger$ creates an electron on site n. Now, we introduce the Majorana operators γ_n and $\bar{\gamma}_n$, which fulfill the fermionic commutator relations $\{\gamma_n, \gamma_m\} = \delta_{nm}$, $\{\bar{\gamma}_n, \bar{\gamma}_m\} = \delta_{nm}$ and $\{\bar{\gamma}_n, \gamma_m\} = 0$. It is straightforward to show that the fermionic operators c_n can be expressed by the Majorana operators, i.e. $c_n = (\gamma_n + i\bar{\gamma}_n)/2$, and obey the commutator relations $\{c_n, c_m^\dagger\} = \delta_{mn}$. Thus, the Hamiltonian can be expressed in terms of Majorana operators,

$$H = -\frac{\mu}{2} \sum_{n=1}^{N} (1 - i\bar{\gamma}_n \gamma_n) - \frac{i}{2} \sum_{n=1}^{N-1} \left[(\Delta_p + t)\gamma_{n+1}\bar{\gamma}_n + (\Delta_p - t)\bar{\gamma}_{n+1}\gamma_n \right]. \tag{4.19}$$

Next, we may consider two limits, which are illustrated in Fig. 4.5:

(I) We set $\Delta_p = t = 0$ but with the chemical potential finite, providing

$$H = -\frac{\mu}{2} \sum_{n=1}^{N} (1 - i\bar{\gamma}_n \gamma_n). \tag{4.20}$$

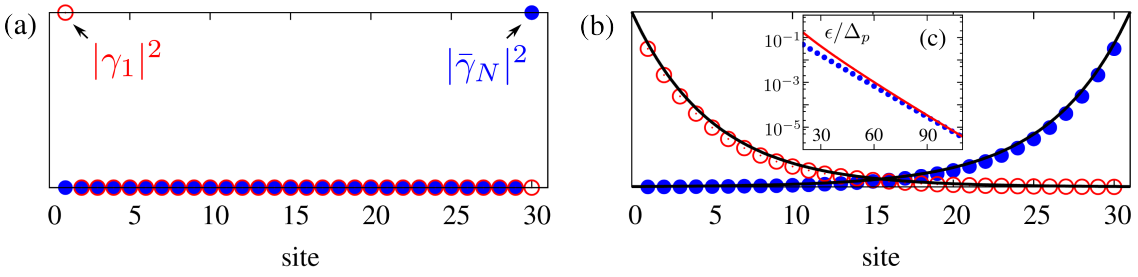

Figure 4.6.: Wave-functions for the Kitaev chain: (a) $\Delta_p = t$ and $\mu = 0$ – As illustrated in Fig. 4.5 (II) the two Majorana fermions are localized at single sites at the end of the chain. (b) $\Delta_p = t$ and $\mu = 1.8\,t$ – The Majorana wavefunctions leak into the bulk and have a finite overlap. The black lines show the analytical result of Eq. (4.24). (c) Finite energy associated with the bound state presented in (b). Blue dots show the numerical result as a function of chain-length, the red line is the analytical approximation (4.25).

Majorana fermions pair on-site and form a conventional fermion c_n. Occupying this state contributes an energy $-\mu$. It is obvious that the Hamiltonian describes nothing but a trivial insulator, in this case with a flat band. We might have expected this already from our classification before, which tells that we are in a special limit of the topologically trivial phase, $|\mu| > 2t$.

(II) In the second limit we consider $\Delta_p = t \neq 0$ and $\mu = 0$ which falls into the topologically non-trivial phase, as $|\mu| < 2t$,

$$H = -i\frac{\Delta_p + t}{2}\sum_{n=1}^{N-1} \gamma_{n+1}\bar{\gamma}_n. \tag{4.21}$$

The on-site pairing of Majorana operators is omitted, but we may likewise define fermion-operators $\tilde{c}_n = (\gamma_{n+1} + i\bar{\gamma}_n)/2$. With this the Hamiltonian reads

$$H = -\frac{\Delta_p + t}{2}\sum_{n=1}^{N-1} \left[2\tilde{c}_n^\dagger \tilde{c}_n - 1\right], \tag{4.22}$$

i.e. the Hamiltonian describes a fermion lattice with on-site energy $\Delta_p + t$. Mind that the Majorana operators γ_1 and γ_N do not appear in the Hamiltonian. This means that they are unpaired and have zero-energy. This simple example shows that Majorana excitations in condensed matter appear by fractionalization of quasiparticles. In this particular case we may define the fermion operator $d = (\gamma_1 + i\gamma_N)/2$, which splits into the two Majorana fractions $\gamma_1 = d + d^\dagger$ and $\gamma_N = (d - d^\dagger)/2i$.

Away from the ideal situation (II) but still within the non-trivial topological phase, the wavefunctions start to *leak* into the bulk. In Fig. 4.6(b) we show a situation which is close to the topological phase transition ($\mu = 1.8\,t$). The Majorana wavefunctions are exponentially suppressed in this case. To understand this behavior we take a look at Eq. (4.17) and derive the bound state wavefunction. We solve the Bogolioubov de Gennes equation $H(k)\phi_k = E_k\phi_k$ for zero energy and near $k = 0$, where the gap closing appears. First of all the condition $E_k = 0$ yields $k \approx \pm i|\mu - 2t|/2\Delta_p$. Furthermore, the particle-hole amplitudes are governed by the equation

$$\left\{[2t - \mu] + i2\Delta_p\, k\, \tau_x\right\}\phi_k = 0, \tag{4.23}$$

which shows that ϕ_k are eigenfunctions of τ_x. On the lattice the wavefunction is determined by $\phi_n = \exp(ikn)\phi_k$. Taking into account the appropriate boundary conditions we obtain the left-sided and right-sided wavefunctions

$$\phi_{nL} \approx \frac{1}{\sqrt{\beta}} e^{-\beta(n-1)} \begin{pmatrix} 1 \\ 1 \end{pmatrix} \qquad \text{and} \qquad \phi_{nR} \approx \frac{1}{\sqrt{\beta}} e^{\beta(n-N)} \begin{pmatrix} 1 \\ -1 \end{pmatrix} \tag{4.24}$$

with the normalization factor $\beta = 2\Delta_p/|\mu - 2t|$. The particle and hole components in ϕ_{nL} and ϕ_{nR} have the same weight, this implies that each wave function corresponds to a single Majorana fermion. In Fig. 4.6(b) the local density of states $|\phi_{n,L}|^2$ and $|\phi_{n,R}|^2$ are plotted by black lines. They are in good agreement with the numerical data-points. Because the wavefunctions are not completely localized, the corresponding energy is not exactly zero but determined by the finite overlap

$$\epsilon = \phi_L^* H \phi_R \approx \frac{\mu}{2\beta N} e^{-\beta(N-1)} + \frac{\Delta_p + t}{2\beta N} e^{-\beta N}. \tag{4.25}$$

This analytical result is shown in Fig. 4.6(c) (red curve) together with the numerical result (blue dots) as a function of chain-length N. We find that the wavefunction overlap and accordingly the energy ϵ is exponentially suppressed with increasing length of the chain.

To summarize, by investigating the bulk properties of the one-dimensional p-wave superconductor we determined the two distinct topological phases (trivial for $|\mu| > 2t$ and non-trivial for $|\mu| < 2t$). Moreover we considered two special cases, (I) a conventional insulator and (II) Kitaev's limit with Majorana modes localized to single sites at the end of the lattice [see Fig. 4.5]. Away from this special limit the Majorana excitations have wavefunctions which extend into the bulk region. Furthermore the corresponding energy is finite but exponentially suppressed.

4.2.2. Realizations of 1-D topological superconductors

There exist plenty of proposals on how to engineer platforms that behave as p-wave superconductors. The fundamental reason is the rareness of bulk p-wave superconductors in nature. For instance, Sr_2RuO_4 appears to be a chiral p-wave superconductor. Even if p-wave superconductivity would be confirmed in the strontium-ruthenates it would be still difficult to engineer topological quantum computing devices, as these are strongly correlated materials.

There has been great effort in developing hybrid devices with low energy excitations behave effectively like those of a p-wave superconductor. Implementations that have been proposed in the past few years commonly rely on helical electronic states that arise from some type of spin-momentum locking and are brought in proximity to a conventional s-wave superconductor. It is easy to imagine that spin-momentum coupling induces p-wave pairing apart from the s-wave pairing amplitude. One can distinguish between hybrid systems of topological insulators and conventional superconductors, but also heterostructures involving Rashba spin-orbit [83] coupled semiconductors. The latter proposals stimulated a series of experiments which presented first encouraging signatures of Majorana-fermions. Other proposals rely on a superconductor in proximity to helical magnetism.

Semiconducting nanowires

First we will discuss a hybrid structure that has been widely discussed in the literature. It consists of a semiconducting wire with intrinsic Rashba spin-orbit coupling [83] which is

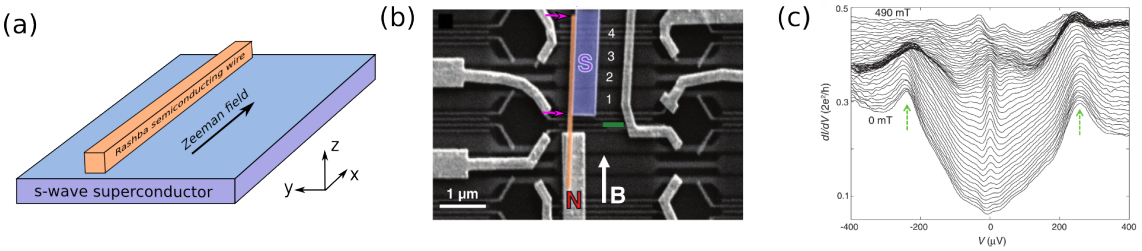

Figure 4.7.: Rashba spin-orbit coupled semiconducting wire in proximity to a bulk s-wave superconductor. (a) The combination of spin-orbit coupling, superconductivity and magnetic field renders a topologically non-trivial superconductor. (b) Figure from Mourik *et al.* [12]: For illustrative reasons we added additional colors and arrows. The semiconducting wire (indium antimonide) is indicated in orange. It is placed next a niobium titanium nitride superconductor (blue). In the presence of a strong magnetic field B the Majorana edge modes should appear at the boundaries of the topological superconductor indicated by magenta arrows. A normal metallic gold electrode probes the local density of states via a tunneling barrier (green line). (c) Figure from Ref [12]: The respective dI/dV curves for increasing magnetic field from bottom to top. A zero-bias peak appears, indicating a Majorana edge-mode.

positioned in proximity to a conventional s-wave superconductor (see Fig. 4.7). Due to the proximity effect there will be a finite pairing amplitude $\tilde{\Delta}$ induced in the wire. It turns out that the application of a magnetic field B along the wire pushes this hybrid system into a topologically non-trivial phase which harbors Majorana bound states at each end of the wire. We describe this situation in terms of the Hamiltonian ($\hbar = 1$)

$$H(k) = \xi_k \tau_z + \alpha k \sigma_z - g\mu_B B \tau_z \sigma_x - \tilde{\Delta} \tau_y \sigma_y. \tag{4.26}$$

Here $\xi_k = k^2/2m - \mu$ is the electronic dispersion of the wire, $\tilde{\Delta}$ is the proximity induced gap, α is the spin-orbit coupling, g and μ_B are the gyromagnetic factor and the Bohr-magneton respectively and B is the magnetic field applied in x-direction. We will now illustrate the connection to the p-wave superconductor. As shown in Ref. [78] the proximity induced gap as well as the spin-orbit coupling can be viewed as a perturbation $\mathcal{V} = \alpha k \sigma_z + \tilde{\Delta} \tau_y \sigma_y$, such that $H(k) = H_0(k) + \mathcal{V}$. Following Schrieffer and Wolff [84] we look for a unitary transformation $\tilde{H} = \mathcal{U} H \mathcal{U}^\dagger$ with $\mathcal{U} = \exp(i\mathcal{S})$, such that terms linear in $\mathcal{V}$ are eliminated. This is true if we find an operator $\mathcal{S}$ which satisfies $[\mathcal{S}, H_0] = i\mathcal{V}$ leading to [78]

$$\tilde{H}(k) \approx H_0(k) + \frac{i}{2}[\mathcal{S}, \mathcal{V}] = \tilde{\xi}_k \, \tau_z - g\mu_B \tilde{B} \tau_z \sigma_x - \Delta_y \tau_x - \Delta_z \tau_x \sigma_x \tag{4.27}$$

with the renormalized quantities $\tilde{\xi}_k = \left[1 + \frac{\tilde{\Delta}^2}{2\xi_k^2}\right]\xi_k$, $\tilde{B} = \left[1 + \frac{\alpha^2 k^2}{2g^2\mu_B^2 B^2}\right] B$ and the spin-triplet pairing components $\Delta_y = (\tilde{\Delta}\alpha/2\xi_k)\, k$ and $\Delta_z = (\tilde{\Delta}\alpha/2g\mu_B B)\, k$. The magnetic field polarizes the spins along the x-direction. Making it sufficiently strong will spin-polarize the low energy excitations such that just one spin-component σ is important and the Hamiltonian reads

$$H_\sigma(k) = [\tilde{\xi}_k - g\mu_B \tilde{B} \sigma] \tau_z - 2[\Delta_y + \Delta_z \sigma]\, k\, \tau_x, \tag{4.28}$$

After an additional rotation around the τ_z-axis it takes the form of the p-wave superconductor (4.15). The eigenenergies are given by

$$E_\sigma(k) = \pm \sqrt{[\tilde{\xi}_k - g\mu_B \tilde{B} \sigma]^2 + 4[\Delta_y + \Delta_z \sigma]^2 k^2} \tag{4.29}$$

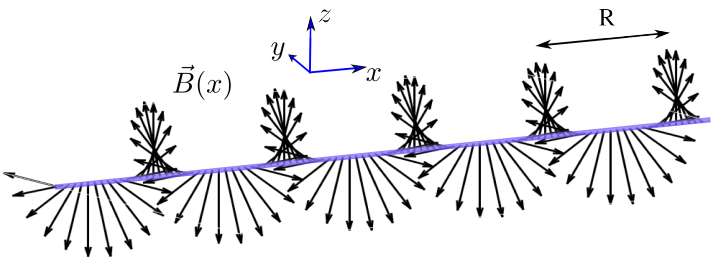

Figure 4.8.: Helical magnetic profile $\vec{B}(x)$ along a one-dimensional wire. The magnetic profile generates an effective spin-orbit coupling in the rotated frame (see Eq. (4.31)).

The gap closing at $k = 0$ appears for the spin-down band provided that $g\mu_B B = \mu + \tilde{\Delta}^2/2\mu$. From the discussion in section 4.2.1 we directly find that the topological non-trivial phase occurs for $g\mu_B B > \mu + \tilde{\Delta}^2/2\mu$. We observe that the spin-orbit coupling α does not enter the criterion for the topological phase transition. However, it determines the localization of the Majorana wavefunction. Consequently, materials with strong spin-orbit are needed.

In Fig. 4.7(b) and (c) results from the pioneering experiment of Mourik *et al.* [12] are presented. The setup consists of a indium antimonide nanowire with strong spin-orbit coupling ($\alpha \approx 0.2\,\mathrm{eV}$) and a large g-factor ($g \approx 50$). The proximity to the superconductor niobium titanium nitride induced gap of $\tilde{\Delta} \approx 250\,\mu\mathrm{eV}$. The dI/dV-spectra clearly show the appearance of a zero-bias peak with increasing magnetic field which the authors attribute to a Majorana fermion. However, there also exist explanations for zero-bias peaks in semiconducting devices other than Majorana physics. As such the interplay between superconductivity and Kondo-physics in semiconducting dots has been discussed [85].

Helical magnetic order

Next, we discuss Majorana proposals that consider an inhomogeneous magnetic order that is either intrinsically coexisting with superconductivity [86] or could be realized by placing nanomagnets [87] or magnetic atoms [88, 89, 90, 91, 92, 93, 94, 95] on the surface of a conventional superconductor. In all these proposals the inhomogeneous magnetic order generates an effective spin-orbit coupling which can be even larger than the intrinsic spin-orbit coupling of semiconducting nanowires. In order to see the correspondence between inhomogeneous magnetic field and spin-orbit coupling we take a look at Fig. 4.8 which shows the helical magnetic profile $\vec{B}(x) = B[0, \sin(x/R), \cos(x/R)]$. In the presence of superconductivity the Hamiltonian for a one-dimensional wire reads

$$H(x) = \left[-\frac{1}{2m}\partial_x^2 - \mu\right]\tau_z - g\mu_B B\big[\sin(x/R)\sigma_y + \cos(x/R)\tau_z\sigma_z\big] - \Delta\tau_y\sigma_y \qquad (4.30)$$

It has been shown in Ref. [87] that the unitary transformation $\mathcal{U} = \exp\big(-i\frac{x}{2R}\,\tau_z\sigma_x\big)$ yields the Hamiltonian

$$\mathcal{U}H\mathcal{U}^\dagger = \left[\frac{p_x^2}{2m} - \mu + \frac{1}{8mR^2}\right]\tau_z + \frac{1}{2mR}p_x\sigma_x - g\mu_B B\tau_z\sigma_z - \Delta\tau_y\sigma_y \qquad (4.31)$$

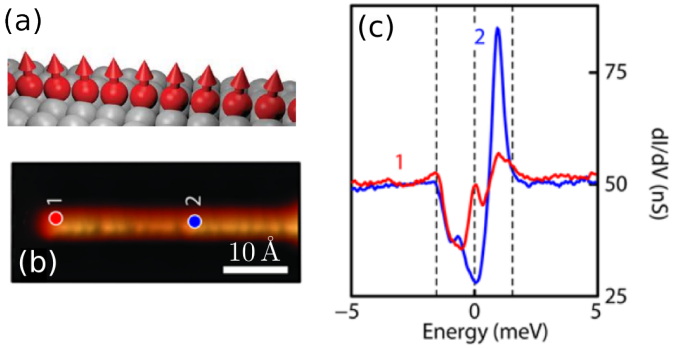

Figure 4.9.: (a) One-dimensional chain of Fe on a Pb surface. The Fes' magnetic moments align ferromagnetically. (b) STM image of the Fe chain. (c) Local dI/dV curves at two specific points, 1. at the end of the chain and 2. in the bulk. (Figures from Ref. [13] with slight modifications)

with the momentum operator $p_x = -i\partial_x$. We find that Eq. 4.31 assumes the form of the Rashba spin-orbit coupled wire (4.26) with spin-orbit coupling-strength $\alpha = 1/2mR$. The unitary transformation shows the correspondence between spin-orbit coupling and helical magnetic order. It has been stressed that magnetic atoms on a superconducting surface with spin-orbit coupling order in a spiral fashion. The fundamental reason leading to this phenomenon is an inversion anisotropy in the substrate like spin-orbit coupling which leads to an anisotropic RKKY superexchange and tilts the relative orientation of magnetic moments [90, 91, 96]. We will discuss this aspect in more detail in section 5.2.1.

Very recently Majorana signatures have been observed in self-assembled one-dimensional chains of Fe-atoms deposited on a Pb-surface (see Fig. 4.9(a)). The combination of a ferromagnetic orientation of Fes' magnetic moments, Rashba spin-orbit coupling induced by the hybridization of the Fe d-orbitals and the Pb p-orbitals, and proximity induced superconductivity leads to the emergence of zero energy states. The experimental data on the local density of states is presented in Fig. 4.9 and shows (b) a scanning tunneling microscope (STM) image of the Fe-chain and (c) the local density of states at two specific points indicated in (b). Right at the end of the chain the data shows a zero bias peak which is absent in the bulk. Therefore the spatially resolved signature provides great evidence for a Majorana bound state.

4.2.3. Topological quantum-computing

From a fundamental point of view the realization of Majorana fermions in solid state devices is already an exciting endeavor. They may be also used for quantum computation processing. For further reading we refer to Refs. [78, 97, 98, 99]. Let us consider the situation depicted in Fig. 4.5(II). In this case we may define a strongly delocalized fermion $d = (\gamma_1 + i\bar{\gamma}_N)/2$. The occupation of the state defines the parity of the degenerate ground states $|0\rangle$ and $|1\rangle = d^\dagger |0\rangle$. With the parity operator

$$P = 1 - 2d^\dagger d = -i\gamma_1\bar{\gamma}_N \tag{4.32}$$

we observe that $P|0\rangle = |0\rangle$ and $P|1\rangle = -|1\rangle$. This means that the pair of Majorana fermions forms a *topological* qubit with elementary states $|0\rangle$ and $|1\rangle$. Because the two elementary states differ by quasiparticle parity, a coherent superposition is not possible.

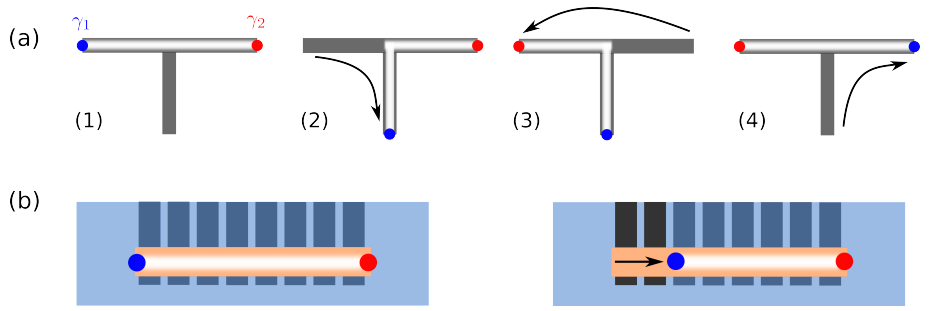

Figure 4.10.: (a) Braiding operation: Exchange of two Majorana fermions by a T-shaped junction. The topological phase is represented by the white shaded area. (b) Top view of the semiconductor setup shown in Fig. 4.7(a). Changing the gate potential moves the topological phase-boundary and the respective position of the Majorana fermion.

However, if one can combine four Majorana fermions, γ_1, ..., γ_4, to form a *logical* qubit. This qubit operates in the subspace of odd or even parity, e.g. for the latter the two states were defined as $|\bar{0}\rangle = |00\rangle$ and $|\bar{1}\rangle = |11\rangle$. In this computational basis the three Pauli matrices may be expressed by the four Majorana operators

$$\sigma_x = -i\gamma_2\gamma_3, \qquad \sigma_y = i\gamma_1\gamma_3, \qquad \sigma_z = -i\gamma_1\gamma_2. \tag{4.33}$$

Braiding operations

The interesting property of the Majorana qubit is the fact that the exchange of Majorana fermions is non-Abelian. In one-dimensional systems Majorana fermions can be exchanged by considering T-junctions consisting of two perpendicular wires. Within the four-step protocol depicted in Fig. 4.10(a) it is possible to exchange Majorana fermions even without closing the gap of the topological non-trivial region (shown by the white shaded area). How to move a Majorana from one point to another depends on the setup. In semiconductor devices for instance an appropriate gating changes the chemical potential μ locally and moves the phase-boundary and the Majorana fermion with it. In the following we will partly follow the discussion of Alicea *et al.*[97].

Let us assume that the exchange happens adiabatically. Up to a phase φ, which can be associated with the superconducting phase of the horizontal wire, we can express the Majorana fermions via fermionic operators (see section 4.2.1), i.e.

$$\begin{aligned} \gamma_1 &= e^{i\varphi/2} d_{hL}^\dagger + H.c., \\ \gamma_2 &= e^{i(\varphi-\pi)/2} d_{hR}^\dagger + H.c., \end{aligned} \tag{4.34}$$

where d_{hL} / d_{hL} denotes the most left / right fermion operator on the horizontal wire. This corresponds to the initial situation (1) shown in Fig. 4.10(a) at the initial time t_1. Then adiabatically moving γ_1 to the bottom end of the vertical wire does not influence the second Majorana, i.e. $\gamma_2(t_2) = \gamma_2(t_1)$, but the first Majorana is given by

$$\gamma_1(t_2) = s_1 \left[e^{i\tilde{\varphi}/2} d_{vB}^\dagger + H.c. \right], \tag{4.35}$$

where d_{vB} is the fermion operator at the bottom end of the vertical wire and $\tilde{\varphi}$ is the superconducting phase associated with the second wire. During the adiabatic evolution

the Majorana has acquired a phase-factor s_1. A gauge transformation $\varphi \to \varphi - \Lambda$ in (4.34) shows that the only possible choice is $\Lambda = 0, \pi$, giving $s_1 = \pm 1$. Then at the time-instant t_3 the second Majorana has changed ends at the horizontal wire, and is now given by

$$\gamma_2(t_3) = s_2 \gamma_1(t_1), \tag{4.36}$$

up to a sign s_2. In step (4) the Majorana γ_1 is moved upwards to the right end of the horizontal wire, giving

$$\gamma_1(t_4) = s_1' s_1 \gamma_2(t_1) \qquad \text{and} \qquad \gamma_2(t_4) = s_2 \gamma_1(t_1). \tag{4.37}$$

Now the braiding should not change the quasiparticle parity $P = -i\gamma_1(t_1)\gamma_2(t_1)$ giving the constrain $s_1 s_1' s_2 = -1$. Without loss of generality we choose $s_2 = -1$ such that (4.37) defines the braiding operation

$$\begin{aligned} \gamma_1 &\to \gamma_2, \\ \gamma_2 &\to -\gamma_1. \end{aligned} \tag{4.38}$$

The unitary operator which fulfills the relation $\gamma_i \to \mathcal{U}_{12}\, \gamma_i\, \mathcal{U}_{12}^\dagger$ is given by

$$\mathcal{U}_{12} = \frac{1}{\sqrt{2}}(1 + \gamma_1\gamma_2) = \exp\left(i\frac{\pi}{4}\sigma_z\right) \tag{4.39}$$

which corresponds to a $\pi/2$-rotation of the logical qubit $\{|00\rangle, |11\rangle\}$ around the z-axis. Similarly one can define braiding operations which mix the two logical states, i.e.

$$\mathcal{U}_{23}\,|00\rangle = \frac{1}{\sqrt{2}}(1 + \gamma_2\gamma_3)\,|00\rangle = \frac{1}{\sqrt{2}}(|00\rangle + i\,|11\rangle). \tag{4.40}$$

We observe that the two operations $\mathcal{U}_{12}$ and $\mathcal{U}_{23}$ do not commute with each other. We rather obtain $[\mathcal{U}_{12}, \mathcal{U}_{23}] = \gamma_1\gamma_3 = -i\sigma_y$, which constitutes the non-Abelian nature of braiding operations. Braiding of Majorana fermions is a topologically protected operation, meaning that it is inert against environmental decoherence. However, concerning single qubit operations the braiding operation exclusively generates $\pi/2$ rotations in the Hilbert space which is not sufficient if it comes to universal quantum computing. One way to circumvent this issue is the abolishment of the topological protection or the coupling of the Majorana qubit to other solid state qubits.

Topological protection

The Majorana qubit is said to be *topologically protected*, meaning that bit-flip or phase-shift errors due to environmental coupling can not occur unless it leads to a coupling of the Majorana fermions. In fact, the Majorana qubit is inert against any *local* perturbation. Nonetheless there are still sources of decoherence which are difficult to avoid. First of all, if Majorana wavefunctions have a finite overlap this leads to a level-splitting (4.25) corresponding to the coupling of the two Majorana states,

$$H = -i\epsilon\gamma_1\gamma_2 = \epsilon\sigma_z. \tag{4.41}$$

Nonetheless this coupling is exponentially suppressed allowing for a compensation of this error by appropriately adapting the setup, e.g. increasing the system size or changing the parameters (like gate potential μ in the semiconductor proposals) accordingly.

Furthermore metallic structures of low dimensions and small size have a large Coulomb interaction. If the superconductor is isolated from its electromagnetic environment, the charging energy $e^2/2C$ gives rise to a *non-local* Coulomb coupling

$$H = -i\frac{e^2}{2C}\gamma_1\gamma_2 = \frac{e^2}{2C}\sigma_z. \tag{4.42}$$

This means that even without an overlap of the Majorana wavefunctions there can be an interaction among them. In any case Eqs. (4.41) and (4.42) give an idea how to lift the topological protection. This is useful if one wants to perform topological *unprotected* quantum computing. Another decoherence source is the quasiparticle-poisoning of the superconductor. In the case of the Majorana qubit it is of particular interest because quasiparticles may change the parity subspace of the qubit and thus destroy its topological protection [100]. Furthermore, non-adiabatic manipulations of Majorana qubits, that might be necessary for quantum information processing, lead to decoherence as well [101].

5. Majorana fermions in chains of magnetic adatoms

In the previous sections we mentioned several alternatives to engineer a one-dimensional p-wave superconductor. In these realizations the main ingredient needed to induce spin-triplet pairing was some kind of spin-momentum locking. The latter either originates intrinsically or due to helical magnetic fields. There exists a broad discussion in the literature about establishing helical magnets in proximity to a superconductor either, by using nanomagnets [87] or magnetic adatoms that are deposited in a spiral fashion [88, 89, 90, 91, 92, 93, 94, 95].

Indeed recent experiments with scanning tunneling microscopes (STM) have demonstrated that magnetic adatoms can be positioned in chains with either spiral [102] or collinear (ferro- or antiferromagnetic) orientation of spins [14]. Even more recently STM experiments on atomic Fe chains on Pb provided the first evidence for Majorana edge states in adatom chains [13].

Following the discussion of section 4.2.2, it is evident that a collinear magnetic order in combination with spin orbit coupling or a helical magnetic order may lead to zero energy Majorana edge states. However, it is not straightforward to see how a spin-momentum locking can be induced if the orientation of magnetic adatoms is collinear and if the substrate itself does not exhibit spin-orbit coupling. In section 5.1 we will present an alternative setup which relies on the combined application of a magnetic field and a supercurrent. In the presence of an antiferromagnetic background of atomic moments, these fields create an effective locking between spin and current, analogous to spin-orbit coupling. Following Kitaev's decomposition in section 4.2.1 we find that this system indeed constitutes a topological superconductor which harbors Majorana zero energy states with distinct wavefunctions and spin-textures.

In section 5.2 we consider collinear chains on a substrate that itself has a Rashba-type of spin-orbit coupling. We discuss under which circumstances the collinear orientation of spins may be realized, albeit the substrate's spin-orbit coupling favors a spiral magnetic order. We will see that the crystal field of the substrate may select an easy axis along which the spins tend to align. Of course, this competes with the anisotropic exchange mentioned before and we will investigate this competition. Later in this section we distinguish the

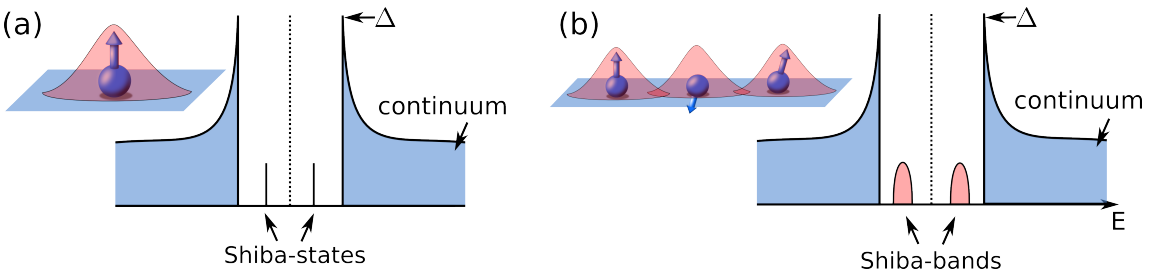

Figure 5.1.: Magnetic adatoms on a superconducting substrate: (a) A single magnetic adatom leads to intra-gap *Shiba states*. (b) In the case of many atoms the associated wavefunctions overlap and form *Shiba bands*.

different topological phases, amongst which there will be phases which appear to have multiple Majorana fermions.

Before we start with the main discussion, let us shortly recapitulate the effect of magnetic atoms in a superconducting host. A single magnetic atom on a superconducting surface leads to quasiparticle state which lies energetically within the superconducting gap and is particle-hole symmetric, a so called Shiba state (see Fig. 5.1(a)). The bound state wavefunction assumes the form [32]

$$\phi(r) \sim \frac{\sin(k_F r)}{k_F r} e^{-r/\xi}, \tag{5.1}$$

where ξ is the coherence length of the superconductor and k_F is the Fermi-momentum. The wavefunction is localized around the magnetic atom and has the energy

$$\epsilon = \pm\Delta \frac{1-(\pi\nu_F JS)^2}{1+(\pi\nu_F JS)^2}, \tag{5.2}$$

where ν_F is the density of states of the superconductor in the normal phase and J is the magnetic exchange between the atomic spin S and the spin of the conduction electrons (see Eq. (1.30)). In the case of many magnetic atoms the subgap-excitations form bands. This becomes clear from the picture in Fig. 5.1(b). The bound state wavefunctions, localized at different adatom sites, overlap and hybridize, leading to a band-structure in the limit of long chains. In the following sections we will investigate the topological properties of exactly these *Shiba-bands*.

5.1. Topological Shiba states in antiferromagnetic chains with applied external fields

Recently it was demonstrated that single magnetic atoms [42] or small atomic clusters [41] deposited on a metallic surface tend to align their spin S along an axis which is selected by the underlying crystal field of the metallic substrate [see Fig. 5.2(a)]. The two degenerate ground states of these systems are the $m = \pm S$ states. The lifetime of these states reaches the order of seconds for iron-clusters [41] and up to minutes for a single holmium atom on top of a platinum surface [42]. Now imagine putting several of these spins in a row. In Ref. [14] it was experimentally demonstrated that in this case the RKKY (Rudermann-Kittel-Kasuya-Yosida) superexchange interaction stabilizes

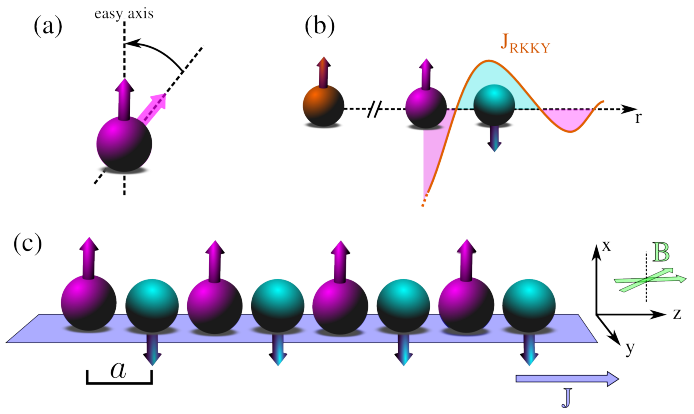

Figure 5.2.: (a) The substrate crystal field selects an easy axis along which the atoms' magnetic moments tend to align. (b) The antiferromagnetic order is stabilized by the RKKY-interaction. (c) Antiferromagnetic chain on top of a superconductor. The simultaneous application of a supercurrent J and a Zeeman-field B turns the preexisting topological unprotected Shiba bands topologically non-trivial.

either a ferromagnetic of antiferromagnetic order of spins, depending on the spacing between them.

Starting from the experimental observation, we raise the question whether we can establish a topological superconductor from an antiferromagnetic profile of magnetic atoms *without* involving spin-orbit coupling in the substrate [see Fig. 5.2(c)]. In section 5.1.1 we introduce the model which is based on a chain of classical spins arranged in antiferromagnetic fashion on top of a conventional superconductor. We start with a mapping of our model to Kitaev's chain model in the limit of short superconducting coherence length. Later, in section 5.1.3, we investigate the more general case and try to make a connection to actual experimental parameters.

5.1.1. Model

We consider a superconductor with classical magnetic moments located at positions $\boldsymbol{R}_i$ $(i = 1, ..., N)$. The corresponding Hamiltonian is given by

$$H = H_{\mathrm{sc}} + H_{\mathrm{J}}. \tag{5.3}$$

Here the first term describes the superconducting substrate, i.e.

$$H_{\mathrm{sc}} = \frac{1}{2}\sum_{\boldsymbol{k}} \psi^{\dagger}_{\boldsymbol{k}}[\xi_{\boldsymbol{k}}\tau_z - \Delta\tau_y\sigma_y]\psi_{\boldsymbol{k}}. \tag{5.4}$$

The spinor $\psi^{\dagger}_{\boldsymbol{k}} = (c^{\dagger}_{\boldsymbol{k}\uparrow}, c^{\dagger}_{\boldsymbol{k}\downarrow}, c_{-\boldsymbol{k}\uparrow}, c_{-\boldsymbol{k}\downarrow})$ contains the operators $c^{\dagger}_{\boldsymbol{k}\sigma}$ which creates an electron in the state with momentum $\boldsymbol{k}$ and spin σ and the energy $\xi_{\boldsymbol{k}} = |\boldsymbol{k}|^2/2m - \mu$ $(\hbar = 1)$. Furthermore Δ is the excitation gap of the bulk superconductor. The second term,

$$H_{\mathrm{J}} = \frac{J}{2}\sum_{n=1}^{N}\sum_{\boldsymbol{k}\boldsymbol{k}'} e^{-i(\boldsymbol{k}-\boldsymbol{k}')\cdot\boldsymbol{R}_n}\, \psi^{\dagger}_{\boldsymbol{k}}[\boldsymbol{S}_n \cdot \tilde{\boldsymbol{\sigma}}]\psi_{\boldsymbol{k}'}, \tag{5.5}$$

describes the exchange interaction between conduction electrons and atomic spins $\boldsymbol{S}_n$. Here we introduced the spin-operator $\tilde{\boldsymbol{\sigma}} = (\tau_z\sigma_x, \sigma_y, \tau_z\sigma_z)$. Stimulated by the experiments [14] we assume an antiferromagnetic order oriented along an easy axis which is

chosen along the x-direction [see Fig. 5.2(c)], i.e. $\boldsymbol{S}_n = (-1)^n S\,\hat{x}$. Thus, we neglect the quantum-mechanical nature of the spins and consider them as a classical magnetic background. This is justified as we show later in section 5.2.1, where we analyze the stability of the antiferromagnetic order against quantum-fluctuations and find that it can be stabilized by the crystal field anisotropy. Evenmore the magnetic order is robust also against collective flips which have been observed experimentally [103].

In order to obtain the energy spectrum of H we solve the Bogolioubov de Gennes equation [32]

$$\sum_{\boldsymbol{k}'}\left[\delta_{\boldsymbol{k},\boldsymbol{k}'} - \hat{G}_{\boldsymbol{k}}(\varepsilon) J \sum_i e^{-i(\boldsymbol{k}-\boldsymbol{k}')\cdot\boldsymbol{R}_n}[\boldsymbol{S}_n\cdot\tilde{\boldsymbol{\sigma}}]\right]\phi_{\boldsymbol{k}'} = 0\,. \tag{5.6}$$

Here the spinor $\phi_{\boldsymbol{k}} = (u_{\boldsymbol{k}\uparrow}, u_{\boldsymbol{k}\downarrow}, v_{\boldsymbol{k}\uparrow}, v_{\boldsymbol{k}\downarrow})^{\mathrm{T}}$ contains the particle and hole components u and v. Furthermore $\hat{G}_{\boldsymbol{k}}(\varepsilon) = (\varepsilon - H_S)^{-1}$ is the Gor'kov-Nambu Green's function. The two external fields, magnetic field and supercurrent, are depicted in Fig. 5.2(c) and enter via the substitution $\xi_{\boldsymbol{k}} \to \xi_{\boldsymbol{k}-\boldsymbol{J}/2\tau_z} + \mu_B B\sigma_z$. Mind that the supercurrent, $\boldsymbol{J}$, is in units of momentum. The associated velocity of Cooper pairs is given by $v_s = |\boldsymbol{J}|/2m$ corresponding to a current of $I_s = en_s v_s$. Here n_s is the density of the superconducting condensate.

Generally the magnetic field and the supercurrent are not independent. However, considering the limit of a thin superconducting film and an in-plane applied magnetic field the coupling to the orbital degrees of freedom is suppressed over the Zeeman coupling (Pauli-limit). If both fields are small, i.e. $\mu_B B \ll \Delta$ and $|\boldsymbol{J}| \ll 1/\xi \ll k_F$, we are able to linearize the Green's-function $G_{\boldsymbol{k}}(\varepsilon)$, yielding

$$\hat{G}_{\boldsymbol{k}}(\varepsilon) = \frac{1}{\varepsilon^2 - \xi_{\boldsymbol{k}}^2 - \Delta^2}\left[\varepsilon - \Delta\tau_y\sigma_y - \mu_B B\tau_z\sigma_z + \frac{1}{2m}\boldsymbol{k}_F\cdot\boldsymbol{J}\right]. \tag{5.7}$$

Solving Eq. (5.6) together with (5.7) turns out to be complicated if one takes into account the modification of the superconducting order parameter in the bulk superconductor. More precisely, this would require a self-consistent and spatially resolved treatment of Δ. In fact, for a single impurity it has been shown in Ref. [34] that the superconducting gap, although slightly suppressed close to the impurity site, remains finite even close to the quantum-phase-transition $\pi\nu_F JS = 1$. Neglecting the self-consistent treatment of the superconducting gap due to the above reasoning is a widely used approximation which provides qualitatively good results [93, 94, 104]. Furthermore it provides the technical advantage to trace out the continuum degrees of freedom reducing the system to a one-dimensional model of Shiba states.

Starting from the Green's function (5.7) we can retrieve the Fourier components $\hat{G}_n(\varepsilon) = \sum_{\boldsymbol{k}} e^{i\boldsymbol{k}\cdot\boldsymbol{R}_n}\hat{G}_{\boldsymbol{k}}(\varepsilon)$. For a metal it is well validated to perform a quasiclassical expansion $\xi_{\boldsymbol{k}}/v_F \ll k_F$ (here v_F is the Fermi-velocity) and thus linearize the dispersion around the Fermi-surface. By that the sum over momenta can be expressed in terms of the integral

$$\hat{G}_n(\varepsilon) = \nu_F\int_{-1}^{1}\frac{d\cos(\theta)}{2}\int_{-\infty}^{\infty} d\xi_{\boldsymbol{k}}\, e^{ik_F a\, n\cos(\theta)} e^{i\xi_{\boldsymbol{k}} a\, n\cos(\theta)/v_F}\hat{G}_{\boldsymbol{k}}(\varepsilon). \tag{5.8}$$

Here ν_F is the density of states in the normal state, $\cos(\theta) = \frac{\boldsymbol{k}\cdot\boldsymbol{R}_n}{|\boldsymbol{k}||\boldsymbol{R}_n|}$ and $\boldsymbol{R}_n = \hat{z}\, an$. The atomic displacement is given by a. Furthermore $n = 1, ..., N$ denotes the position of the atom. For $n = 0$ the integral can be readily calculated, recovering the result of Eq. (1.28), i.e.

$$\hat{G}_0(\varepsilon) = -\pi\nu_F \frac{\varepsilon - \Delta\tau_y\sigma_y - \mu_B B\tau_z\sigma_z}{\sqrt{\Delta^2 - \varepsilon^2}}. \tag{5.9}$$

For $n \neq 0$ we obtain [105]

$$\hat{G}_n(\varepsilon) \approx -\pi\nu_F \left[\frac{\varepsilon - \Delta\tau_y\sigma_y - \mu_B B\tau_z\sigma_z}{\sqrt{\Delta^2 - \varepsilon^2}} a_n + \tau_z b_n + \frac{|\boldsymbol{J}|k_F}{2m} \frac{c_n}{\sqrt{\Delta^2 - \varepsilon^2}} \right], \tag{5.10}$$

with the combinations

$$\begin{aligned} a_n &= e^{-\frac{a|n|}{\xi}} \frac{\sin(k_F a|n|)}{k_F a|n|}\,, \\ b_n &= e^{-\frac{a|n|}{\xi}} \frac{\cos(k_F a|n|)}{k_F a|n|}\,, \\ c_n &= i\mathrm{sgn}(n)\, e^{-\frac{a|n|}{\xi}} \frac{\sin(k_F a|n|) - k_F a|n|\, \cos(k_F a|n|)}{(k_F an)^2}\,, \end{aligned} \tag{5.11}$$

where ξ is the coherence length of the superconductor. At this point, Eq. (5.6) reduces to the one-dimensional BdG equation

$$\sum_{n=1}^{N} [\delta_{nl} - G_{n-l}(\varepsilon)]\phi_l = 0\,, \tag{5.12}$$

with $\phi_l = \sum_{\boldsymbol{k}} e^{i\boldsymbol{k}\cdot\boldsymbol{R}_l}\phi_{\boldsymbol{k}}$. In the following sections we will derive the low-energy Shiba states from this equation. More precisely we consider Shiba states which lie deep inside the gap, i.e. $\varepsilon \ll \Delta$. This limit allows to linearize the BdG equation in ε/Δ yielding the generalized eigenvalue problem

$$\begin{aligned} &\sum_{l=1}^{N} \left[\frac{\delta_{nl}(-1)^n\Delta}{\pi\nu_F JS}\tau_z\sigma_z - a_{n-l}(\Delta\tau_y\sigma_y - \mu_B B\tau_z\sigma_z) + b_{n-l}\Delta\tau_z + c_{n-l}\frac{|\boldsymbol{J}|k_F}{2m} \right] \phi_l \\ &= \varepsilon \sum_{l=1}^{N} a_{n-l}\phi_l. \end{aligned} \tag{5.13}$$

Eq. (5.13) can be solved numerically. In section 5.1.3 we will do this for realistic material parameters. Before that let us consider the limit of short superconducting coherence length $\xi \ll a$. Although this may be an unrealistic case for a conventional metallic superconductor, this limit offers great inside into the topological properties of the system.

5.1.2. Short coherence length – mapping to Kitaev's chain model

In the limit of short coherence length the coefficients a_n, b_n and c_n are exponentially suppressed on the length-scale of coherence length ξ. Accordingly couplings to higher than nearest neighbors may be neglected, yielding the BdG-equation

$$[-(-1)^n M\tau_z\sigma_x - \Delta\tau_y\sigma_y + \mu_B B\tau_z\sigma_z]\,\Phi_n + [t\tau_z + it_J]\,\Phi_{n+1} + [t\tau_z - it_J]\,\Phi_{n-1} = \varepsilon\Phi_n, \tag{5.14}$$

with $M = -\Delta/\pi\nu_F JS$, $t = b_1\Delta$ and $t_J = ic_1|\boldsymbol{J}|k_F/2m$. Furthermore $\Phi_n = \sum_l \mathcal{L}_{nl}\phi_l$ with the Cholesky decomposition $a_{n-l} = [(\mathcal{L}\mathcal{L}^\dagger)^{-1}]_{nl}$ [1]. The simplified BdG equation (5.14) describes an on-site magnetic exchange energy M which is alternating in sign, on-site superconductivity Δ and nearest neighbor hopping with strength t. Furthermore the time-reversal breaking fields $\boldsymbol{B}$ and $\boldsymbol{J}$ add as a on-site term and as a nearest neighbor hopping amplitude t_J respectively.

Infinite chain and topological classification

The one-dimensional system (5.14) can be topologically classified if we consider the bulk properties of an infinitely long chain. To this end we go to momentum space where the corresponding Hamiltonian is given by $H_k = H_k^0 + V_k$. We distinguish between the unperturbed Hamiltonian

$$H_k^0 = -M\tau_z\rho_x\sigma_x - \Delta\tau_y\sigma_y + 2t\sin(ka)\tau_z\rho_z \tag{5.15}$$

and the perturbation by the external fields $\boldsymbol{B}$ and $\boldsymbol{J}$,

$$V_k = -2t_J\cos(ka)\rho_z + \mu_B B\tau_z\sigma_z. \tag{5.16}$$

The additional Pauli matrices ρ_i account for the antiferromagnetic order and act on the extended spinor

$$\Phi_k = (u_{k+Q/2,\uparrow}, u_{k+Q/2,\downarrow}, u_{k-Q/2,\uparrow}, u_{k-Q/2,\downarrow}, v_{k+Q/2,\uparrow}, v_{k+Q/2,\downarrow}, v_{k-Q/2,\uparrow}, v_{k-Q/2,\downarrow})^{\mathrm{T}}. \tag{5.17}$$

The relative shift in momenta by the wave-vector $Q = \pi/a$ reflects the underlying antiferromagnetic order. The momenta k are restricted to the reduced Brillouin zone (RBZ) $k \in (-\pi/2a,\, \pi/2a]$.

First, we consider the topologically unprotected Shiba-spectrum in the limit of vanishing control-fields, i.e. $V_k = 0$. We start with the Hamiltonian (5.15) and apply the unitary transformation

$$U = \exp\left(i\frac{\pi}{4}\tau_z\sigma_z\right)\exp\left(i\frac{\pi}{4}\tau_y\rho_y\right)\exp\left(i\frac{\pi}{4}\sigma_x(1+\tau_z)\right). \tag{5.18}$$

The Hamiltonian that we obtain is block-diagonal, i.e. $U^\dagger H_k^0 U = \sum_{\sigma\rho}(1+\sigma\sigma_z)(1+\rho\rho_z)H^0_{\rho\sigma}(k)/4$ and contains the blocks

$$H^0_{\rho\sigma}(k) = \hat{\boldsymbol{g}}_{\rho\sigma}(k)\cdot\boldsymbol{\tau}. \tag{5.19}$$

Here the g-vector is given by $\hat{\boldsymbol{g}}_{\rho\sigma}(k) = [0, (\rho M - \Delta)\sigma, 2t\rho\sin(ka)]$. The corresponding Shiba energy-dispersions are

$$E_{\rho\sigma}(k) = \pm\sqrt{(\rho M - \Delta)^2 + 4t^2\sin^2(ka)}. \tag{5.20}$$

For $\rho = 1$ and $M = \Delta$ the bands show a gap closing at $k = 0$. This gap closing might be associated with a topological phase-transition. To check whether this is the case we

[1] The Cholesky decomposition of a tridiagonal matrix $\mathcal{A}_{nl} = a_{n-l} = \delta_{nl} + a_1\delta_{n,l+1} + a_1\delta_{n,l-1}$ with $a_1 \ll 1$ is given by $\mathcal{A} \approx (\mathbb{1} + \Lambda^a/2)(\mathbb{1} + \Lambda^a/2)$ with $\Lambda^a_{nl} = a_1\delta_{n,l+1} + a_1\delta_{n,l-1}$. According to that $\mathcal{L} = \mathbb{1} - \Lambda^a/2$. With $\mathcal{N} = (-1)^n\delta_{nl}$, $\Lambda^b_{nl} = b_1\delta_{n,l+1} + b_1\delta_{n,l-1}$ and $\Lambda^c_{nl} = c_1\delta_{n,l+1} - c_1\delta_{n,l-1}$ we obtain in linear order of a_1, b_1 and c_1: $\mathcal{L}^\dagger\mathcal{N}\mathcal{L} \approx \mathcal{N}$, $\mathcal{L}^\dagger\Lambda^b\mathcal{L} \approx \Lambda^b$ and $\mathcal{L}^\dagger\Lambda^c\mathcal{L} \approx \Lambda^c$.

have to see that Eq. (5.19) is very similar to Eq. (4.17). Like in section 4.2.1 we can assign each block Hamiltonian $H_{\rho\sigma}$ to the symmetry class BDI which has the topological invariant [see (4.14)]

$$\mathcal{N}_{\rho\sigma} = \frac{1}{2\pi}\int_{\mathrm{BZ}} dk \left[\hat{\boldsymbol{g}}_{\rho\sigma}(k) \times \frac{\partial \hat{\boldsymbol{g}}_{\rho\sigma}(k)}{\partial k}\right]_x . \tag{5.21}$$

It follows immediately that the invariant (5.21) is zero. Therefore we are in the non-trivial topological phase. Next, we will show that the situation is different when we switch on the control-fields $\boldsymbol{B}$ and $\boldsymbol{J}$ which enter as a perturbation V_k. In the spirit of a Schrieffer-Wolff transformation $\tilde{H}_k = e^{i\mathcal{S}_k} H_k e^{-i\mathcal{S}_k} \approx H_k^0 + i[\mathcal{S}_k, V_k]/2$ we find an operator

$$\mathcal{S}_k = -\frac{t_J \cos(ka)}{M}\tau_z\rho_y\sigma_x + \frac{\mu_B B}{2M}\rho_x\sigma_y + \frac{t\, t_J \sin(2ka)}{M\Delta}\tau_y\rho_x\sigma_z - \frac{\mu_B B\, t \sin(ka)}{M\Delta}\tau_x\rho_y \tag{5.22}$$

which necessarily fulfills the condition $[\mathcal{S}_k, H_k^0] = iV_k$. Since only changes close to the inversion symmetric point $k = 0$ change the topological properties, we consider k to be small. Because of this we may neglect the last two terms in Eq. (5.22) because they are smaller by one order in the expansion parameters $\{t_J,\, \mu_B B\}/\{\Delta,\, M\}$ and k. Up to second order in t_J, $\mu_B B$ as well as k, the low-energy Hamiltonian is given by

$$\tilde{H}_k = -\Delta\tau_y\sigma_y - \widetilde{M}\tau_z\rho_x\sigma_x + 2t\sin(ka)\tau_z\rho_z - \Lambda\,\cos(ka)\rho_y\sigma_y\,. \tag{5.23}$$

The combinations $\widetilde{M}$ and Λ both depend on the external fields,

$$\widetilde{M} = \left[M + \frac{[\mu_B B]^2 + 4t_J^2\cos^2(ka)}{2M}\right] \qquad \text{and} \qquad \Lambda = \frac{2\mu_B B t_J}{M}. \tag{5.24}$$

The Hamiltonian (5.23) assumes a time-reversal symmetry $\Theta = i\rho_y\sigma_y\mathcal{K}'$, i.e. $[\Theta, \tilde{H}_k] = 0$. Here $\mathcal{K}'$ defines the complex conjugation, which however does not affect the sign of the antiferromagnetic wavevector Q. Together with the charge-conjugation symmetry $\Xi = \tau_x\rho_x\mathcal{K}'$, i.e. $\{\Xi, \tilde{H}_k\} = 0$, the Hamiltonian also has a chiral symmetry $\Pi = \Theta\Xi = \tau_x\rho_z\sigma_y$. Furthermore there exist two unitary symmetries $\mathcal{U}_1 = \tau_y\rho_y$ and $\mathcal{U}_2 = \tau_z\rho_z\sigma_x$, i.e. $[\mathcal{U}_i, \tilde{H}_k] = 0$, with which we can define additional *generalized* time-reversal, charge-conjugation and chiral symmetries, i.e. $\Theta' = \mathcal{U}\Theta$, $\Xi_i = \mathcal{U}_i\Xi$, and $\Pi_i = \mathcal{U}_i\Pi$. Table 5.1 summarizes the different symmetries. According to that the Hamiltonian falls into the topological class $\oplus_{n=1}^{4}$BDI [106].

Θ	Ξ	Π	Θ^2	Ξ^2	Π^2
$i\rho_y\sigma_y\mathcal{K}'$	$\tau_x\rho_x\mathcal{K}'$	$\tau_x\rho_z\sigma_y$	1	1	1
$i\tau_y\rho_y\mathcal{K}'$	$-i\tau_z\rho_y\sigma_x\mathcal{K}'$	$\tau_z\rho_x\sigma_y$	1	1	1
$i\tau_z\rho_x\sigma_y\mathcal{K}'$	$i\tau_y\rho_z\mathcal{K}'$	$-\tau_y\sigma_z$	1	1	1

Table 5.1.: Symmetry classification of (5.23). $\mathcal{K}'$ defines the complex conjugation, which does not act on the antiferromagnetic wavevector Q.

The additional symmetries allow for a block-diagonalizing the Hamiltonian by the unitary transformation (5.18). As before $U^\dagger H_k U = \sum_{\sigma\rho}(1+\sigma\sigma_z)(1+\rho\rho_z)\hat{\boldsymbol{g}}_{\rho\sigma}(k)\cdot\boldsymbol{\tau}/4$ with

$$\hat{\boldsymbol{g}}_{\rho\sigma}(k) = [0, (\rho\widetilde{M} - \Delta)\sigma + \Lambda\cos(ka), 2t\rho\sin(ka)]. \tag{5.25}$$

We immediately see that this vector has a finite winding $\mathcal{N}_{\rho\sigma}$ [(5.21)] and therefore indicates a transition into the topologically non-trivial phase for

$$|\Lambda| > |\widetilde{M} \mp \Delta|. \tag{5.26}$$

There are some similarities and differences to the nanowire-proposals presented in section 4.2.2. In both cases a time-reversal breaking magnetic field is applied. In the case of the nanowire the Zeeman-field has to be rather large in order to exceed the proximity induced gap. However, in our case the superconducting gap is compensated by the intrinsic magnetic order and there is no requirement for large external fields. Furthermore the combined presence of Zeeman-field and supercurrent leads to a staggered spin-current coupling proportional to Λ (see Eq. (5.23)), similar to the spin-orbit coupling in semiconducting nanowires. It is staggered because it is off-diagonal in ρ-space leading to an alternating dependence in real space.

Kitaev's limit – well localized Majorana states

Due to the bulk-boundary correspondence we expect that the topological properties become manifest in the case of the finite size chain. From section 4.2.1 we know that there is a convenient way to illustrate that the zero energy edge state in the topological non-trivial phase is composed of two well separated Majorana edge states. Now we extend the decomposition of lattice electrons into Majorana fermions to the *spinful* case. By expressing the Hamiltonian (5.23) by electronic field operators $\Psi_n^\dagger = (\psi_{n\uparrow}^\dagger, \psi_{n\downarrow}^\dagger, \psi_{n\uparrow}, \psi_{n\downarrow})$ on the lattice sites $n = 1...N$, we obtain

$$\tilde{H} = \frac{1}{2}\sum_{n=1}^{N} \Psi_n^\dagger[-(-1)^n\widetilde{M}\tau_z\sigma_x - \Delta\tau_y\sigma_y]\Psi_n + \frac{1}{2}\sum_{n=1}^{N-1} \Psi_n^\dagger[2t\tau_z - (-1)^n\Lambda\sigma_y]\Psi_{n+1}. \tag{5.27}$$

As a next step we introduce the Majorana operators $\gamma_{n\sigma} \equiv \psi_{n\sigma} + \psi_{n\sigma}^\dagger$ and $\bar{\gamma}_{n\sigma} \equiv (\psi_{n\sigma} - \psi_{n\sigma}^\dagger)/i$. For explanatory reasons we write the full matrix expressions

$$\begin{aligned}\tilde{H} = \frac{i}{4}\sum_{n=1}^{N} \begin{pmatrix}\gamma_{n\uparrow}\\ \gamma_{n\downarrow}\\ \bar{\gamma}_{n\uparrow}\\ \bar{\gamma}_{n\downarrow}\end{pmatrix}^{\mathrm{T}} \begin{pmatrix} 0 & 0 & 0 & \Delta + (-1)^n\widetilde{M} \\ 0 & 0 & -\Delta + (-1)^n\widetilde{M} & 0 \\ 0 & \Delta - (-1)^n\widetilde{M} & 0 & 0 \\ -\Delta - (-1)^n\widetilde{M} & 0 & 0 & 0 \end{pmatrix} \begin{pmatrix}\gamma_{n\uparrow}\\ \gamma_{n\downarrow}\\ \bar{\gamma}_{n\uparrow}\\ \bar{\gamma}_{n\downarrow}\end{pmatrix} \\ + \frac{i}{4}\sum_{n=1}^{N-1} \begin{pmatrix}\gamma_{n\uparrow}\\ \gamma_{n\downarrow}\\ \bar{\gamma}_{n\uparrow}\\ \bar{\gamma}_{n\downarrow}\end{pmatrix}^{\mathrm{T}} \begin{pmatrix} 0 & -(-1)^n\Lambda & 2t & 0 \\ (-1)^n\Lambda & 0 & 0 & 2t \\ -2t & 0 & 0 & -(-1)^n\Lambda \\ 0 & -2t & (-1)^n\Lambda & 0 \end{pmatrix} \begin{pmatrix}\gamma_{n+1\uparrow}\\ \gamma_{n+1\downarrow}\\ \bar{\gamma}_{n+1\uparrow}\\ \bar{\gamma}_{n+1\downarrow}\end{pmatrix}.\end{aligned} \tag{5.28}$$

In Fig. 5.3(a) we illustrate that each lattice site decomposes into four Majorana fermions. For simplicity we consider a chain consisting of three lattice-sites. Remember the course of action we took in section 4.2.1:

- First we decoupled the Majorana operators locally by choosing the chemical potential to be zero. In the case at hand we make the appropriate choice $\widetilde{M} = \Delta$ which cancels out several terms in the off-diagonal of (5.28) but does not decouple all of the Majorana fermions locally. Specifically, $\gamma_{n\uparrow}$ and $\bar{\gamma}_{n\downarrow}$ are decoupled if n is odd and $\gamma_{n\downarrow}$ and $\bar{\gamma}_{n\uparrow}$ if n is even (see Fig. 5.3).

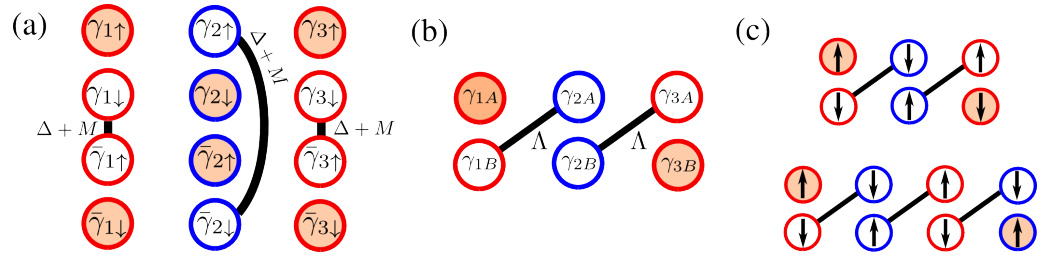

Figure 5.3.: Kitaev's decomposition [see Eq. (5.28)]: (a) Each lattice electron decomposes into four Majorana operators. For $\Delta = \widetilde{M}$ and $n = \text{odd}$ the Majorana operators $\gamma_{n\uparrow}$ and $\bar{\gamma}_{n\downarrow}$ remain locally un-paired, whereas for even sites $\gamma_{n\downarrow}$ and $\bar{\gamma}_{n\uparrow}$ are un-paired. (b) We reduce to the low-energy subspace of locally un-paired Majorana operators and introduce new operators $\gamma_{n,A}$ and $\gamma_{n,B}$ (see text). In this basis, for $2t = \Lambda$, the Kitaev-limit is achieved: The Majorana operators γ_{1A} and γ_{3B} are true zero energy states and appear at the ends of the chain. (c) Electronic spin-polarization of the Majorana edge modes. The rightmost Majorana bound state is eigenstate of σ_y, either with eigenvalue $+1$ or -1 depending on the parity of number of sites, N.

- It turns out that within this low energy subspace spanned by the Majorana operators $\{\gamma_{\text{odd},\uparrow}, \bar{\gamma}_{\text{odd},\downarrow}, \gamma_{\text{even},\downarrow}, \bar{\gamma}_{\text{even},\uparrow}\}$ the nearest neighbor coupling is given by

$$\begin{aligned}\tilde{H}_{\text{sub}} = &\frac{i}{4}\sum_m \begin{pmatrix}\gamma_{2m-1\uparrow}\\ \bar{\gamma}_{2m-1\downarrow}\end{pmatrix}^T \begin{pmatrix}-\Lambda & -t\\ t & \Lambda\end{pmatrix}\begin{pmatrix}\gamma_{2m\downarrow}\\ \bar{\gamma}_{2m\uparrow}\end{pmatrix}\\ &+\frac{i}{4}\sum_m \begin{pmatrix}\gamma_{2m\downarrow}\\ \bar{\gamma}_{2m\uparrow}\end{pmatrix}^T \begin{pmatrix}-\Lambda & -t\\ t & \Lambda\end{pmatrix}\begin{pmatrix}\gamma_{2m+1\uparrow}\\ \bar{\gamma}_{2m+1\downarrow}\end{pmatrix}.\end{aligned} \tag{5.29}$$

  For the specific choice, $\Lambda = 2t$, we find the familiar form

$$\tilde{H}_{\text{sub}} = -\frac{i}{2}\Lambda\sum_{n=1}^{N-1}\gamma_{n,B}\gamma_{n+1,A}, \tag{5.30}$$

  Eq. (5.30) looks very similar to the Kitaev limit (4.21) that we inferred for a *spinless* p-wave superconductor. However, here the Majorana operators are combinations of spin-up and spin-down operators, i.e.

$$\begin{aligned}\gamma_{2m-1,A} &= \left(\gamma_{2m-1,\uparrow} + \bar{\gamma}_{2m-1,\downarrow}\right)/\sqrt{2},\\ \gamma_{2m-1,B} &= \left(\gamma_{2m-1,\uparrow} - \bar{\gamma}_{2m-1,\downarrow}\right)/\sqrt{2},\\ \gamma_{2m,A} &= \left(\gamma_{2m,\downarrow} + \bar{\gamma}_{2m,\uparrow}\right)/\sqrt{2},\\ \gamma_{2m,B} &= \left(\gamma_{2m,\downarrow} - \bar{\gamma}_{2m,\uparrow}\right)/\sqrt{2}.\end{aligned} \tag{5.31}$$

  The Majorana operators γ_{1A} and γ_{NB} do not appear in the Hamiltonian (5.30), thus they must have zero energy.

It turns out that the electronic part of the Majorana wavefunctions are eigenstates of the

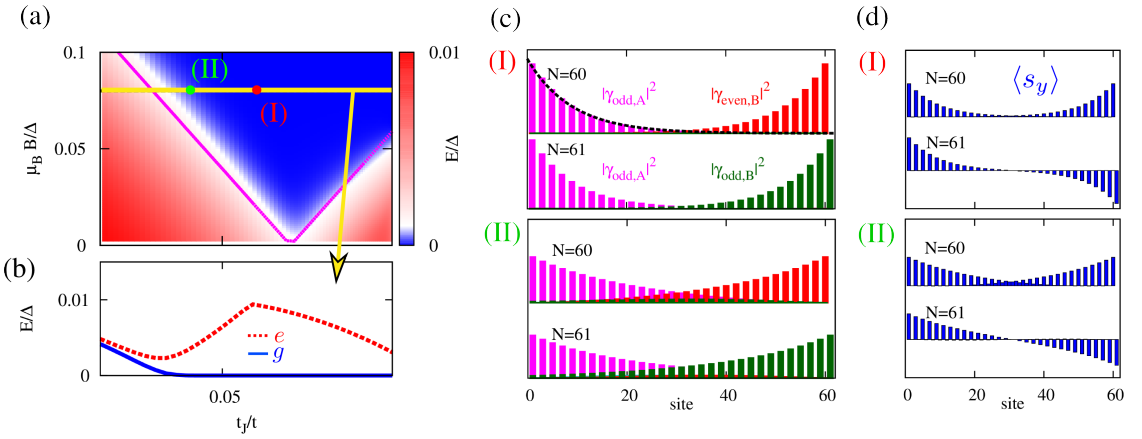

Figure 5.4.: (a) Topological phase-diagram: The ground state wavefunction of a finite chain ($N = 160$) is plotted in color scale as a function of current t_J and magnetic field B. The analytical result for the topological phase-transition (5.26) is shown by the magenta line. (b) Cut along the yellow line in (a): The two lowest positive eigenenergies are plotted as a function of t_J. (c) Wavefunctions corresponding to the red (I) and green (II) point in (a) for an even ($N = 60$) and odd ($N = 61$) number of sites. (d) The s_y spin-polarization corresponding to the wavefunctions shown in panel (c). [parameters used in this figure: $M = 0.99\Delta$ and $t = 0.1\Delta$]

s_y spin-operator. For instance

$$\gamma_{\mathrm{odd},A} = \frac{\gamma_{\mathrm{odd},\uparrow} + \bar{\gamma}_{\mathrm{odd},\downarrow}}{\sqrt{2}} = \frac{(\psi_{\mathrm{odd},\uparrow} - i\psi_{\mathrm{odd},\downarrow}) + (\psi^\dagger_{\mathrm{odd},\uparrow} + i\psi^\dagger_{\mathrm{odd},\downarrow})}{\sqrt{2}} = \psi_{\mathrm{odd},\rightarrow} + \psi^\dagger_{\mathrm{odd},\rightarrow}. \tag{5.32}$$

Here the fermion operator $\psi^\dagger_{\mathrm{odd},\rightleftarrows} = (\psi_{\mathrm{odd},\uparrow} - i\psi_{\mathrm{odd},\downarrow})/\sqrt{2}$ creates an electron which is spin-polarized along the y-direction. We find that the electronic part of $\gamma_{\mathrm{odd},A}$ and $\gamma_{\mathrm{even},B}$ is an eigenvector to σ_y with eigenvalue $+1$, whereas $\gamma_{\mathrm{even},A}$ and $\gamma_{\mathrm{odd},B}$ have the eigenvalue -1. This is an important observation, as it tells that the spin-polarization of the rightmost Majorana $\gamma_{N,B}$ is different for the cases that N is even or odd (see Fig. 5.3(c)). This characteristic feature could serve as an spectroscopic signature and help identifying the emergence of Majorana excitations.

Bulk-boundary correspondence

In the previous paragraphs we identified the topological phase-transition which appears for $|\Lambda| > |\Delta - \widetilde{M}|$ and Δ, $\widetilde{M} > 0$. Furthermore we analyzed the Kitaev limit, $\widetilde{M} = \Delta$ and $2t = \Lambda$ for which we found that the Majorana fermions are spin-polarized and that the polarization differs depending on whether they appear at even or odd sites. In order to confirm these results we perform a numerical solution of the BdG equation (5.14). In the top-panel of Fig. 5.4(a) we show the ground state energy of a chain with $N = 160$ atoms as a function of current t_J and magnetic field B. The previously extracted condition for the topological phase transition (5.26), which is equivalent to

$$\mu_B B = \left| \sqrt{2M|\Delta - M|} - 2t_J \right|, \tag{5.33}$$

follows the magenta line. First of all we observe that this condition coincides with the emergence of a zero energy ground state. Within the blue-colored region the system is in the non-trivial topological phase. The yellow cut shows the evolution of the ground state (g) and the first excited state (e) as a function of supercurrent t_J: The ground state energy goes to zero whereas the first excited energy opens a gap. This excitation gap leads to a protection of the Majorana wavefunction, because the exponential suppression of the wavefunctions increases with the *bulk*-excitation gap [compare situations (I) and (II) in Fig. 5.4(b)]. There are two interesting features the wavefunctions seem to obey:

(i) The electronic components of the Majorana wavefunctions constitute eigenstates of σ_y [see Fig. 5.4(c)]. Adding a single site switches the spin-polarization of the right Majorana fermions similar to Kitaev's limit discussed previously. In order to understand this behavior we follow section 4.2.1 and derive an analytical approximation for the envelope of the wavefunction. To this end we solve the equation $\tau_y(\hat{\boldsymbol{g}}_{\rho\sigma}\cdot\boldsymbol{\tau})\Phi_{k\rho\sigma}=0$ with $\hat{\boldsymbol{g}}_{\rho\sigma}$ from Eq. (5.25) close to point $k=0$, i.e.

$$\left\{(\rho\widetilde{M}-\Delta)\sigma+\Lambda+i2t\rho\,ka\,\tau_x\right\}\Phi_{k\rho\sigma}=0. \tag{5.34}$$

The real-space solutions are given by

$$\Phi_{n\rho\sigma}=\exp(ikn)\Phi_{k\rho\sigma}=\frac{1}{\sqrt{\beta_{\rho\sigma}}}e^{\mp\beta_{\rho\sigma}n}\left|\pm\right\rangle_{\tau_x} \tag{5.35}$$

with the inverse decay-length $\beta_{\rho\sigma}=[(\rho\widetilde{M}-\Delta)\sigma+\Lambda]/2t\rho$. Furthermore, $|\pm\rangle_{\tau_x}$ are eigenfunctions of τ_x. For $\rho=\sigma=1$ the envelope of (5.35) closely follows the numerical result in Fig. 5.4(b) (black dashed line). The Majorana wavefunctions $\Phi_{k\rho\sigma}$ are eigenfunctions of the chiral operator $\Pi'=\tau_x\rho_z\sigma_z$. In the unrotated frame this operator is given by $\Pi=U\Pi'U^\dagger=\tau_x\rho_z\sigma_y$ (see Table 5.1). According to this the spin-components are eigenfunctions of σ_y. This is the result of the Kitaev limit as well as of the numerical diagonalization in Fig. 5.4(c).

(ii) A second observation is that the wavefunctions are constrained to be zero at every second site. This implies that adding a single site also switches the occupation of even sites to odd sites and vise versa. Comparing the BdG equation (5.14) with its momentum representation (5.15) one immediately sees that the operator ρ_z corresponds to the translational operator $t_a\psi_n=\psi_{n+1}$. The corresponding eigenstates have the property $t_a\psi_n=\lambda\psi_n$ with $\lambda=\pm1$. Thus the eigenfunctions are either constant or alternating, i.e. $\psi_n^\pm=(\pm1)^n$. Furthermore, we found that the Hamiltonian (5.15) has another chiral symmetry $\Pi_1=\tau_z\rho_x\sigma_y$ (see Table. 5.1). Here the Pauli-matrix ρ_x reflect the alternating antiferromagnetic order. The corresponding eigenstates fulfill the relation $(-1)^n\psi_n^\pm=\lambda_\pm\psi_n^\pm$ with $\lambda_\pm=\pm1$. According to that the wavefunctions must vanish at every second site as observed in Fig. 5.4(b).

5.1.3. Long coherence length

The limit of short coherence length offered an transparent way for a qualitative analysis of the underlying mechanism turning the formerly unprotected Shiba bands topologically non-trivial. Now we consider the realistic case of coherence lengths, ξ, which are larger than the spacing of adatoms in STM experiments [14]. Typical coherence length are listed in Table 5.2. Hence, an accurate description should include higher neighbor couplings rather than just nearest neighbor coupling in the generalized eigenvalue problem (5.13).

	Δ [meV]	E_F [eV]	λ_F [nm]	ξ [nm]
Pb	1.33	9.47	0.79	83
Al	0.18-0.21	11.7	0.71	1600
Nb	1.55	5.32	1.06	38

Table 5.2.: Parameters for superconducting gap Δ, Fermi-energy E_F, Fermi-wavelength λ_F and coherence length ξ adopted from Ref. [107, 108, 109].

Topological $\mathbb{Z}_2$-invariant

First we consider the limit of an infinitely long chain. In momentum space the BdG equation (5.13) becomes diagonal, i.e.

$$\left[-M\tau_z\rho_x\sigma_x - \hat{\alpha}_k(\Delta\tau_y\sigma_y - \mu_B B\tau_z\sigma_z) + \hat{\beta}_k\Delta\tau_z + \hat{\gamma}_k\frac{|\boldsymbol{J}|k_F}{2m}\right]\phi_k = \varepsilon_k\hat{\alpha}_k\,\phi_k. \quad (5.36)$$

The operators $\hat{\alpha}_k$, $\hat{\beta}_k$ and $\hat{\gamma}_k$ are given by

$$\begin{aligned}\hat{\alpha}_k &= \sum_n e^{-ikan}(i\rho_z)^n\, a_n = \alpha_k^e - \alpha_k^o\,\rho_z\\ \hat{\beta}_k &= \sum_n e^{-ikan}(i\rho_z)^n\, b_n = \beta_k^e - \beta_k^o\,\rho_z,\\ \hat{\gamma}_k &= -i\sum_n e^{-ikan}(i\rho_z)^n\, c_n = \gamma_k^e - \gamma_k^o\,\rho_z.\end{aligned} \quad (5.37)$$

A Cholesky decomposition of the right-hand site of Eq. 5.36, i.e. $\hat{\alpha}_k = (\mathcal{L}_k\mathcal{L}_k^\dagger)^{-1}$ together with the transformation $\Phi_k = \mathcal{L}_k\phi_k$ leads to the effective Schrödinger-equation $H_k\Phi_k = \varepsilon_k\Phi_k$ with the Hamiltonian

$$H_k = -m_k\,\tau_z\rho_x\sigma_x - \Delta\,\tau_y\sigma_y + t_k\,\tau_z\rho_z + \mu_k\,\tau_z + \mu_B B\,\tau_z\sigma_z + j_k\,\rho_z + p_k. \quad (5.38)$$

The respective coefficients are give by

$$\begin{aligned}m_k &= \frac{M}{\sqrt{D_k}}, \qquad \frac{t_k}{\Delta} = -\frac{\alpha_k^e\beta_k^o - \alpha_k^o\beta_k^e}{D_k}, \qquad \frac{j_k}{\Delta} = -\frac{\alpha_k^e\gamma_k^o - \alpha_k^o\gamma_k^e}{D_k},\\ \frac{\mu_k}{\Delta} &= -\frac{\alpha_k^e\beta_k^e - \alpha_k^o\beta_k^o}{D_k}, \qquad \frac{p_k}{\Delta} = -\frac{\alpha_k^e\gamma_k^e - \alpha_k^o\gamma_k^o}{D_k}.\end{aligned} \quad (5.39)$$

with $D_k = (\alpha_k^e)^2 - (\alpha_k^o)^2$. By comparing the Hamiltonian (5.38) with the nearest neighbor approximation (5.15) one identifies the antiferromagnetic exchange energy m_k, the kinetic energy t_k as well as the supercurrent contribution j_k. The additional terms μ_k and p_k correspond to even-neighbor kinetic energy and supercurrent contributions respectively.

The full Hamiltonian falls into the topological class D since it is only particle-hole symmetric, i.e. $\{H_k, \Xi\} = 0$ with the charge-conjugation operator $\Xi = \tau_x\rho_x\mathcal{K}'$ and $\mathcal{K}'$ defined in Table. 5.1. According to Ref. [80] the topological invariant of a class D topological superconductor in one dimension is a $\mathbb{Z}_2$ invariant. Following Kitaev [110] this invariant can be expressed in terms of the Pfaffian, i.e.

$$\mathcal{M} = \mathrm{sgn}\left[\mathrm{Pf}(H_{k=0})\,\mathrm{Pf}(H_{k=Q/2})\right]. \quad (5.40)$$

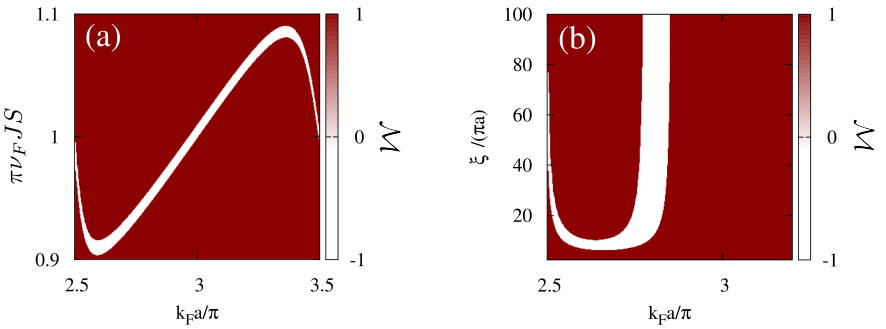

Figure 5.5.: Topological $\mathbb{Z}_2$-invariant: Dependence on atomic spacing a as well as (a) magnetic exchange energy J ($\xi/a = 20\,\pi$) and (b) coherence length ξ ($\pi\nu_F JS = 0.99$). [parameters used in this figure: $\mu_B B = 0.05\Delta$ and $k_F|\boldsymbol{J}|/2m = 0.5\,\Delta$]

Note however that the Pfaffian is evaluated at $k = \pi/2a$ instead of $k = \pi/a$, as we have to consider the reduced Brillouin zone. It turns out that in our case the Pfaffian only changes sign at $k = 0$. This is not surprising since this is the point where the gap closing occurs in the case of the nearest-neighbor approximation. After some algebra we find

$$\mathcal{M} = \mathrm{sgn}\left[\mathrm{Pf}(H_{k=0})\right] = \mathrm{sgn}\left[(A - j_{k=0})^2 - (\mu_B B)^2\right] , \tag{5.41}$$

where $A^2 = \Delta^2 - m_{k=0}^2 + \mu_{k=0}^2$. Therefore the topological phase-transition happens at $\mu_B B = |A - j_{k=0}|$, which is equivalent to the condition (5.33) that we derived for the limit of short coherence length. If the magnetic exchange energy $m_{k=0}$ is large enough in order to compensate the superconducting gap, then the external fields can be small. For simulations we used a magnetic field $B = 0.05\,\Delta/\mu_B$ and a supercurrent-velocity $v_s = |\boldsymbol{J}|/2m = 0.5\Delta/k_F$. In Fig. 5.5 the dependence of the topological invariant $\mathcal{M}$ on (a) magnetic exchange energy J and (b) coherence length ξ is shown. The sign-change of the invariant indicates a topological phase-transition. Depending on the atomic spacing a, the invariant $\mathcal{M}$ opens a window, in which the system is topologically non-trivial (white area). It can be broadened by increasing the current or the magnetic field.

Bulk-boundary correspondence

Following the bulk-boundary correspondence we may expect a Majorana fermion to appear in the topological non-trivial phase which is defined by a negative sign of $\mathcal{M}$. In Fig. 5.6 the topological invariant as well as the two lowest positive energies of the finite chain are shown. We find that the predicted topological phase-transition coincides with the emergence of a zero-energy bound state.

In Fig. 5.7 the Majorana wavefunctions $\gamma_{n,A}$ and $\gamma_{n,B}$ as defined in the previous section as well as their spin-polarizations are plotted. Interestingly we observe the same features as in the short coherence length limit, i.e. (i) the wavefunctions vanish on either even or odd sites. By adding a single atom the whole spectral weight of the Majorana $\gamma_{n,B}$ shifts by one lattice site. (ii) The same is true for the spin-polarization, which depends on the parity of the number of atoms in the chain. In the previous section we attributed these features to the presence of particular chiral symmetries. Strictly speaking the Hamiltonian (5.38) does not have these symmetries. However, since the external fields $\boldsymbol{B}$ and $\boldsymbol{J}$ are so small this symmetry remains approximately intact and these interesting spectroscopic

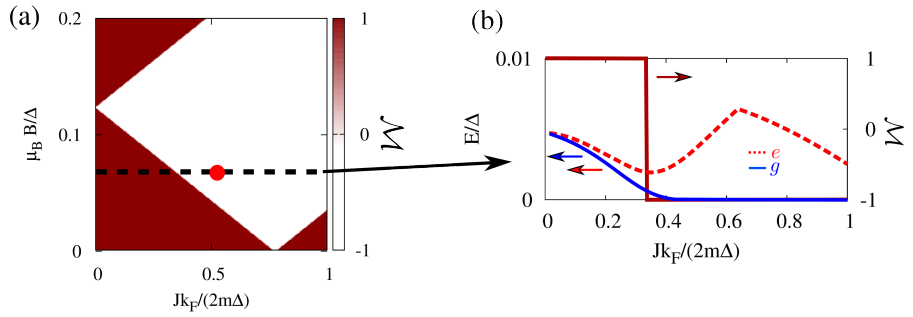

Figure 5.6.: (a) Topological invariant $\mathcal{M}$ depending on current $|\boldsymbol{J}|$ and magnetic field B. (b) Two lowest positive energies, ground state (g) and first excited (e), as well as the topological invariant $\mathcal{M}$ along the cut in panel (a). The topological phase transition coincides with the appearance of a zero energy state.

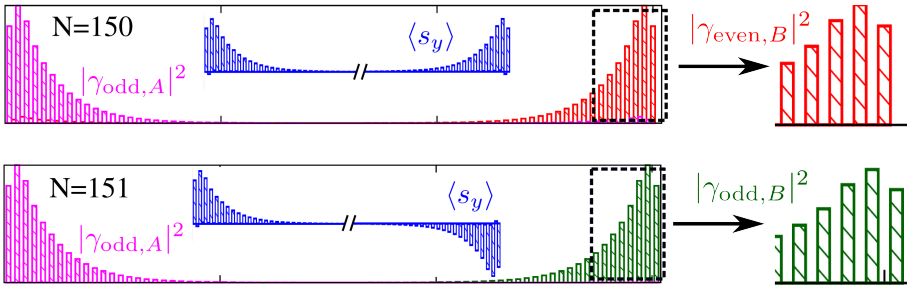

Figure 5.7.: Majorana wavefunctions as well as the corresponding spin-polarization $\langle s_y \rangle$ for $N = 150$ and $N = 151$ atoms. External fields correspond to the red point indicated in Fig. 5.6(a).

signatures still survive. The Majorana wavefunctions are exponentially suppressed within the bulk, in contrast to the power-law behavior observed in helical Shiba chains [94]. This can be seen in Fig. 5.8(a) and (b), where we investigate the dependence of the two lowest positive energies. With increasing the length of the chain the ground state energy is lowered. In Fig. 5.8(c) the corresponding wavefunctions for $N = 50$ and $N = 150$ atoms are presented. Their comparison shows that the spectral weight of each end-state is extended over roughly 20 atom-sites.

Experimental realizability

In order to increase the window of the topological non-trivial phase and make it experimentally accessible, both the coherence length and the superconducting gap should be small so to increase the maximum current and decrease the necessary magnetic field.

Let us consider the superconductor Pb in order to evaluate the experimental realizability. Pb has a critical magnetic field of $B_c^{\perp} \sim 0.1\,\mathrm{T}$, when applied perpendicular to the plane. On the other hand magnetic fields applied parallel to the surface can be even larger. In Ref. [111] in-plane magnetic fields of the order of $B_c^{\parallel} \sim 10\,\mathrm{T}$ have been achieved. In our simulation we used $B = 0.05\,\Delta/\mu_B$, which corresponds to a planar field of the order of $\sim 1\,\mathrm{T}$.

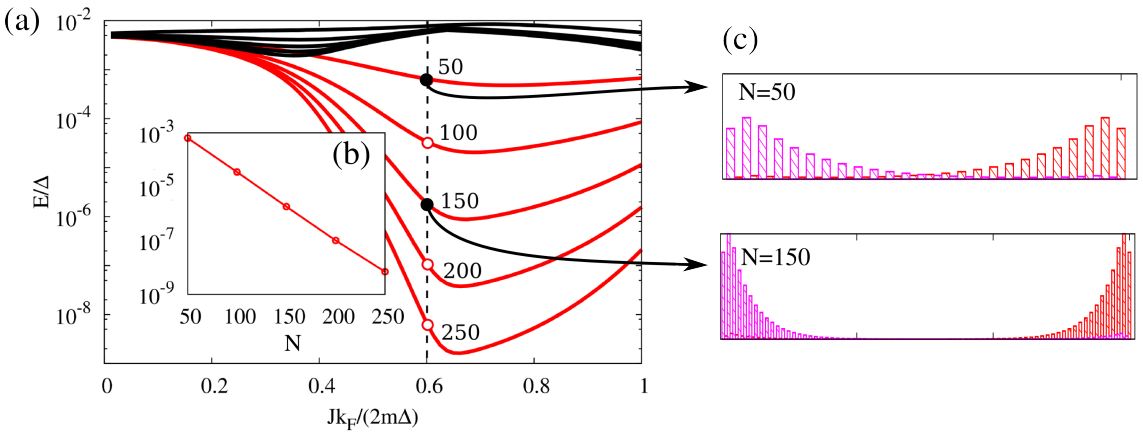

Figure 5.8.: (a) Two lowest positive eigenenergies (ground state in red and first excited state in black) for different chain-lengths N depending on supercurrent $|\boldsymbol{J}|$. (b) Ground-state energy depending on N for the particular points indicated in panel (a). (c) Wavefunctions for $N = 50$ and $N = 150$ atom sites. [additional parameters used in this figure: $\mu_B B = 0.05\Delta$ and $\pi\nu_F JS = 0.99$.]

Regarding the supercurrent we used a velocity of $v_s = |\boldsymbol{J}|/2m = 0.5\,\Delta/k_F$. It corresponds to a current $I = en_s v_s$ which shall be compared to the Ginsburg-Landau result for the maximum critical current $I_d \sim 2en_s/3\sqrt{3}m\xi$. This means that the maximum critical momentum has to be compared to the coherence length of the superconductor, i.e. $J_c \approx 1/\xi$. According to that we used a current corresponding to $J \sim 0.1\,J_c$ in our simulations. In thin Pb structures currents of the order of ten percent of the depairing current have been achieved in the lab [112]. Even larger currents, close to the depairing current, have been observed in other materials like Nb [113] which has a smaller coherence length.

Furthermore with regard to Fig. 5.5 the window of topologically non-trivial phase corresponds to an atomic displacement of $\delta a \sim 0.1\,\pi k_F^{-1}$. This requires an accuracy of Å in atomic deposition, which is certainly possible [14]. Regarding the length of atomic chains we found that the Majorana wavefunctions are extended over a few tens of atomic sites [see Fig. 5.8(c)]. Up to date the realization of ferromagnetic and antiferromagnetic chains only of about ten atoms has been communicated [14] but longer chains are certainly accessible [103]. Recent experiments have shown that even longer chains with self-assembled ferromagnetic order can be produced [13].

In conclusion the setup appears to be experimentally accessible, albeit technically very challenging. Parameters like adatom spacing, supercurrent and magnetic field can be used to control the topological phase transition. Furthermore state-of-the-art scanning tunneling techniques would allow for the detection of the parity dependent switching of the local density of states as well as the spin-texture which shall be associated with the Majorana states.

5.2. Topological Shiba states in collinear chains with spin-orbit coupling

Recently there has been great efforts to engineer a topological superconductor device relying on magnetic adatoms deposited on top of a conventional superconductor by scan-

ning tunneling microscopy (STM) techniques. According to recent results [13], Majorana fermions (MFs) seem to emerge, while the spin-polarized measurement indicates a ferromagnetic (FM) orientation of the atomic spins. However, this type of ordering leads to Majorana fermions, only if spin-orbit coupling (SOC) is involved (see section 4.2.2). The latter could either arise intrinsically, i.e. be a property of the superconductor itself or it could be due to a Rashba type of spin-orbit coupling [83] that arises from the broken inversion associated with the surface. In fact, both are plausible scenarios for Pb which owes already an intrinsic spin-orbit coupling. Even more, it has been shown that the Rashba spin-orbit coupling in Pb quantum well structures can be considerably large and tunable [114, 115, 116, 117]. The momentum splitting associated with the spin-orbit coupling can even reach an order of $\delta k \sim 0.05\, k_F$, where k_F is the Fermi-momentum ($\hbar = 1$).

Very recently theoretical progress has been put forward in this direction: in Ref. [118] the authors consider a ferromagnetic metallic wire on top of a superconductor with intrinsic spin-orbit coupling. On the other hand Ref. [119] discusses magnetic atoms placed in a ferromagnetic fashion on a superconducting surface with Rashba spin-orbit coupling. Therefore both proposals treat very different regimes. In the first proposal the wire is metallic by itself, whereas the second proposal relies on the emergence of Shiba-bound states in the superconducting substrate that effectively behave like a one-dimensional wire.

Following the previous sections and very similar to the proposal in Ref. [119], we investigate the topological properties of Shiba bands that arise from collinear spin-chains on top of a superconducting surface with Rashba spin-orbit coupling. First, we infer the energetically favored magnetic ordering for the parameter space relevant for current experiments. By assuming identical adatoms, owing a fixed magnetic moment S, we explore the competition of ferromagnetic, antiferromagnetic and spiral ordering. The magnetic atoms interact via a Ruderman-Kittel-Kasuya-Yosida (RKKY) superexchange interaction [18, 19, 20], which is mediated by the electrons of the superconducting substrate. Due to the presence of spin-orbit coupling, the resulting superexchange includes an anisotropic term, more precisely a Dzyaloshinsky-Moriya (DM) contribution. This interaction favors spiral ordering of spins. On the other hand, ferromagnetic and antiferromagnetic orders are stabilized by the crystal field anisotropy mentioned earlier, which favors spins to align parallel to an easy axis (see Fig. 5.9). By taking into account the various interactions, we extract the resulting phase diagram and find that the collinear orders are established if the Ising anisotropy of the crystal field dominates over the Dzyaloshinsky-Moriya interaction. Furthermore we investigate the stability of the collinear order against quantum and thermal fluctuations.

Later on in this section we discuss the topological properties of Shiba-bands arising from either ferromagnetic or antiferromagnetic (AFM) atomic chains. The symmetry properties of these systems gives rise to a rich phase diagram of Majorana fermion phases with 0, 1, or 2 MFs per chain edge. One can access the three phases by changing the adatom distance, the strength of the spin-orbit coupling and the value of the magnetic moment. The phases with two Majorana fermions per chain edge are topologically protected by chiral symmetry. By identifying the relevant gap closings in the Shiba bandstructure, responsible for all the topological phase transitions, we provide insight for manipulating and tailoring the Majorana phases.

5.2.1. Magnetic phases

In this section we discuss the ordering of magnetic atoms on top of a Rashba spin-orbit

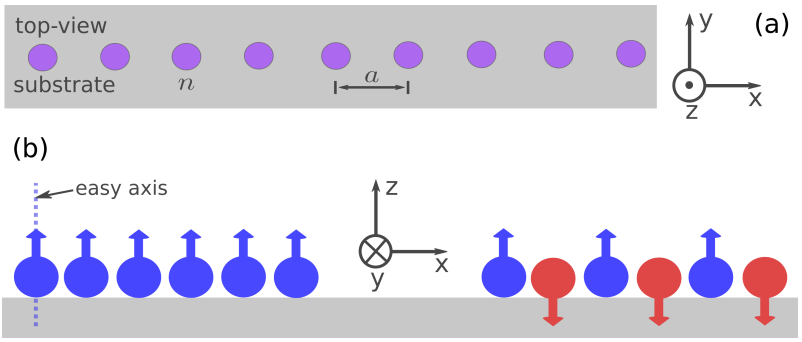

Figure 5.9.: (a) Top view of a chain of adatoms placed on top of a superconducting surface with Rashba spin-orbit coupling. (b) Side view of the hybrid structure. Crystal field effects violate spin rotational symmetry and favor an easy spin axis for the magnetic ordering (here the $\hat{z}$ direction). On the other hand, spin-orbit coupling induces a Dzyaloshinsky-Moriya (DM) interaction. When the spin anisotropy dominates over the DM interaction, the adatoms order in a ferromagnetic (FM) or antiferromagnetic (AFM) fashion, depending on the chain constant a. (Figure from Ref. [120])

coupled metallic surface. The RKKY superexchange mediated by the substrate favors a spiral order. However, in the presence of an Ising anisotropy both, FM and AFM orders, can be stabilized and are stable against quantum and thermal fluctuations.

RKKY interaction for a Rashba spin-orbit coupled metal

We start with the Hamiltonian of a two-dimensional metallic substrate with Rashba SOC:

$$H_{\text{metal}} = \sum_{\boldsymbol{k}} \psi^\dagger_{\boldsymbol{k}}\, h_{\boldsymbol{k}}\, \psi_{\boldsymbol{k}}\,, \tag{5.42}$$

where $h_{\boldsymbol{k}} = \xi_{\boldsymbol{k}} + \alpha(\boldsymbol{k}\times\hat{\boldsymbol{z}})\cdot\boldsymbol{\sigma}$ is a 2×2 matrix in spin-space and $\psi^\dagger_{\boldsymbol{k}} = (c^\dagger_{\boldsymbol{k}\uparrow}, c^\dagger_{\boldsymbol{k}\downarrow})$ is the corresponding spinor. Furthermore, $c^\dagger_{\boldsymbol{k}\sigma}$ creates an electron with momentum $\boldsymbol{k}$ and spin σ. The quadratic electronic dispersion, $\xi_{\boldsymbol{k}} = k^2/2m - \mu$, can be linearized around the Fermi-momentum ($k_F = \sqrt{2m\mu}$), i.e. $\xi_{\boldsymbol{k}} = v_F(k - k_F)$, where $k = |\boldsymbol{k}|$ and v_F is the Fermi-velocity. Accordingly the effective momentum splitting δk corresponds to a SOC strength $\alpha = v_F\,\delta k/k_F$. As depicted in Fig. 5.10, the Hamiltonian $h_{\boldsymbol{k}}$ can be readily diagonalized via a $\pi/2$-rotation about the $\hat{\boldsymbol{k}}$-axis:

$$e^{i\frac{\pi}{4}\hat{\boldsymbol{k}}\cdot\boldsymbol{\sigma}}\, h_{\boldsymbol{k}}\, e^{-i\frac{\pi}{4}\hat{\boldsymbol{k}}\cdot\boldsymbol{\sigma}} = \xi_k + \alpha k\sigma_z\,, \tag{5.43}$$

where $\hat{\boldsymbol{k}} = \boldsymbol{k}/k$. The respective eigenenergies are given by $\xi_{k\lambda} = \xi_k + \lambda\alpha k \approx v_F(k - k_\lambda)$, with $k_\lambda \approx k_F(1 - \alpha\lambda/v_F)$, corresponding to the two helicity bands $\lambda = \pm 1$. We define the Matsubara Green's function in the helicity subspace: $g_\lambda(k, i\omega) = (i\omega - \xi_{k\lambda})^{-1}$ and obtain

$$(i\omega - \xi_k - \alpha k\sigma_z)^{-1} = \sum_{\lambda=\pm} \frac{1+\lambda\sigma_z}{2}\, g_\lambda(k, i\omega)\,. \tag{5.44}$$

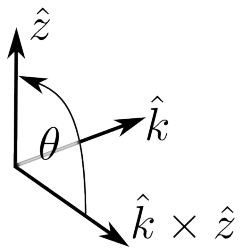

Figure 5.10.: Rotation about the $\hat{\boldsymbol{k}}$-axis by an angle $\theta = \pi/2$.

According to above result, the electronic Green's function is given by

$$\begin{aligned} G_{\boldsymbol{k}}(i\omega) &= \sum_{\lambda=\pm} \frac{1+\lambda e^{-i\frac{\pi}{4}\hat{\boldsymbol{k}}\cdot\sigma}\sigma_z\, e^{i\frac{\pi}{4}\hat{\boldsymbol{k}}\cdot\boldsymbol{\sigma}}}{2}\, g_\lambda(k,i\omega) \\ &= \sum_{\lambda=\pm} \frac{1+\lambda(\hat{\boldsymbol{k}}\times\hat{\boldsymbol{z}})\cdot\boldsymbol{\sigma}}{2}\, g_\lambda(k,i\omega)\,. \end{aligned} \tag{5.45}$$

Now, we consider classical spins $\boldsymbol{S}_i$ with magnitude $|\boldsymbol{S}_i| = S$, placed at positions $\boldsymbol{R}_i = ia\hat{\boldsymbol{x}}$, with $i = 1, ..., N$. In addition, we assume that the interaction between the adatoms is driven by an exchange interaction mediated by the conduction electrons of the substrate. The coupling between adatoms and conduction electrons can be parametrized by an exchange energy J (see Eq. (5.5)). Given that J is a small coupling constant and that the local modifications of the electronic spectrum in the substrate are negligible, we can follow a standard one-loop expansion and obtain an effective spin-spin interaction. The so called RKKY interaction reads [18, 19, 20]

$$H_{\mathrm{RKKY}} = -\frac{J^2}{2}\sum_{ij}\chi_{ij}^{\alpha\beta}S_i^\alpha S_j^\beta\,. \tag{5.46}$$

The spin-spin susceptibility can be derived using the Green's function given in Eq. (5.45):

$$\chi_{ij}^{\alpha\beta} = -T\sum_\omega \mathrm{Tr}_\sigma\left[\sigma_\alpha G(\boldsymbol{R}_i-\boldsymbol{R}_j,i\omega)\sigma_\beta G(\boldsymbol{R}_j-\boldsymbol{R}_i,i\omega)\right], \tag{5.47}$$

where $G(\boldsymbol{R},i\omega) = \int \frac{d\boldsymbol{k}}{(2\pi)^2}\, e^{i\boldsymbol{k}\cdot\boldsymbol{R}}G_{\boldsymbol{k}}(i\omega)$. Using the result in Eq. (5.45) we apply a quasi-classical expansion $\xi_{\boldsymbol{k}} \ll v_F k_F$ [120] and arrive at the well known result [121]

$$\begin{aligned} H_{\mathrm{RKKY}} &= -m\left(\frac{Jk_F}{\pi}\right)^2 \sum_{ij}\frac{\sin(2k_F|r_{ij}|)}{(2k_F r_{ij})^2} \\ \times\ &\left\{\cos(2m\alpha r_{ij})\boldsymbol{S}_i\cdot\boldsymbol{S}_j + [1-\cos(2m\alpha r_{ij})]S_i^yS_j^y + \sin(2m\alpha r_{ij})\left(\boldsymbol{S}_i\times\boldsymbol{S}_j\right)_y\right\}, \end{aligned} \tag{5.48}$$

where $\nu_F = m/2\pi$ is the density of states at the Fermi-level for each spin-band and $r_{ij} \equiv (i-j)a$. Eq. (5.48) holds in the limit $k_F a \gg 1$. For vanishing SOC, we recover the usual spin rotationally invariant Heisenberg interaction, proportional to $\boldsymbol{S}_i\cdot\boldsymbol{S}_j$,

$$J_{\mathrm{RKKY}}(r) = -m\left(\frac{Jk_F}{\pi}\right)^2\frac{\sin(2k_F|r|)}{(2k_Fr)^2}. \tag{5.49}$$

This implies a ferromagnetic interaction between neighboring spins if $J_{\mathrm{RKKY}} < 0$ and a ferromagnetic interaction if $J_{\mathrm{RKKY}} > 0$. On the other hand, a finite SOC produces both an Ising interaction $S_i^y S_j^y$ and a DM interaction $(\boldsymbol{S}_i \times \boldsymbol{S}_j)_y$. By taking into account that the rotation of a classical spin, $\boldsymbol{S}_j$, by an angle $\theta_{ij} = 2m\alpha r_{ij}$ with respect to $\boldsymbol{S}_i$ is given by

$$\boldsymbol{S}_j(\theta_{ij}) \equiv \cos(\theta_{ij})\boldsymbol{S}_j + \sin(\theta_{ij})\,(\hat{\boldsymbol{y}} \times \boldsymbol{S}_j)\ , \tag{5.50}$$

we may rewrite Eq. (5.48) compactly as follows [121]:

$$H_{\mathrm{RKKY}} = \sum_{ij} J_{\mathrm{RKKY}}(r_{ij})\ \ \boldsymbol{S}_i \cdot \boldsymbol{S}_j(\theta_{ij}). \tag{5.51}$$

This implies that the SOC would generally establish a spiral configuration, with a tilting angle $\theta_{i+1,i} = 2ma\alpha$ between neighboring spins (see Fig. 5.11). However, crystal field effects (CFEs) of the substrate may violate spin rotational invariance so that the magnetic moment of adatoms tends to point along the axis perpendicular to the surface (easy axis). This anisotropy gives rise to an additional term appearing in the total spin-Hamiltonian, which depends on the microscopic details and generally assumes a rather complicated form. However on phenomenological grounds we will consider the simplest term allowed, which has the form

$$H_{\mathrm{CF}} = -\frac{D}{2}\sum_i (S_i^z)^2\,, \qquad (D > 0). \tag{5.52}$$

It accounts for the broken spin-rotational invariance and emerges from a coupling of spin $\boldsymbol{S}$ with the angular momentum $\boldsymbol{L}$ of the deposited atom, i.e. $H_{s-o} = \lambda\,\boldsymbol{L}\cdot\boldsymbol{S}$ [122]. If $|g\rangle$ is the ground state multiplet of the atom and $|e\rangle$ the first excited state, then $D \sim \lambda^2 |\,\langle g|L_z|e\rangle\,|^2/E_{ge} \neq 0$, where E_{ge} is the energy difference between ground state and first excited state. When the atom is placed on a high-symmetry point of the surface the matrix-elements of the other angular momentum components L_x and L_y may vanish.

In STM experiments the nearest neighbor exchange energy as well as the crystal field anisotropy, D, can be measured. The next neighbor RKKY interaction of various metals is of the order [14, 123]

$$|J_{\mathrm{RKKY}}(a)| \leq |J_{\max}(a)| \equiv m\left(\frac{Jk_F}{\pi}\right)^2 \frac{1}{(2k_F a)^2} \sim 0.1\,\mathrm{meV}\,. \tag{5.53}$$

Furthermore the anisotropy D has been determined in Ref. [14] to be approximately given by $\sim 1\,\mathrm{meV}$ or even larger [123]. According to that the chosen parameter-space for the calculations of the subsequent paragraphs should cover $D/J_{\max}(a) \lesssim 10$.

Classical magnetic ground state

In this paragraph, we discuss the possible magnetic phases (see Fig. 5.12), arising from the competition of spin-orbit coupling and crystal field effects. Whereas SOC favors a spiral ordering the latter may stabilize a FM or AFM ordering depending on the adatomic spacing. For the beginning we treat the spins classically, thus assuming that $|\boldsymbol{S}_i| = S$ with

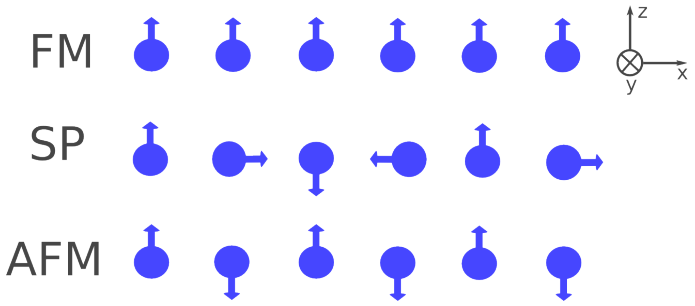

Figure 5.11.: Possible scenarios for the classical magnetic ground state: spiral (SP) with a tilting angle $\theta_{i,i+1}$ between neighboring spins, ferromagnetic (FM) and antiferromagnetic (AFM) ordering parallel to an easy axis. (Figure from Ref. [120])

a fixed magnitude S. In the classical limit: $S \to \infty$ whereas $J \to 0$, so that JS remains finite. Later we will discuss the stability of the classical ground state against quantum and thermal fluctuations.

There are various ways to determine the classical ground state of the Hamiltonian $H_{\rm cl} = H_{\rm CF} + H_{\rm RKKY}$. In this section we pursue a rather qualitative discussion and we prefer to apply a trial configuration $\boldsymbol{S}_i(\vartheta) = S\cos(\vartheta i)\hat{\boldsymbol{z}} - S\sin(\vartheta i)\hat{\boldsymbol{x}}$ with a tilting angle of $\theta_{i,i+1} = \vartheta$ between neighboring spins. This particular ordering can be motivated by the fact that (i) CFEs energetically favor a magnetization along the easy axis (z-axis) and (ii) the DM interaction mixes the z and x components of spins, such that the spins tend to lie in the xz-plane. Under these conditions, the ground state is defined by the optimal tilting angle ϑ, which minimizes the classical Hamiltonian:

$$H_{\rm cl}(\vartheta) = -\frac{DS^2}{2}\sum_i \cos^2(\vartheta i) + \sum_{ij} J_{\rm RKKY}(r_{ij})S^2\cos[(2m\alpha - \vartheta/a)r_{ij}] \quad (5.54)$$

We minimize this Hamiltonian numerically with respect to ϑ for an infinite chain. In Fig. 5.12 we see that, depending on the relation between (i) exchange energy, JS, (ii) crystal field anisotropy, D, (iii) spin-orbit coupling, αk_F, and (iv) adatom spacing, a, the classical ground state assumes a ferromagnetic ($\vartheta_{\rm FM} = 0, 2\pi$), antiferromagnetic ($\vartheta_{\rm AFM} = \pi$) or spiral order ($\vartheta_{\rm SP} \neq \vartheta_{\rm FM,AFM}$). The stronger the spin-orbit coupling, the stronger the CF anisotropy has to be in order to compensate the tendency of the system to form a spiral.

The transition between various phases is of first order. In order to understand their origin we discuss the phase-transitions in the following:

1. Increasing the atomic spacing the order can switch from FM to AFM and vise versa. This can be seen from the spatial dependence of the RKKY interaction (5.49).

2. In addition to that a transition between these phases can be achieved by increasing the Rashba spin-orbit coupling, α, which happens for the following reason: for the parameters $\alpha = 0$ and $k_F a/\pi = 5.27$ the classical order is ferromagnetic [see Fig. 5.12(b)], i.e. $\vartheta_{\rm FM} = 0$. For finite spin-orbit-coupling the nearest neighbor RKKY interaction in (5.54) is multiplied by a factor $\cos(2m\alpha a)$, which changes its sign when $m\alpha/k_F a = \mathrm{acos}(0)/(2k_F a)$. This corresponds exactly to the transition from FM to AFM observed in Fig. 5.12(b).

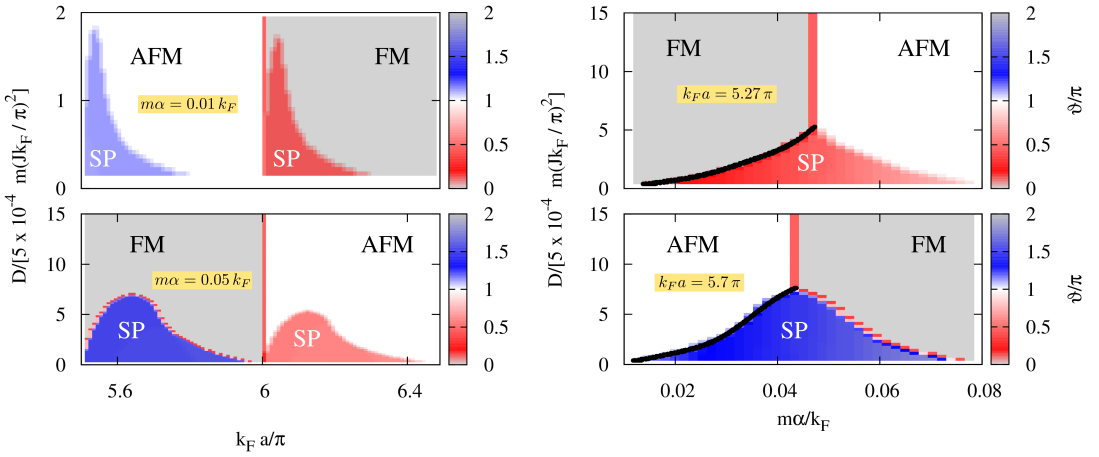

Figure 5.12.: Phase diagrams for the classical magnetic ground state: The tilting angle ϑ defines the FM ($\vartheta_{\mathrm{FM}} = 0, 2\pi$), the AFM ($\vartheta_{\mathrm{AFM}} = \pi$) and the spiral configuration ($\vartheta_{\mathrm{SP}} \neq \vartheta_{\mathrm{FM,AFM}}$). (a) ϑ as a function of atomic spacing, a, and crystal field anisotropy, D. The presented diagrams were calculated for two values of the Rashba spin-orbit coupling strength α. (b) ϑ depending on spin-orbit coupling, α and anisotropy D. Black lines show the analytical result for the phase-transition, D^*, in (5.55). (Figure from Ref. [120] with slight modifications)

3. In order to understand the transition between spiral and collinear magnetic order we refer to Eq. (5.54). For an infinitely long chain the first term vanishes, unless the tilting angle ϑ is given by 0 or π. According to that the energy in the spiral phase is minimized by an angle $\vartheta_{\mathrm{SP}} = 2m\alpha a$. We obtain the condition for the phase-transition between collinear and spiral configuration by comparing the corresponding classical energy scales, i.e. $H_{\mathrm{cl}}(\vartheta_{\mathrm{FM,AFM}}) = H_{\mathrm{cl}}(\vartheta_{\mathrm{SP}})$, yielding the critical value

$$D^*_{\mathrm{FM,AFM}} = 2\sum_{\delta} J_{\mathrm{RKKY}}(r_\delta)[\cos(2m\alpha a\delta - \vartheta_{\mathrm{FM,AFM}}\delta) - \cos(\vartheta_{\mathrm{FM,AFM}}\delta)]. \tag{5.55}$$

Here $D^*_{\mathrm{FM,AFM}}$ indicates the transition between spiral and, either FM or AFM order. Furthermore, we sum over neighbors δ in Eq. (5.55). In Fig. 5.12(b) we compare the analytical result of Eq. (5.55) (black line) with the numerical minimization.

In Fig. 5.12 the crystal field anisotropy, D, is displayed in units of $m(Jk_F/\pi)^2$, while the RKKY interaction is of the order $J_{\max}(a) \sim 6 - 8 \times 10^{-4}\, m(Jk_F/\pi)^2$. Therefore our calculations cover the parameter-space $D/J_{\max}(a) \lesssim 15$ consistent with the experimental situation discussed previously. We conclude that a sufficient crystal field anisotropy D favors a collinear magnetic order over the spiral magnetic order which is induced by the finite spin-orbit coupling α.

Thermal and quantum fluctuations

In this part we will investigate the stability of the collinear ferromagnetic (FM) and antiferromagnetic (AFM) phases against thermal and quantum fluctuations. Under the assumption that the classical ground state coincides with the real ground state of the spin-system

one can employ a Holstein-Primakoff transformation, i.e. a bosonization of spins, in order to derive the corresponding quasiparticle excitations. To this end we introduce the bosonic operators b_i and $b_i^\dagger$ with $[b_i,\, b_j^\dagger] = \delta_{ij}$. Here i and j refer to the adatom sites. In the limit of large spin S and up to second order in the operators b_i and $b_i^\dagger$ the Holstein-Primakoff-transformation reads [124]

$$S_j^x = (\pm 1)^j \sqrt{S/2}\,(b_j^\dagger + b_j)\,, \quad S_j^y = i\sqrt{S/2}\,(b_j^\dagger - b_j)\,, \quad S_j^z = (\pm 1)^j (S - b_j^\dagger b_j) \tag{5.56}$$

In addition, $\pm$ corresponds to the FM $(+)$ and the AFM $(-)$ cases, respectively. We immediately find that the spin fulfills the commutator relations

$$[S_i^\eta,\, S_j^\nu] = i\,\delta_{ij}\,\epsilon_{\delta\eta\nu} S_j^\delta. \tag{5.57}$$

At this point we use the transformation (5.56) and separate the Hamiltonian $H = H_{\mathrm{RKKY}} + H_{\mathrm{CF}}$ in orders $H^{(m)}$ of the operators b_i and $b_i^\dagger$. The classical ground state energy is given by

$$H^{(0)} = -\frac{NDS^2}{2} + \sum_{ij} J_{\mathrm{RKKY}}(r_{i-j})(\pm 1)^{i-j} S^2\, \cos(2m\alpha r_{ij}) \tag{5.58}$$

The linear term $H^{(1)}$ vanishes, whereas the bilinear term is given by

$$\begin{aligned} H^{(2)} &= \frac{S}{2}\sum_{ij} J_{\mathrm{RKKY}}(r_{ij})\left[(\pm 1)^{i-j}\cos(2m\alpha r_{ij}) - 1\right]\left(b_i^\dagger b_j^\dagger + b_i b_j\right) \\ &+ \frac{S}{2}\sum_{ij} J_{\mathrm{RKKY}}(r_{ij})\left[(\pm 1)^{i-j}\cos(2m\alpha r_{ij}) + 1\right]\left(b_i^\dagger b_j + b_j^\dagger b_i\right) \\ &- S\sum_{ij} J_{\mathrm{RKKY}}(r_{ij})\,(\pm 1)^{i-j}\cos(2m\alpha r_{ij})\left(b_i^\dagger b_i + b_j^\dagger b_j\right) \\ &+ \frac{D}{2}(2S-1)\sum_i b_i^\dagger b_i\,. \end{aligned} \tag{5.59}$$

The Hamiltonian can be readily diagonalized in momentum space. To this end we introduce the Fourier components

$$\begin{aligned} \gamma_k^{(1)} &= \frac{D}{2}\left(S - \frac{1}{2}\right) + \frac{S}{2}\sum_j e^{ikj}\, J_{\mathrm{RKKY}}(r_j)\left[(\pm 1)^{i-j}\cos(2m\alpha r_j) + 1\right] \\ &\quad - S\sum_j J_{\mathrm{RKKY}}(r_j)\,(\pm 1)^{i-j}\cos(2m\alpha r_j), \\ \gamma_k^{(2)} &= \frac{S}{2}\sum_j e^{ikj}\, J_{\mathrm{RKKY}}(r_j)\left[(\pm 1)^{i-j}\cos(2m\alpha r_j) - 1\right], \end{aligned} \tag{5.60}$$

such that the Hamiltonian assumes the form

$$H^{(2)} = \sum_k \left[\gamma_k^{(1)}\left(b_k^\dagger b_k + b_{-k}^\dagger b_{-k}\right) + \gamma_k^{(2)}\left(b_k^\dagger b_{-k}^\dagger + b_k b_{-k}\right)\right]. \tag{5.61}$$

In order to diagonalize $H^{(2)}$ a Bogoliubov transformation $b_k = u_k\beta_k - v_k\beta_{-k}^\dagger$ is performed with $u_k = \cosh(\eta_k)$, $v_k = \sinh(\eta_k)$ and $\tanh(2\eta_k) = \gamma_k^{(2)}/\gamma_k^{(1)}$, yielding

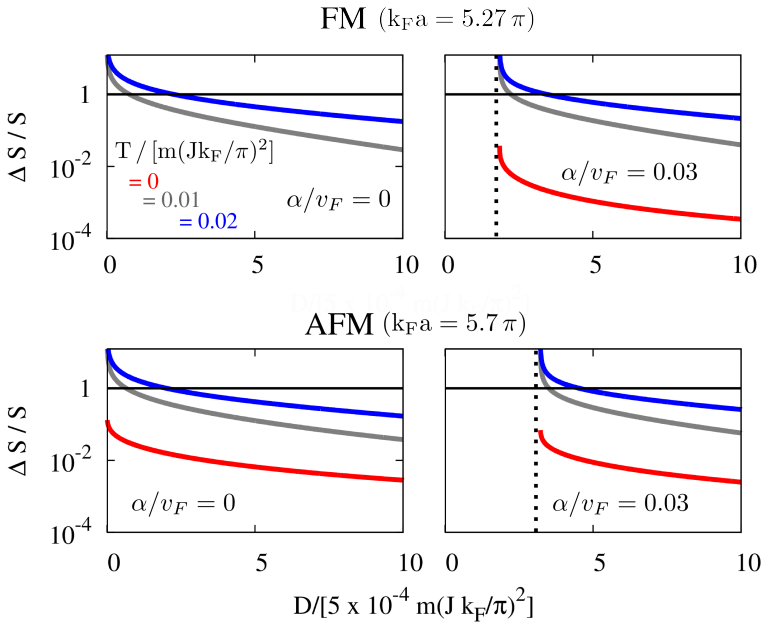

Figure 5.13.: Sublattice magnetization measured from its ground state value, ΔS ($S = 15/2$), as a function of anisotropy D for different temperatures T and spin-orbit coupling α for both, AFM and the FM configuration. The dashed lines indicate the transition into the spiral phase. (Figure from Ref. [120])

$$H^{(2)} = \sum_k \omega_k \beta_k^\dagger \beta_k . \tag{5.62}$$

Here the dispersions of spin-waves are given by $\omega_k = \sqrt{\left[\gamma_k^{(1)}\right]^2 - \left[\gamma_k^{(2)}\right]^2}$. We investigate the stability of the FM/AFM order by calculating the amount of sub-lattice magnetization, i.e.

$$M_\pm = -\frac{1}{N}\sum_{j=1}^{N}(\pm 1)^j \langle S_j^z \rangle = S - \frac{1}{N}\sum_k \langle b_k^\dagger b_k \rangle .$$

Using the Bogoliubov operators and defining the Bose-distribution $n_k = \langle \beta_k^\dagger \beta_k \rangle$ we arrive at the sublattice magnetization measured from its ground state value,

$$\Delta S = S - M = \frac{1}{N}\sum_k n_k u_k^2 + (1+n_k)v_k^2 , \tag{5.63}$$

where we have assumed that $\mathrm{sgn}(\langle S_1^z \rangle) = 1$. In Fig. 5.13 we show ΔS for different temperatures T and spin-orbit couplings α as a function of crystal field anisotropy D. For the atomic spin we use $S = 15/2$ which has been observed for a cluster of five iron atoms [41]. Furthermore, we display various temperatures correspond to the temperature range $T \sim 0 - 1\,K$, in accordance to the experimental value (5.53) and an atomic spacing of $k_F a/\pi = 5.5 - 6.5$.

For $T = \alpha = D = 0$ the AFM sublattice magnetization diverges, thus the magnetic order is destroyed. This is due to non-vanishing quantum-fluctuations which manifests

in a non-vanishing $v_k \neq 0$. On the other hand, ΔS vanishes for the FM configuration because $v_k = 0$. For finite temperature but still $\alpha = D = 0$ both, FM and AFM orders, are destroyed. The Ising anisotropy D leads to a pinning of the spin-direction along the easy-axis. This effectively induces an excitation gap in the spin-waves' dispersion ω_k. Consequently the ΔS remains finite and small for the experimental parameters of D that have been discussed before. Increasing the spin-orbit coupling weakly, modifies the AFM sublattice magnetization, in the FM case however it leads to finite quantum-fluctuations and a divergent deviation ΔS at the classical phase boundary to the spiral phase.

We want to remind the thoughtful reader that the Mermin-Wagner theorem can not be applied in our case. It states that continuous symmetries can not be spontaneously broken at finite temperature in systems of low dimensions ($d \leq 2$) and with short-range interactions. Since in the case at hand the isotropy is broken by crystal field effects the theorem is not applicable anymore. In fact, we observe that the FM and AFM order are stable against fluctuations.

5.2.2. Rashba spin-orbit coupled superconductor

In a conventional superconductor spin orbit coupling has stringent consequences on superconducting correlations. More precisely, it induces spin-triplet pairing amplitudes very similar to the case of nanowires on top of a s-wave superconductor which has been discussed in section 4.2.2. In the presence of Rashba spin-orbit coupling and s-wave superconductivity the Hamiltonian of of a two-dimensional metal is given by [125]

$$H_{\text{sc}} = \frac{1}{2}\sum_{\boldsymbol{k}} \psi^\dagger_{\boldsymbol{k}} \underbrace{\left[\xi_k \tau_z + \alpha \tau_z (\boldsymbol{k} \times \hat{\boldsymbol{z}}) \cdot \tilde{\boldsymbol{\sigma}} - \Delta \tau_y \sigma_y\right]}_{h_{\boldsymbol{k}}} \psi_{\boldsymbol{k}} \tag{5.64}$$

where the Pauli-matrices, $\boldsymbol{\tau}$, are defined in particle-hole space and $\psi^\dagger_{\boldsymbol{k}} = (c^\dagger_{\boldsymbol{k}\uparrow},\, c^\dagger_{\boldsymbol{k}\downarrow},\, c_{-\boldsymbol{k}\uparrow},\, c_{-\boldsymbol{k}\downarrow})$ is the corresponding spinor. Following the procedure of the previous section we perform a rotation to a basis in which the Hamiltonian (5.64) is diagonal in the spin-indices , i.e.

$$e^{i\frac{\pi}{4}\hat{\boldsymbol{k}}\cdot\tilde{\boldsymbol{\sigma}}}\, h_{\boldsymbol{k}} e^{-i\frac{\pi}{4}\hat{\boldsymbol{k}}\cdot\tilde{\boldsymbol{\sigma}}} = \xi_k \tau_z + \alpha k \sigma_z - \Delta \tau_y \sigma_y \,.$$

Mind that in particle-hole representation the spin-operator is given by $\tilde{\boldsymbol{\sigma}} = (\tau_z\sigma_x, \sigma_y, \tau_z\sigma_z)$. Within this basis the Gor'kov Nambu Green's function can be readily calculated. We obtain

$$\begin{aligned}\hat{G}_{\boldsymbol{k}}(i\omega) &= e^{-i\frac{\pi}{4}\hat{\boldsymbol{k}}\cdot\tilde{\boldsymbol{\sigma}}}\left[i\omega - \xi_k\tau_z - \alpha k\sigma_z + \Delta\tau_y\sigma_y\right]^{-1} e^{i\frac{\pi}{4}\hat{\boldsymbol{k}}\cdot\tilde{\boldsymbol{\sigma}}} \\ &= \sum_{\lambda=\pm} \frac{1+\lambda(\hat{\boldsymbol{k}}\times\hat{\boldsymbol{z}})\cdot\tilde{\boldsymbol{\sigma}}}{2} \frac{i\omega + \xi_{k\lambda}\tau_z - \Delta\tau_y\sigma_y}{(i\omega)^2 - \Delta^2 - \xi^2_{k\lambda}}. \end{aligned} \tag{5.65}$$

Here Δ is a s-wave order parameter, which is choosen to be real. The presence of the Rashba SOC induces triplet pairing correlations in the anomalous parts of the Gor'kov Nambu Green's function, i.e.

$$\Delta(\hat{\boldsymbol{k}}\times\hat{\boldsymbol{z}})\cdot\tilde{\boldsymbol{\sigma}}\;\tau_y\sigma_y = \Delta\left(\sin\varphi_{\boldsymbol{k}}\tau_x\sigma_z - \cos\varphi_{\boldsymbol{k}}\tau_y\right)\,,$$

where $\tan\varphi_{\boldsymbol{k}} = k_y/k_x$. For systems with spin-orbit interaction but purely local pairing interaction, like electron-phonon interaction, only the singlet order parameter component has to be treated in a self-consistent fashion in terms of the BCS gap-equation [126]. The triplet order parameter is identically zero, but triplet pairing correlations appear due to Rashba SOC.

RKKY interaction

Previously we discussed the RKKY interaction mediated by a normal conducting metal with Rashba SOC. Technically the RKKY interaction (5.47) can be calculated as in the normal state but with the electronic Green's function replaced by the Gor'kov Nambu Green's function and the spin replaced by the operator $\tilde{\boldsymbol{\sigma}}/2 = (\tau_z\sigma_x, \sigma_y, \tau_z\sigma_z)/2$. However, the static susceptibility is only weakly modified in the superconducting state. This is simply because the energy integration in (5.47) is merely depending on high energies ω, i.e. $\Delta \ll \omega \lesssim v_F/r$.

This is true as far as continuum quasiparticle excitations are concerned, for which the perturbative treatment in (5.47) is a valid approximation. However, sub-gap Shiba states that are a direct consequence of magnetic adatoms contribute an additional term to the effective superexchange. In spite of the fact that the number of Shiba states is relatively small (compared to the number of the bulk accessible states) it has been recently shown [104] that their contribution to the RKKY interaction can become important and favors an AFM ordering. The Shiba contribution dominates if the condition $k_F r > \xi/r$ is fulfilled which is true for the material parameters (Al) used in this reference and the atomic spacing that has been assumed ($r \sim 100\,\mathrm{nm}$). Here, however, we assume an adatom spacing of the order of $1\,\mathrm{nm}$ and a coherence length of $\xi \sim 80\,\mathrm{nm}$ (Pb). According to that we obtain $k_F r < \xi/r$, which means that Shiba states do not lead to significant modifications of the results found previously for a normal metallic substrate.

5.2.3. Shiba states from chains with collinear magnetic order

We assume that a classical collinear magnetic order $\boldsymbol{S}_n = (\pm 1)^n S\tau_z\sigma_z$ has been realized, where $(+)$ and $(-)$ correspond to the FM and AFM order respectively. The magnetic atoms align along a chain in x-direction with their respective position given by $\boldsymbol{R}_n = na\hat{\boldsymbol{x}}$. Analogous to section 5.1.1 we derive the Shiba states from the BdG equation (5.6) but with the Green's function $\hat{G}_{\boldsymbol{k}}$ replaced by (5.65). With this the BdG equation can be recast in the form

$$\sum_j \Big[V_i\delta_{ij} - V_i\hat{G}(r_{ij}\hat{\boldsymbol{x}}, \varepsilon)V_j \Big]\phi_j = 0\,, \tag{5.66}$$

where $V_i = JS(\pm 1)^i\tau_z\sigma_z$ is the local magnetization, $\hat{G}(r_{ij}\hat{\boldsymbol{x}}, \varepsilon) = \sum_{\boldsymbol{k}} e^{ik_x r_{ij}}\hat{G}_{\boldsymbol{k}}(\varepsilon)$ is the Green's-function in real space and $r_{ij} = |i-j|a$. We assume that neighboring atoms are well separated, i.e. $k_F a \gg 1$ and in addition to that we consider energies deep inside the gap, i.e. $\varepsilon \ll \Delta$. To this end we perform both, an expansion in energy ε/Δ and in couplings to higher order neighbors. Then the Green's-function in the quasiclassical approximation $\xi_{\boldsymbol{k}}/v_F \ll k_F$ can be written in the convenient form

$$\begin{aligned}
\hat{G}(\mathbf{0}, \varepsilon) &\approx -\pi\nu_F(\varepsilon/\Delta - \tau_y\sigma_y)\,, \\
\hat{G}(r\hat{\boldsymbol{x}}, 0) &\approx \pi\nu_F\sqrt{\frac{2}{\pi k_F|r|}}e^{-|r|/\xi}e^{im\alpha r\,\sigma_y}\left[\tau_z\sin(k_F|r| - \tfrac{\pi}{4}) + \tau_y\sigma_y\cos(k_F|r| - \tfrac{\pi}{4})\right].
\end{aligned} \tag{5.67}$$

The solution of Eq. (5.66) determines the energies and wavefunctions of the Shiba midgap states. It can be expressed in terms of an effective Schrödinger equation $\sum_j H_{ij}\phi_j = \varepsilon\phi_i$

with

$$H_{ij} = \delta_{ij}\left[\frac{\Delta}{\pi\nu_F JS}(\pm 1)^i \tau_z\sigma_z - \Delta\,\tau_y\sigma_y\right] - \hat{G}(-r_{ij}\hat{\boldsymbol{x}}, 0)\,\frac{\Delta}{\pi\nu_F} \tag{5.68}$$

The first term accounts for local magnetic exchange as well as s-wave superconductivity, whereas the the second term couples nearest and higher order neighbors. In particular we identify a kinetic energy proportional to τ_z, spin-orbit coupling $\tau_z\sigma_y$, a triplet pairing amplitude τ_y and an s-wave component $\tau_y\sigma_y$. Mind that we have neglected a self-consistent treatment of the superconducting gap for the same reasoning discussed in section 5.1.1.

Symmetries

In the absence of magnetic order the hybrid structure depicted in Fig. 5.9 holds a C_{2v} point-group symmetry. According to that it is invariant under the reflection operation σ_{yz} on the yz-plane, the reflection σ_{xz} on the xz-plane and the π-rotation around the z-axis C_2. Within our spinor-formalism the operators are given by $\sigma_{xz} = i\sigma_y$, $\sigma_{yz} = i\tau_z\sigma_x I$ and $C_2 = i\tau_z\sigma_z I$, where $I\,x = -x$ is the inversion operation of the x-component. The presence of either magnetic order breaks the usual time-reversal symmetry operation $\mathcal{T} = i\sigma_y\mathcal{K}$, because $\mathcal{T}^\dagger\tau_z\sigma_z\mathcal{T} = -\tau_z\sigma_z$. Likewise it breaks the reflection symmetries, i.e. $\sigma_{yz}^\dagger\tau_z\sigma_z\sigma_{yz} = -\tau_z\sigma_z$ and $\sigma_{xz}^\dagger\tau_z\sigma_z\sigma_{xz} = -\tau_z\sigma_z$. This however means that the operator $\Theta = \sigma_{xz}\mathcal{T} = \mathcal{K}$ commutes with the Hamiltonian and constitutes an effective time-reversal symmetry. Together with this the inherent particle-hole symmetry $\Xi = \tau_x\mathcal{K}$ gives rise to the chiral symmetry $\Pi = \tau_x$. Because $\Theta^2 = \Xi^2 = \Pi^2 = 1$ the system falls into the BDI symmetry class which implies a topological $\mathbb{Z}$ invariant. In fact we will observe topological phases with an integer number of Majorana fermions. In the particular case we identify phases with 0, 1 and 2 Majorana states at each end of the atomic chain.

5.2.4. Topological superconductivity in ferromagnetic chains

We begin with the ferromagnetic chain and transform the Hamiltonian (5.68) to momentum space spanned by the Brillouin zone (BZ) $k \in (-\pi/a,\, \pi/a]$,

$$H_k = t_k\tau_z - v_k\tau_z\sigma_y + (\Delta + \mathcal{D}_k)\tau_y\sigma_y - d_k\tau_y - M\,\tau_z\sigma_z\,. \tag{5.69}$$

Here we introduced $M = \Delta/\pi\nu_F JS$ and the Fourier components

$$\begin{aligned}
t_k &= \sum_{n=1}^{\infty}\frac{\Delta}{2\pi\nu_F}\mathrm{Tr}\left[\tau_z\hat{G}(na\hat{x}, 0)\right]\cos(kan),\\
v_k &= \sum_{n=1}^{\infty}\frac{\Delta}{2\pi\nu_F}\mathrm{Tr}\left[\tau_z\sigma_y\hat{G}(na\hat{x}, 0)\right]\sin(kan),\\
\mathcal{D}_k &= \sum_{n=1}^{\infty}\frac{\Delta}{2\pi\nu_F}\mathrm{Tr}\left[\tau_y\sigma_y\hat{G}(na\hat{x}, 0)\right]\cos(kan),\\
d_k &= \sum_{n=1}^{\infty}\frac{\Delta}{2\pi\nu_F}\mathrm{Tr}\left[\tau_y\hat{G}(na\hat{x}, 0)\right]\sin(nka).
\end{aligned} \tag{5.70}$$

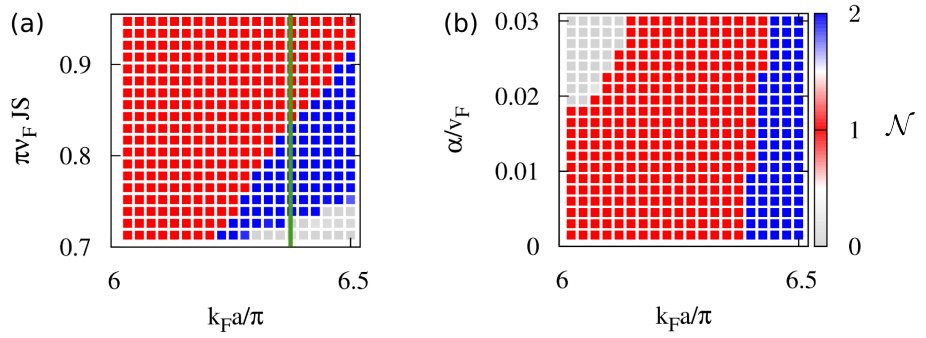

Figure 5.14.: The $\mathbb{Z}$ topological invariant as defined in Eq. (5.72), for varying adatom spacing a and (a) magnetic exchange energy JS ($\alpha = 0.01\, v_F$) or (b) normalized SOC strength α ($\pi\nu_F JS = 0.85$). In both cases, we find topological phases harboring 1 or 2 MFs per chain edge. (Figure from Ref. [120])

The first term, t_k, corresponds to the kinetic energy, v_k to spin-orbit coupling, $\mathcal{D}_k$ to a momentum dependent s-wave pairing correlation and d_k to a triplet pairing amplitude. The Hamiltonian is very similar to the nanowire with proximity induced superconductivity (4.26). The only difference is the appearance of a triplet component of the superconducting gap, which however does not change the symmetries of the system. Due to the presence of chiral symmetry, $\Pi = \tau_x$, the Hamiltonian can be block off-diagonalized by the unitary transformation $U = (\tau_x + \tau_z)/\sqrt{2}$, i.e.

$$H_k' = U H_k U^\dagger = \begin{pmatrix} 0 & A_k \\ A_k^\dagger & 0 \end{pmatrix}. \tag{5.71}$$

Here the upper block is given by $A_k = t_k - i d_k - M\sigma_z - [v_k - i(\Delta + \mathcal{D}_k)]\sigma_y$. It obeys the relation $A_k = A_{-k}^*$ and is therefore purely real at the inversion-symmetric points $k = 0,\ \pi$. Since $\det(H_k') = \det(A_k)\det(A_{-k})$ an gap closing can only occur if the determinant of A_k vanishes. In general $z_k = \det(A_k) = |\det(A_k)|\exp(i\theta_k)$ is a complex number with the winding angle θ_k. It has been shown [127] that the topological invariant can be written by the winding number

$$\mathcal{N} = \frac{1}{2\pi}\int_{-\pi/a}^{\pi/a} dk \frac{d\theta_k}{dk}. \tag{5.72}$$

In Fig. 5.14 we show the winding number as a function of the adatom spacing a, magnetic exchange energy JS and SOC strength α. Phases with zero, one or two MFs per edge are accessible. We additionally observe that the phase diagram exhibits MF bound states even for *very small* values of spin orbit coupling α. This is reasonable from the discussion of the nanowire model in section 4.2.2. There α did not enter the criterion for the topological phase transition but rather determined the exponential decay of the edge-state wavefunctions. In our case the topological phase transition happens when $\det(A_k) = 0$, which yields the following relations,

$$v_k(\Delta + \mathcal{D}_k) - t_k d_k = 0\,, \tag{5.73}$$

$$t_k^2 + (\Delta + \mathcal{D}_k)^2 - M^2 - d_k^2 - v_k^2 = 0. \tag{5.74}$$

The first relation is immediately fulfilled for the inversion symmetric points $k = 0$ and $k = \pi/a$, because v_k and d_k are odd under inversion, i.e. $v_{k=0,\pi/a} = d_{k=0,\pi} = 0$. It might

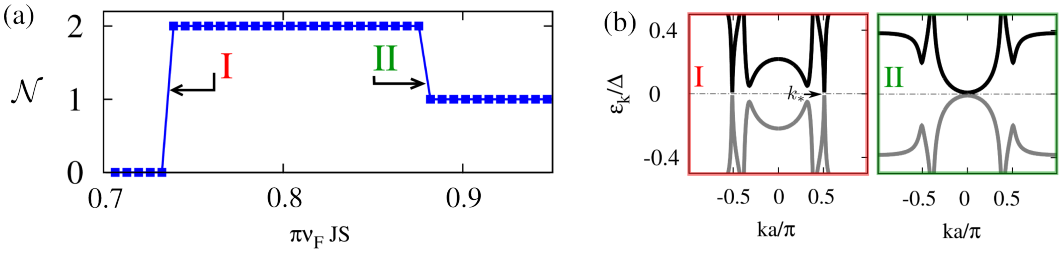

Figure 5.15.: (a) The winding number $\mathcal{N}$ of (5.72) depending on magnetic exchange energy JS along the green line in Fig. 5.14(a). (b) Gap closings of the energy dispersions ε_k, occuring exactly at the phase transition points I and II. The transition (II) $\mathcal{N} = 2 \to \mathcal{N} = 1$ arises due to a gap closing at the inversion symmetric momentum $k = 0$. Instead, the transition (I) $\mathcal{N} = 0 \to \mathcal{N} = 2$ arises from gap closings at the non-inversion-symmetric points $\pm k_*$. (Figures from Ref. [120])

be true for non-inversion symmetric points $\pm k_*$ as well. For instance, considering nearest neighbor couplings only, i.e. $t_k = t_1 \cos(ka)$, $v_k = v_1 \sin(ka)$, $\mathcal{D}_k = \mathcal{D}_1 \cos(ka)$ and $d_k = d_1 \sin(ka)$ yields the condition

$$k_* a = \pm \text{acos}\left[\frac{v_1 \Delta}{(d_1 t_1 - v_1 \mathcal{D}_2)}\right]. \tag{5.75}$$

At this point it might be reasonable to repeat our discussion from the very beginning: Majorana fermions in a topological superconductor are related to the quasiparticle operators $d_k = u_k c_k + v_k c_{-k}^\dagger$, where $c_k^\dagger$ and c_k are creation and annihilation operators of spinless fermions[2]. It is immediately obvious that under the condition $u_k = v_k$ and $k = 0,\ \pi/a$ the operators d_k behave like Majorana operators, i.e. $d_0 = d_0^\dagger$. This is true for non-inversion symmetric points as well. In this case we may define combinations

$$\gamma_1 = d_{k_*} + d_{-k_*} \tag{5.76}$$
$$\gamma_2 = i(d_{k_*} - d_{-k_*}) \tag{5.77}$$

which are Majorana operator as well as they fulfill the condition $\gamma_i = \gamma_i^\dagger$ under the particle-hole symmetry $d_{k_*} = d_{-k_*}^\dagger$. Due to the fact that each MF consists is associated to two fermions at momenta $\pm k_*$ we may expect the appearance of four Majorana fermions, two per end of the one-dimensional system.

Furthermore, at $k = 0,\ \pi/a$ the second relation (5.74) yields the condition $M^2 = t_{k=0,\pi/a}^2 + (\Delta + \mathcal{D}_{k=0,\pi/a})^2$, akin to the criterion found for the nanowire models. A similar condition can be found for the non-inversion symmetric points $\pm k_*$ by plugging them into (5.74).

In Fig. 5.15 (a) the numerically evaluated winding number $\mathcal{N}$ is shown, along the green cut in Fig. 5.14 (a). We observe two transitions indicated by (I) and (II):

(I) $\mathcal{N} = 0 \to 2$: As discussed in the last paragraph the first transition coincides with the gap closing at non-inversion symmetric points $\pm k_*$. This can be seen in Fig. 5.15 (b) where the lowest energy-bands are shown.

[2] for illustrative reasons we neglect the spin for a moment

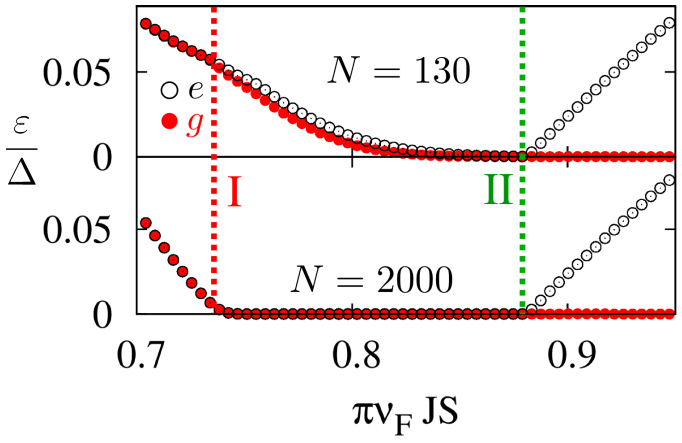

Figure 5.16.: The two lowest positive eigenenergies in red and black for two different lengths of the chain ($N = 130$ and $N = 2000$). The transitions (I) and (II) of Fig. 5.15 are indicated. Note that in order to obtain well localized MF bound states and validate the bulk-boundary correspondence predictions, quite long chains are required. (Figures from Ref. [120])

(II) $\mathcal{N} = 2 \to 1$: The second transition can be attributed to a gap closing at $k = 0$ (see Fig. 5.15 (b)), involving only one instead of two Majorana fermions.

In the spirit of the bulk-boundary correspondence we check our predictions by solving the BdG equation (5.66) together with (5.67). In Fig. 5.16 we show the two lowest positive eigenvalues, the ground state energy (g) and the energy of the first excited state (e), as a function of exchange energy J. Furthermore we indicate the transitions (I) and (II) by red and green dotted lines. As expected the winding number $\mathcal{N}$ corresponds to the number of zero energy edge-states. Nonetheless, in the $\mathcal{N} = 2$ phase truly-zero bound states only appear for very long chains. This has to be contrasted with the region where $\mathcal{N} = 1$. There, the zero energy bound state seems to be stabilized already for shorter lengths of the chain.

In Fig. 5.17 the wavefunctions of the left and right Majorana fermions in the one and two Majorana phase are shown. In the one Majorana phase the wavefunctions are strongly localized. In the two Majorana phase the wavefunctions leak into the bulk. Furthermore they show an oscillatory behavior that is associated with the wave vector $\pm k_*$. More precisely, since the MF wavefunctions should be real they oscillate with $\cos(k_* aj)$ and $\sin(k_* aj)$. This explains the oscillating behavior shown in Fig. 5.17(b) and (c).

5.2.5. Topological superconductivity in antiferromagnetic chains

The present paragraph follows closely the analysis carried out for the FM chain. First we transform (5.68) to momentum space yielding the Schrödinger equation

$$H_k^0 \phi_k + H^M \phi_{k+Q} = \varepsilon \phi_k, \tag{5.78}$$

with $H_k^0 = H_k = t_k \tau_z - v_k \tau_z \sigma_y + (\Delta + \mathcal{D}_k)\tau_y \sigma_y - d_k \tau_y$ and $H^M = M\, \tau_z \sigma_z$. Futhermore, $Q = \pi/a$ is the antiferromagnetic wavevector and $\phi_k = (u_{k\uparrow}, u_{k\downarrow}, v_{k\uparrow}, v_{k\downarrow})^{\mathrm{T}}$ is the spinor containing the particle and hole components. In constrast to the ferromagnetic chain the antiferromagnetic order holds a discrete transilational invariance by two lattice sites. Thus, the reduced Brillouin zone (RBZ) extends from $k = -\pi/2a$ to $k = \pi/2a$ and the

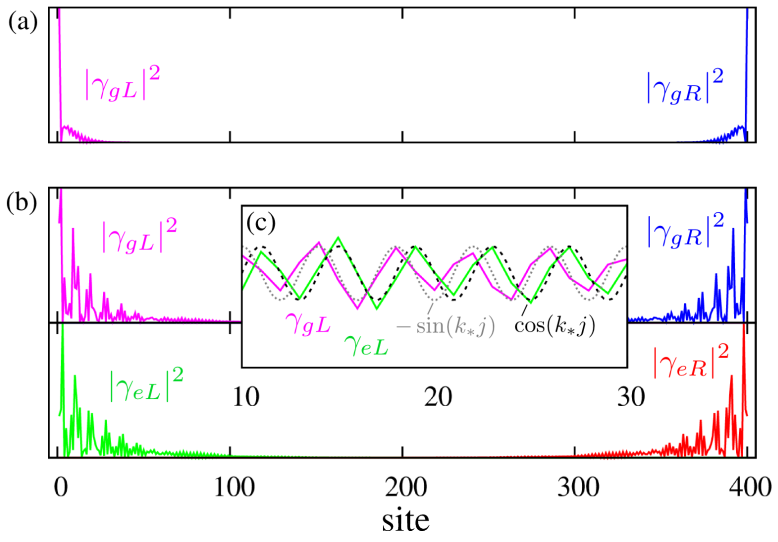

Figure 5.17.: Wavefunctions corresponding to Fig. 5.16 for the ground state (g) and the first excited state (e). The left and right Majorana edge modes are labeled by (L) and (R) respectively. (a) The MF wavefunction within the 1MF phase is strongly localized. (b) The wave functions inside the 2MF phase leak into the bulk and oscillate with an inverse wavelength k_* (see close-up of the wavefunctions in (c)). (Figure from Ref. [120])

BdG equation (5.1) reads

$$\begin{pmatrix} H^0_{k-Q/2} & M\tau_z\sigma_z \\ M\tau_z\sigma_z & H^0_{k+Q/2} \end{pmatrix} \begin{pmatrix} \phi_{k-Q/2} \\ \phi_{k+Q/2} \end{pmatrix} = \varepsilon \begin{pmatrix} \phi_{k-Q/2} \\ \phi_{k+Q/2} \end{pmatrix} . \tag{5.79}$$

By introducing the Pauli matrices ρ_i, which act in the antiferromagnetic subspace, we may write the Hamiltonian as

$$H_k = H^0_{k,+} + H^0_{k,-}\rho_z + M\tau_z\rho_x\sigma_z \, . \tag{5.80}$$

Here we introduced the combinations $A_{k,\pm} = (A_{k-Q/2} \pm A_{k+Q/2})/2$. With the appropriate coefficients in Eq. (5.69) we directly retrieve the explicit form of the Hamiltonian,

$$\begin{aligned} H_k = {} & t_{k,+}\tau_z + t_{k,-}\tau_z\rho_z - v_{k,+}\tau_z\sigma_y - v_{k,-}\tau_z\rho_z\sigma_y \\ & + (\Delta + \mathcal{D}_{k,+})\tau_y\sigma_y + \mathcal{D}_{k,-}\tau_y\rho_z\sigma_y - d_{k,+}\tau_y - d_{k,-}\tau_y\rho_z \\ & - M\tau_z\rho_x\sigma_z \, . \end{aligned} \tag{5.81}$$

We already know that the Hamiltonian is purely real and therefore commutes with the *effective* time reversal symmetry operator $\Theta = \mathcal{K}$. In the reduced BZ we have to introduce the operator $\mathcal{K}'$ which does not act on the wavevector Q but on k and is given by $\mathcal{K} = \rho_x\mathcal{K}'$. Furthermore we find that the Hamiltonian commutes with the operator $\mathcal{O} = \rho_z\sigma_y$ which constitutes another symmetry of the system. It consist of translation by one lattice site, ρ_z, and a spin-flip operation, σ_y, leaves the antiferromagnetic order invariant. Accordingly we may introduce the additional operator $\Theta' = i\mathcal{O}\Theta = \rho_y\sigma_y\mathcal{K}'$. Similarly we find another chiral symmetry $\Pi' = \tau_x\rho_z\sigma_y$ in addition to the chiral operator

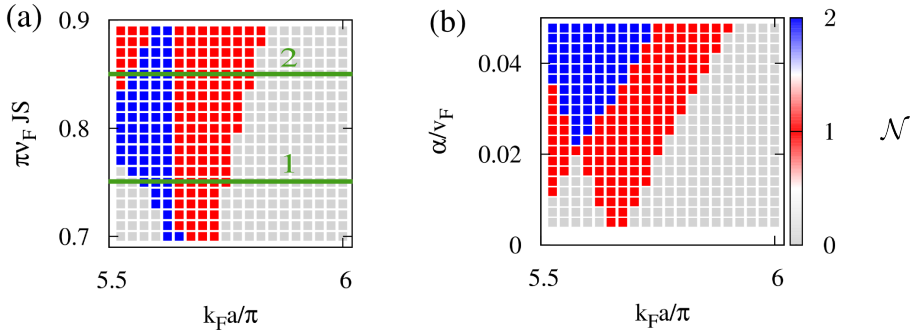

Figure 5.18.: The $\mathbb{Z}$ topological invariant (winding number) as defined in Eq. (5.86), for varying adatom spacing a and (a) magnetic exchange energy JS ($\alpha = 0.03\, v_F$) or (b) normalized SOC strength α ($\pi\nu_F JS = 0.85$). In both cases, we find topological phases harboring 1 or 2 MFs per chain edge. (Figure from Ref. [120])

$\Pi = \tau_x$ which we declared previously. In summary we have $\Theta^2 = \Theta'^2 = \Pi^2 = \Pi'^2 = 1$, which defines the BDI $\oplus$ BDI symmetry class. Furthermore this shows that the Hamiltonian (5.81) can be block-diagonalized by a unitary transformation

$$U = \frac{\rho_y + \rho_z}{\sqrt{2}} \frac{\rho_z\sigma_z + \sigma_y}{\sqrt{2}} e^{-i\frac{\pi}{4}\sigma_y}\,, \tag{5.82}$$

which yields $UH_kU^\dagger = \frac{1}{2}\sum_\sigma (1+\sigma\sigma_z)\otimes H_{k\sigma}$, with the blocks

$$\begin{aligned} H_{k\sigma} &= (t_{k,+} - \sigma v_{k,-})\tau_z + (t_{k,-} - \sigma v_{k,+})\tau_z\rho_y + M\tau_z\rho_z \\ &+ [\sigma(\Delta + \mathcal{D}_{k,+}) - d_{k,-}]\tau_y\rho_y + (\sigma\mathcal{D}_{k,-} - d_{k,+})\tau_y\,. \end{aligned} \tag{5.83}$$

For each spin-subspace, spin-up and spin-down, the Hamiltonian assumes the form of the ferromagnetic Shiba model (5.69) but with the spin operators σ_i replaced by the Pauli matrices ρ_i operating in the AFM subspace. According to that we may identify the various corresponding contributions:

- kinetic energy: $t_k \to t_{k,+} - \sigma v_{k,-}$,
- spin-orbit coupling: $v_k \to \sigma v_{k,+} - t_{k,-}$,
- magnetic exchange: $M \to M$,
- singlet superconductivity: $\Delta + \mathcal{D}_k \to \sigma(\Delta + \mathcal{D}_{k,+}) - d_{k,-}$,
- triplet superconductivity: $d_k \to d_{k,+} - \sigma\mathcal{D}_{k,-}$.

Because of this correspondence we may follow the previous analysis and define a topological invariant for each block (5.83). First, we block off-diagonalize the Hamiltonian $H_{k\sigma}$, i.e.

$$H'_{k\sigma} = UH_{k\sigma}U^\dagger = \begin{pmatrix} 0 & A_{k\sigma} \\ A^\dagger_{k\sigma} & 0 \end{pmatrix}, \tag{5.84}$$

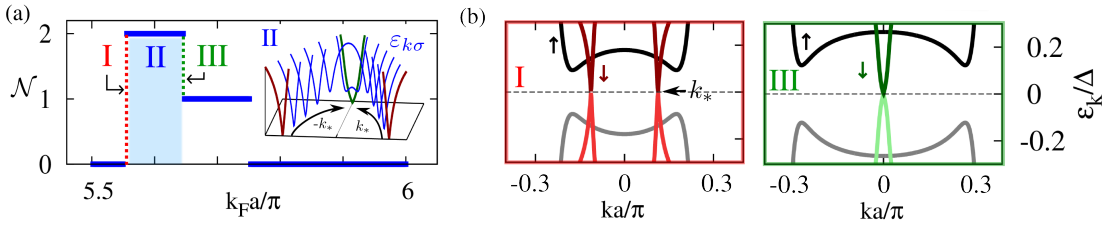

Figure 5.19.: (a) The topological invariant $\mathcal{N}$ along cut 1 in Fig. 5.19. (b) The band-gap closings associated with the transitions I and III. The inset in (a) illustrates that the two minima of the spin-down band merge at III into a gap closing at $k = 0$. (Figures from Ref. [120])

by the unitary transformation $U = (\tau_x + \tau_z)/\sqrt{2}$. A gap closing occurs if the determinant $\det(H_k) = \prod_\sigma \det(A_{k\sigma})[\det(A_{k\sigma})]^*$ becomes zero. For each block $\det(A_{k\sigma}) = |\det(A_{k\sigma})| \exp(i\theta_{k\sigma})$ is a complex number with the angle $\theta_{k\sigma}$. We may define the complex number

$$z_k = \prod_\sigma |\det(A_{k\sigma})| \exp(i\theta_{k\sigma}) = \exp\left(i \sum_\sigma \theta_{k\sigma}\right) \prod_\sigma |\det(A_{k\sigma})| \tag{5.85}$$

which has the complex angle $\theta_k = \sum_\sigma \theta_{k\sigma}$. Similar to (5.72) the topological invariant can be defined by

$$\mathcal{N} = \frac{1}{\pi} \int_{-\pi/2a}^{\pi/2a} dk \, \frac{d\theta_k}{dk}. \tag{5.86}$$

In Fig. 5.18 the winding number is plotted depending on adatom spacing a, magnetic exchange energy JS and spin orbit coupling α. We find that like in the FM case, phases with zero, one or two Majorana fermions are accessible. Furthermore a finite spin-orbit coupling is needed in order to pass into the topological non-trivial phase. This is in stark contrast to the FM chain where the spin-orbit coupling can be small. Furthermore, the 2 MF phase opens up for increasing spin-orbit coupling, in contrast to the FM case where it was nearly independent on spin-orbit coupling.

In order to investigate the various transitions between phases with different topological invariants we consider the two cuts (green line) in Fig. 5.18.

1. The topological invariant for the first cut is presented in Fig. 5.19(a). The transitions I and III in panel (a) can be attributed to closings of the bands $\varepsilon_{k\sigma}$ which are eigenvalues of (5.83) (see panel (b)). Similarly to the FM case the transition (I) $\mathcal{N} = 0 \to 2$ is associated with closings at non-inversion symmetric momenta $\pm k_*$. In the inset of (a) we illustrate that the minima of the responsible spin-down band opens a gap within the region (II) and move towards $k = 0$ where the gap closing leads to the transition (III) $\mathcal{N} = 2 \to 1$. For a chain with finite length the lowest positive eigenvalues of (5.68) are presented in Fig. 5.20. The emergence of true zero modes in the two Majorana phase is only stabilized by relatively long chains, whereas the one Majorana phase is distinct already for short length of the chain. In accordance with this we assert that – like in the FM case – the Majorana wavefunction of the one MF phase is strongly localized. In the 2MF phase the gap closings at $\pm k_*$ imprint on the oscillating behavior of the MF wavefunctions (see

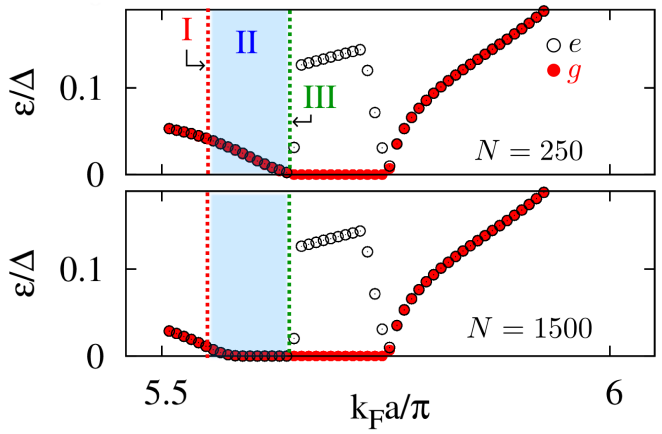

Figure 5.20.: The two lowest positive eigenenergies in red and black for two different lengths of the chain ($N = 250$ and $N = 1500$). The transitions (I) and (III) of Fig. 5.19 are indicated. Note that in order to obtain well localized MF bound states and validate the bulk-boundary correspondence predictions, quite long chains are required. (Figures from Ref. [120] with slight modifications)

Fig. 5.20(a)-(c)). The latter are extended over the bulk region on a length-scale of 500 atoms. This makes it difficult for an experimental realization.

2. The situation is different for the second cut in Fig. 5.18. This time the transitions between different MF phases exclusively arise from band-touchings at $k = 0$ [see Fig. 5.22(a) and (c)]. They coincide with the appearance of either one, zero and two zero energy modes in the finite system, as depicted in panel (b). The two MF phase is stable, already for shorter chain-lengths. The corresponding wavefunctions in the two MF phase are shown in Fig. 5.23 (a). Their oscillatory behavior can be deduced from the band-minima of the dispersions. In Fig. 5.23 (b) we show the wave function of the right ground state edge-state deep inside the 2MF phase (dark-blue) and close to the transition (II) (light-blue). A band mimium at $k = 0$ corresponds to the point $Q/2$ in the original BZ. This leads to an oscillation of the wavefunction on the length-scale of adatom spacing. On the other hand the band minima move away from this point when passing into the 2MF phase. This leads to a corresponding oscillation on a larger length-scale. In contrast to the two scenarios discussed before the Majorana wavefunctions can be localized already for shorter chains.

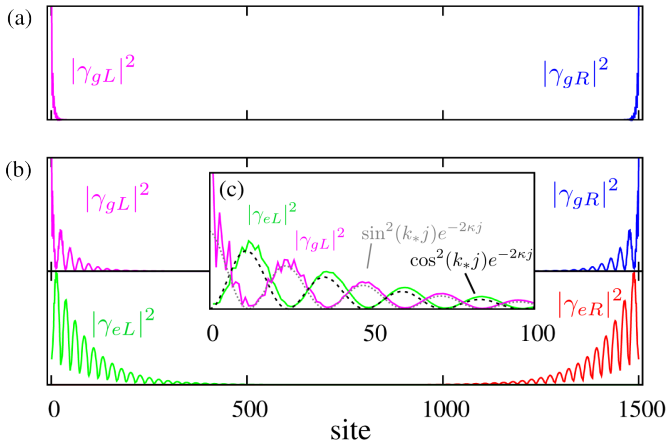

Figure 5.21.: Wavefunctions corresponding to Fig. 5.20 for the ground state (g) and the first excited state (e). The left and right Majorana edge modes are labeled by (L) and (R) respectively. (a) The MF wavefunction within the 1MF phase is strongly localized. (b) The wave functions inside the 2MF phase which leak into the bulk and oscillate with an inverse wavelength k_* (see close-up of the wavefunctions in (c)). (Figure from Ref. [120] with close-up (c) added)

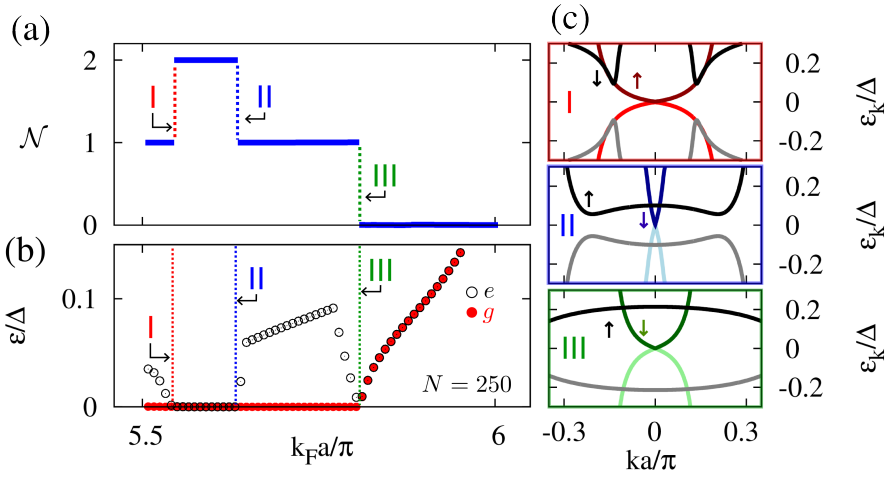

Figure 5.22.: (a) Winding number along the second cut in Fig. 5.18. (b) The transitions (I-III) coincide with the emergence of zero, one and two zero modes. (c) The corresponding band-touchings occur at the inversion-symmetric point $k = 0$. (Figure from Ref. [120])

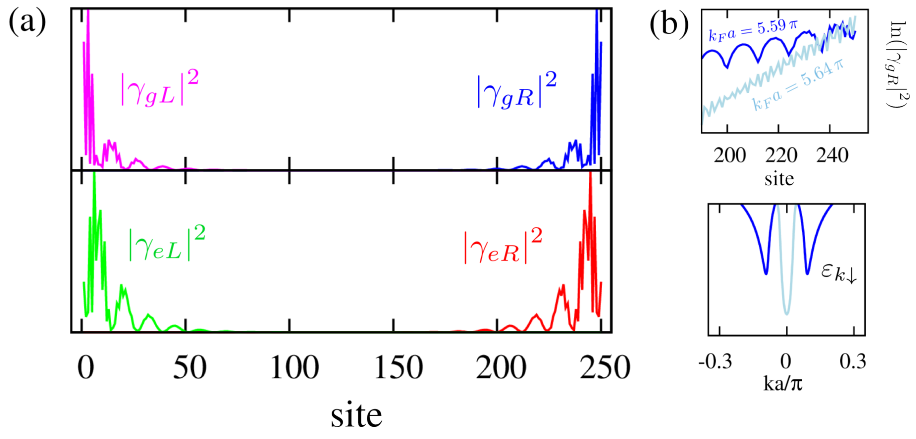

Figure 5.23.: Wavefunctions corresponding to Fig. 5.20 for the ground state (g) and the first excited state (e) within the 2MF phase of Fig. 5.22. The oscillatory behavior originates from the band-mimima of the energetically lowest band, which do not always coincide with $k = 0$. (Figures from Ref. [120])

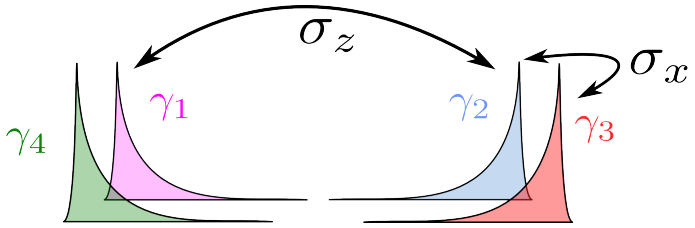

Figure 5.24.: New quantum computing perspectives: A *logical* Majorana qubit on a single chain.

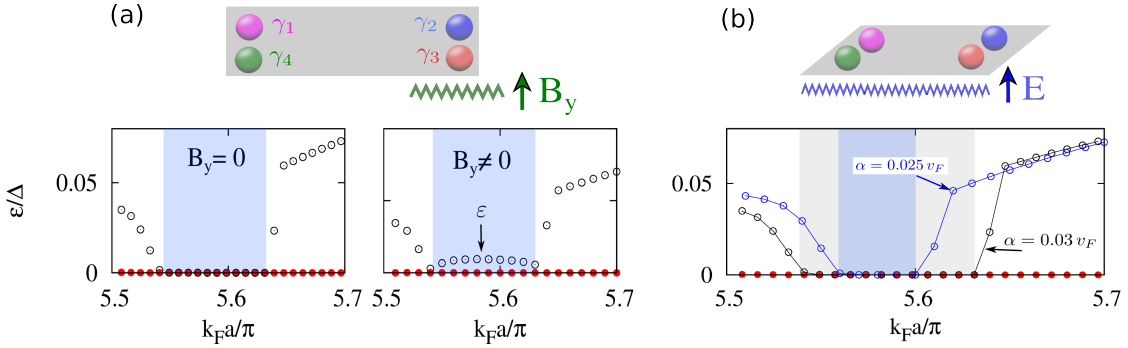

Figure 5.25.: (a) The coupling of γ_2 and γ_3 is realized by a *locally* applied magnetic field ($B_y = 0.02\,\Delta/\mu_B$). The first excited state has the energy ε. (b) A change in Rashba spin-orbit coupling moves the phase boundaries of the 1 and 2 MF phases. For specific adatom spacing a we can switch between these phases by applying electric fields.

5.3. Outlook: Manipulation of a Majorana logical qubit on a single chain

In the previous chapters we presented two alternative ways to engineer a topological superconductor using collinear magnetic adatom chains on top of conventional superconductors. We discussed directions on how to access different topological phases using external fields. For instance, in the setup presented in chapter 5.1 the application of a supercurrent and a magnetic field has been a necessarily criterion to realize a TSC. In the previous chapter 5.2 phases with different numbers of Majorana fermions have be obtained by, e.g., changing the effective Rashba spin orbit coupling. The latter can be tuned by applying electric fields.

In this short chapter we want to discuss perspectives on how to exploit these external control knobs in order to manipulate a Majorana qubit on a single adatom chain and use it for quantum computation processing. In the following we will present a very general idea which, however, requires further research in order to fully develop this approach. As discussed in section 4.2.3 a logical qubit can be formed by four Majorana operators γ_1, ..., γ_4, two of which make up a delocalized fermionic state, i.e., $d = \gamma_1 + i\gamma_2$ and $c = \gamma_3 + i\gamma_4$. In the basis of the two logical states $|\bar{0}\rangle \equiv |00\rangle$ and $|\bar{1}\rangle \equiv |11\rangle = c^\dagger d^\dagger |00\rangle$ we can define the Pauli-matrices

$$\sigma_x = -i\gamma_2\gamma_3, \qquad \sigma_y = i\gamma_1\gamma_3, \qquad \sigma_z = -i\gamma_1\gamma_2\,. \tag{5.87}$$

The four Majorana end-states emerge in the two-Majorana phase (see Fig. 5.22). In the

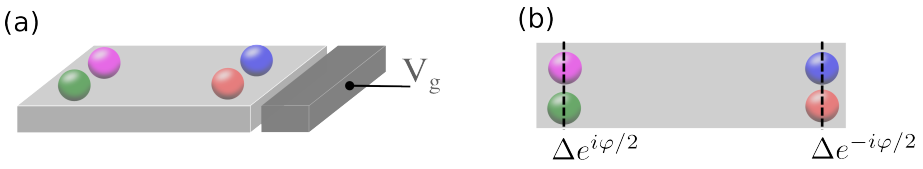

Figure 5.26.: (a) Charging effects can couple Majorana operators (b) Superconducting phase-gradient modifies the tunnel-coupling between Majorana fermions.

following we will consider the schematic picture in Fig. 5.24. In order to perform non - topological quantum computation, different Majorana operators have to be coupled:

- A magnetic field y-direction, that is applied *locally* at the right-hand side of the adatom chain, breaks the chiral symmetry which protects the 2MF phase. The hybridization of the Majorana fermions γ_2 and γ_3 leads to a finite energy ε (see Fig. 5.25(a)). For a weak magnetic field the effective low energy Hamiltonian reads

$$H = -i\varepsilon\,\gamma_2\gamma_3 = \varepsilon\,\sigma_x. \tag{5.88}$$

  Once the logical qubit is initialized in one of the logical qubit states $|\bar{0}\rangle$ or $|\bar{1}\rangle$ (see section 4.2.3), which are eigenstates of σ_z with eigenvalues ± 1, the coupling (5.88) leads to a rotation around the σ_x-axis with the characteristic frequency ε. This realizes superpositions of the qubit states. However, mind that the Majorana fermions on the left-hand side lose their topological protection and may be coupled by local perturbations.

- Electric fields are able to control the effective Rashba spin-orbit coupling. Fig. 5.25 (b) shows the energies of the ground state and first excited state for two different values of spin-orbit coupling. We find that for certain adatom spacing, a, a change in spin-orbit coupling leads to transitions between the phases with one or two MFs per edge. In this case, in order to pass from one topological phase into the other, the topological protection has to be lifted *only* right at the phase transtition. In contrast to the case discussed before the remaining Majorana edge states in the 1MF phase are still protected against local perturbatiions.

- Charging effects can couple the Majorana operators $\gamma_1, ..., \gamma_4$ (see Fig. 5.26 (a)). If the adatom chain is put onto a mesoscopic superconductor the occupation with an additional electronic charge costs an extra energy $E_C = e^2/2C$. Here C is the capacity of the superconductor. The coupling reads

$$H = E_C(d^\dagger d + c^\dagger c - n_g)^2\,, \tag{5.89}$$

  where the gate-charge, n_g, controls the number of excess charges.

- A superconducting phase-gradient applied modifies the tunnel-coupling (see Eq. (4.25)) by a phase dependent term [78, 128], e.g.,

$$H \sim i\epsilon\,\cos\left(\frac{\varphi}{2}\right)\,\gamma_1\gamma_2\,. \tag{5.90}$$

  In section 5.1 we have shown that Majorana phases are indeed accessible by applying a supercurrent. Furthermore, it has been demonstrated that Majorana states arising from helical atomic chains can be as well manipulated by a supercurrent [129].

These few examples demonstrate how a Majorana qubit may be manipulated using external fields. At the same time this provides additional ideas on how to couple a Majorana qubit to other solid state qubits.

Conclusion

The influence of *quasiparticle poisoning* on the properties of superconducting devices like the coherence of Josephson qubits [2, 3, 4, 5, 6], the current-voltage characteristics of Josephson arrays [130], and the accuracy of single-electron turnstiles [7, 8, 9] is an intense field of research. Very recently it has been demonstrated that an efficient quasiparticle-trapping minimizes the negative impact on the functionality of these devices [8, 28]. Furthermore it has been shown that tunneling of quasiparticles in Josephson-qubits can be coherently suppressed [4]. In addition, it is important to understand the underlying physics that leads to a non-equilibrium population of quasiparticles in superconducting electronic devices. In order to experimentally quantify the impact of quasiparticles, a controllable injection source and simultaneous measurement of the experimentally accessible quantity is required. Recently an on-chip injection of quasiparticles has been realized in superconducting qubits by a spatially separated but nearby quasiparticle source [3]. In comparison hybrid single-electron turnstiles have the advantage that the quasiparticle injection is an *inherent* part of single-charge tunneling. This also facilitates the accessibility from a theoretical point of view considerably.

In the first part of this thesis we presented a detailed study of the *non-equilibrium quasiparticle dynamics* in a hybrid normal-metal – superconductor – normal-metal single-electron turnstile, which is driven by a DC bias voltage and an AC pumping gate voltage. In chapter **3** we derived, starting from microscopic theory, a set of coupled equations that on one hand describe the tunneling of single-electron charges and on the other the time-evolution of the non-equilibrium quasiparticles distribution in the small superconducting island. Additionally, we derived a simplified kinetic equation which only depends on the total number of quasiparticles instead of their energy-dependent distribution function. Furthermore we demonstrated how the presence of non-equilibrium quasiparticles modifies the single-electron current through this device. Recent experiments by Maisi *et al.*[9], that were targeted to probe the dynamics of quasiparticles, confirm the validity of our model for a wide range of turnstile operation rates.

We observed that, within the turnstile protocol, the injected quasiparticles relax either due to electron-phonon interaction or due to quasiparticle escape into the normal conducting leads. Quasiparticle recombination is the dominant relaxation channel at high frequencies, whereas at low frequencies the electron-phonon interaction plays a minor role. In the latter limit single quasiparticle effects become important. In particular we identified the emergence of the parity effect with decreasing operation frequency. This is very similar to the equilibrium situation of superconducting SETs, where the parity effect appears with decreasing electronic temperature [11, 48, 49, 50].

We expect that our model will provide a deeper understanding of the dynamics of quasiparticles also in other systems like superconducting qubits where the repetition rates are comparable with typical turnstile frequencies [131].

The second part of the thesis is devoted to *topological superconductivity* and *Majorana fermions* in condensed matter systems. The quest for Majorana fermions in solid state devices has led to a great diversity of theoretical proposals. Among these we discussed heterostructures involving semiconducting nanowires, helical magnetic fields and magnetic adatoms (see chapter **4**). The basic ingredient appearing in all these devices is a spin-momentum locking. In proximity to conventional s-wave superconductors these systems develop effective p-wave superconductivity leading to the emergence of zero energy Majorana bound states. The latter appear due to non-trivial topological properties of the system and are protected by symmetry.

In chapter **5** we presented two alternative Majorana fermion platforms that rely on magnetic adatoms deposited on a superconducting surface. In the first model we discussed the possibility of generating an effective coupling of spin and momentum by applying external control fields, *without* involving any kind of intrinsic spin-orbit coupling. This can be realized by imposing a Zeeman field in combination with a supercurrent along a one-dimensional chain of antiferromagnetically ordered magnetic adatoms. The emergent Majorana fermions feature a characteristic local density with spectral weight suppressed at every second site. Furthermore, the Majorana states have a specific spin-polarization, a signature that can be measured with spin-sensitive STM probes. Adding a single adatom to the chain switches the polarization. This even-odd effect is associated with the particular symmetry of the Majorana wavefunctions.

The second model relies on collinear types of magnetic order in the presence of Rashba spin-orbit coupling and complies with the experimental situation of Ref. [13]. We studied the stability of ferromagnetic and antiferromagnetic orders and conclude that a crystal field anisotropy of the metallic substrate supports phases with collinear magnetic order. Furthermore we studied the emergence of Majorana fermions in this setup and identified rich phase-diagrams with several Majorana bound-states at the edges of the atomic wire. Finally, in chapter 5.3, we discussed perspectives on how to realize and manipulate a logical Majorana qubit on a single adatom chain. In the topological phase with two Majorana excitations per edge certain Majorana operators can be coupled by applying external fields, e.g., magnetic and electric fields or a supercurrent. Furthermore, if the adatom chain is put on a mesoscopic superconductor the charging energy provides an additional control knob to manipulate the Majorana qubit. In addition to that, we believe that these types of interactions provide possibilities to couple the Majorana qubit also to other solid state quantum information devices.

References

[1] J. Bardeen, L. N. Cooper, and J. R. Schrieffer, Phys. Rev. **108**, 1175 (1957).

[2] J. M. Martinis, M. Ansmann, and J. Aumentado, Phys. Rev. Lett. **103**, 097002 (2009).

[3] J. Wenner, Y. Yin, E. Lucero, R. Barends, Y. Chen, B. Chiaro, J. Kelly, M. Lenander, M. Mariantoni, A. Megrant, C. Neill, P. J. J. O'Malley, D. Sank, A. Vainsencher, H. Wang, T. C. White, A. N. Cleland, and J. M. Martinis, Phys. Rev. Lett. **110**, 150502 (2013).

[4] I. M. Pop, K. Geerlings, G. Catelani, R. J. Schoelkopf, L. I. Glazman, and M. H. Devoret, Nature **508**, 369 (2014).

[5] G. Catelani, R. J. Schoelkopf, M. H. Devoret, and L. I. Glazman, Phys. Rev. B **84**, 064517 (2011).

[6] J. Leppäkangas and M. Marthaler, Phys. Rev. B **85**, 144503 (2012).

[7] J. P. Pekola, J. J. Vartiainen, M. Mottonen, O.-P. Saira, M. Meschke, and D. V. Averin, Nat Phys **4**, 120 (2008).

[8] H. S. Knowles, V. F. Maisi, and J. P. Pekola, Applied Physics Letters **100**, 262601 (2012).

[9] V. F. Maisi, S. V. Lotkhov, A. Kemppinen, A. Heimes, J. T. Muhonen, and J. P. Pekola, Phys. Rev. Lett. **111**, 147001 (2013).

[10] J. P. Pekola, O.-P. Saira, V. F. Maisi, A. Kemppinen, M. Möttönen, Y. A. Pashkin, and D. V. Averin, Rev. Mod. Phys. **85**, 1421 (2013).

[11] G. Schön and A. D. Zaikin, EPL (Europhysics Letters) **26**, 695 (1994).

[12] V. Mourik, K. Zuo, S. M. Frolov, S. R. Plissard, E. P. A. M. Bakkers, and L. P. Kouwenhoven, Science **336**, 1003 (2012).

[13] S. Nadj-Perge, I. K. Drozdov, J. Li, H. Chen, S. Jeon, J. Seo, A. H. MacDonald, B. A. Bernevig, and A. Yazdani, Science , 1259327 (2014).

[14] A. A. Khajetoorians, J. Wiebe, B. Chilian, S. Lounis, S. Blugel, and R. Wiesendanger, Nat Phys **8**, 497 (2012).

[15] L. Yu, Acta Phys. Sin. **21**, 75 (1965).

[16] A. I. Rusinov, Zh. Eksp. Teor. Fiz. **56**, 2047 (1969), [Sov. Phys. JETP Lett. 29, 1101 (1969)].

[17] H. Shiba, Progress of Theoretical Physics **40**, 435 (1968).

[18] M. Ruderman and C. Kittel, Phys. Rev. **96**, 99 (1954).

[19] T. Kasuya, Prog. Theor. Phys. **16**, 45 (1956).

[20] K. Yosida, Phys. Rev. **106**, 893 (1957).

[21] A. Abrikosov, I. Dzialoshinskii, and L. Gorkov, *Quantum Field Theoretical Methods in Statistical Physics*, (International series of monographs in natural philosophy, v.4) Translation of Metody kvantovoi teorivi polya v statisticheskoi fizike (1965).

[22] G. Eliashberg, ZhETF **38(3)**, 966 (1960), [Sov. Phys. JETP 11(3), 696-702 (1960)].

[23] S. Vonsovsky, Y. A. Izyumov, and E. Kurmaev, *Superconductivity of Transition Metals*, Vol. 27 (Springer-Verlag Berlin Heidelberg New York) pp. 34–55.

[24] M. Kresch, M. Lucas, O. Delaire, J. Y. Y. Lin, and B. Fultz, Phys. Rev. B **77**, 024301 (2008).

[25] E. Wolf, J. Zasadzinski, J. Osmun, and G. Arnold, Journal of Low Temperature Physics **40**, 19 (1980).

[26] S. B. Kaplan, C. C. Chi, D. N. Langenberg, J. J. Chang, S. Jafarey, and D. J. Scalapino, Phys. Rev. B **14**, 4854 (1976).

[27] R. C. Dynes, V. Narayanamurti, and J. P. Garno, Phys. Rev. Lett. **41**, 1509 (1978).

[28] O.-P. Saira, A. Kemppinen, V. F. Maisi, and J. P. Pekola, Phys. Rev. B **85**, 012504 (2012).

[29] A. A. Abrikosov and L. P. Gor'kov, ZhETF **39(6)**, 1781 (1960), [Sov. Phys. JETP 12, 1243 (1961)].

[30] M. A. Woolf and F. Reif, Phys. Rev. **137**, A557 (1965).

[31] A. Yazdani, B. A. Jones, C. P. Lutz, M. F. Crommie, and D. M. Eigler, Science **275**, 1767 (1997).

[32] A. V. Balatsky, I. Vekhter, and J.-X. Zhu, Rev. Mod. Phys. **78**, 373 (2006).

[33] S.-H. Ji, T. Zhang, Y.-S. Fu, X. Chen, J.-F. Jia, Q.-K. Xue, and X.-C. Ma, Applied Physics Letters **96**, 073113 (2010).

[34] M. E. Flatté and J. M. Byers, Phys. Rev. Lett. **78**, 3761 (1997).

[35] M. I. Salkola, A. V. Balatsky, and J. R. Schrieffer, Phys. Rev. B **55**, 12648 (1997).

[36] J. Kondo, Progress of Theoretical Physics **32**, 37 (1964).

[37] P. W. Anderson, Journal of Physics C: Solid State Physics **3**, 2436 (1970).

[38] T. Matsuura, Progress of Theoretical Physics **57**, 1823 (1977).

[39] J. Bauer, A. Oguri, and A. C. Hewson, Journal of Physics: Condensed Matter **19**, 486211 (2007).

[40] K. J. Franke, G. Schulze, and J. I. Pascual, Science **332**, 940 (2011).

[41] A. A. Khajetoorians, B. Baxevanis, C. Hübner, T. Schlenk, S. Krause, T. O. Wehling, S. Lounis, A. Lichtenstein, D. Pfannkuche, J. Wiebe, and R. Wiesendanger, Science **339**, 55 (2013).

[42] T. Miyamachi, T. Schuh, T. Markl, C. Bresch, T. Balashov, A. Stohr, C. Karlewski, S. Andre, M. Marthaler, M. Hoffmann, M. Geilhufe, S. Ostanin, W. Hergert, I. Mertig, G. Schön, A. Ernst, and W. Wulfhekel, Nature **503**, 242 (2013).

[43] J. Bardeen, Phys. Rev. Lett. **6**, 57 (1961).

[44] T. Aref, A. Averin, S. van Dijken, A. Ferring, M. Koberidze, V. F. Maisi, H. Q. Nguyend, R. M. Nieminen, J. P. Pekola, and L. D. Yao, Journal of Applied Physics **116**, 073702 (2014).

[45] C. A. Neugebauer and M. B. Webb, Journal of Applied Physics **33**, 74 (1962).

[46] T. Dittrich, P. Hänggi, G.-L. Ingold, B. Kramer, G. Schön, and W. Zwerger, *Quantum Transport and Dissipation*, ISBN 3-527-29261-6 (Wiley-VCH Verlag, 1998) chapter 3: Single-Electron Tunneling (G. Schön), p. 149-212.

[47] H. Grabert and M. H. Devoret, eds., *Single Charge Tunneling*, NATO ASI Series B, Vol. 294 (Plenum Press, New York, 1992) chapter 6: Macroscopic Quantum Tunneling of Charge and Co-Tunneling (D.V. Averin and Yu. V. Nazarov), p. 217-247.

[48] P. Lafarge, P. Joyez, D. Esteve, C. Urbina, and M. H. Devoret, Phys. Rev. Lett. **70**, 994 (1993).

[49] T. M. Eiles, J. M. Martinis, and M. H. Devoret, Phys. Rev. Lett. **70**, 1862 (1993).

[50] J. M. Hergenrother, M. T. Tuominen, and M. Tinkham, Phys. Rev. Lett. **72**, 1742 (1994).

[51] B. Jankó, A. Smith, and V. Ambegaokar, Phys. Rev. B **50**, 1152 (1994).

[52] D. Golubev and A. Zaikin, Physics Letters A **195**, 380 (1994).

[53] F. W. J. Hekking, L. I. Glazman, K. A. Matveev, and R. I. Shekhter, Phys. Rev. Lett. **70**, 4138 (1993).

[54] J. Siewert, G. Schön, and A. Zaikin, *Quantum Dynamics of Submicron Structures*, edited by H. Cerdeira, B. Kramer, and G. Schön, NATO ASI Series, Vol. 291 (Springer Netherlands, 1995) pp. 489–502.

[55] A. F. G. Wyatt, V. M. Dmitriev, W. S. Moore, and F. W. Sheard, Phys. Rev. Lett. **16**, 1166 (1966).

[56] T. Kommers and J. Clarke, Phys. Rev. Lett. **38**, 1091 (1977).

[57] T. Klapwijk, J. van den Bergh, and J. Mooij, Journal of Low Temperature Physics **26**, 385 (1977).

[58] U. Eckern, A. Schmid, M. Schmutz, and G. Schön, Journal of Low Temperature Physics **36**, 643 (1979).

[59] M. Nahum, T. M. Eiles, and J. M. Martinis, Applied Physics Letters **65**, 3123 (1994).

[60] M. M. Leivo, J. P. Pekola, and D. V. Averin, Applied Physics Letters **68**, 1996 (1996).

[61] A. Heimes, V. F. Maisi, D. S. Golubev, M. Marthaler, G. Schön, and J. P. Pekola, Phys. Rev. B **89**, 014508 (2014).

[62] B. Josephson, Physics Letters **1**, 251 (1962).

[63] K. v. Klitzing, G. Dorda, and M. Pepper, Phys. Rev. Lett. **45**, 494 (1980).

[64] F. Piquemal, A. Bounouh, L. Devoille, N. Feltin, O. Thevenot, and G. Trapon, Comptes Rendus Physique **5**, 857 (2004), fundamental metrology.

[65] M. W. Keller, J. M. Martinis, N. M. Zimmerman, and A. H. Steinbach, Applied Physics Letters **69**, 1804 (1996).

[66] D. Averin and K. Likharev, Journal of Low Temperature Physics **62**, 345 (1986).

[67] L. P. Kouwenhoven, A. T. Johnson, N. C. van der Vaart, C. J. P. M. Harmans, and C. T. Foxon, Phys. Rev. Lett. **67**, 1626 (1991).

[68] H. Pothier, P. Lafarge, P. Orfila, C. Urbina, D. Esteve, and M. Devoret, Physica B: Condensed Matter **169**, 573 (1991).

[69] D. V. Averin and J. P. Pekola, Phys. Rev. Lett. **101**, 066801 (2008).

[70] V. F. Maisi, Y. A. Pashkin, S. Kafanov, J.-S. Tsai, and J. P. Pekola, New Journal of Physics **11**, 113057 (2009).

[71] T. Aref, V. F. Maisi, M. V. Gustafsson, P. Delsing, and J. P. Pekola, EPL (Europhysics Letters) **96**, 37008 (2011).

[72] D. D. Averin and A. N. Korotkov, Zh. Eksp. Teor. Fiz. **97**, 1661 (1990), [Sov. Phys. JETP 70, 937 (1990)].

[73] F. Giazotto, T. T. Heikkilä, A. Luukanen, A. M. Savin, and J. P. Pekola, Rev. Mod. Phys. **78**, 217 (2006).

[74] J. Clarke, Phys. Rev. Lett. **28**, 1363 (1972).

[75] M. Tinkham and J. Clarke, Phys. Rev. Lett. **28**, 1366 (1972).

[76] A. Rothwarf and B. N. Taylor, Phys. Rev. Lett. **19**, 27 (1967).

[77] B. A. Bernevig and T. L. Hughes, *Topological insulators and topological superconductors* (Princeton University Press, 2013).

[78] P. Kotetes, *Lecture Notes on Topological insulators and superconductors* (2014) http : //www.tfp.kit.edu/img/P_Kotetes__TKMI_lecture_2014.pdf.

[79] F. Bloch, Zeitschrift für Physik **52**, 555.

[80] L. Fu and C. L. Kane, Phys. Rev. B **74**, 195312 (2006).

[81] W. P. Su, J. R. Schrieffer, and A. J. Heeger, Phys. Rev. Lett. **42**, 1698 (1979).

[82] M. Z. Hasan and C. L. Kane, Rev. Mod. Phys. **82**, 3045 (2010).

[83] E. I. Rashba, Fizika tverd. tela **2**, 1224 (1960), [Sov. Phys. Solid. State, 2, 1109 (1960)].

[84] J. R. Schrieffer and P. A. Wolff, Phys. Rev. **149**, 491 (1966).

[85] E. J. H. Lee, X. Jiang, R. Aguado, G. Katsaros, C. M. Lieber, and S. De Franceschi, Phys. Rev. Lett. **109**, 186802 (2012).

[86] I. Martin and A. F. Morpurgo, Phys. Rev. B **85**, 144505 (2012).

[87] M. Kjaergaard, K. Wölms, and K. Flensberg, Phys. Rev. B **85**, 020503 (2012).

[88] S. Nadj-Perge, I. K. Drozdov, B. A. Bernevig, and A. Yazdani, Phys. Rev. B **88**, 020407 (2013).

[89] S. Nakosai, Y. Tanaka, and N. Nagaosa, Phys. Rev. B **88**, 180503 (2013).

[90] B. Braunecker and P. Simon, Phys. Rev. Lett. **111**, 147202 (2013).

[91] J. Klinovaja, P. Stano, A. Yazdani, and D. Loss, Phys. Rev. Lett. **111**, 186805 (2013).

[92] M. M. Vazifeh and M. Franz, Phys. Rev. Lett. **111**, 206802 (2013).

[93] F. Pientka, L. I. Glazman, and F. von Oppen, Phys. Rev. B **88**, 155420 (2013).

[94] F. Pientka, L. I. Glazman, and F. von Oppen, Phys. Rev. B **89**, 180505 (2014).

[95] K. Pöyhönen, A. Westström, J. Röntynen, and T. Ojanen, Phys. Rev. B **89**, 115109 (2014).

[96] J. Li, T. Neupert, B. A. Bernevig, and A. Yazdani, ArXiv e-prints (2014), arXiv:1404.4058 [cond-mat.mes-hall] .

[97] J. Alicea, Y. Oreg, G. Refael, F. von Oppen, and M. P. A. Fisher, Nat Phys **7**, 412 (2011).

[98] M. Leijnse and K. Flensberg, Semiconductor Science and Technology **27**, 124003 (2012).

[99] C. Beenakker, Annual Review of Condensed Matter Physics **4**, 113 (2013).

[100] D. Rainis and D. Loss, Phys. Rev. B **85**, 174533 (2012).

[101] M. S. Scheurer and A. Shnirman, Phys. Rev. B **88**, 064515 (2013).

[102] D. Serrate, P. Ferriani, Y. Yoshida, S.-W. Hla, M. Menzel, K. von Bergmann, S. Heinze, A. Kubetzka, and R. Wiesendanger, Nat Nano **5**, 350 (2010), 10.1038/nnano.2010.64.

[103] A. A. Khajetoorians, (2014), private communication.

[104] N. Y. Yao, L. I. Glazman, E. A. Demler, M. D. Lukin, and J. D. Sau, Phys. Rev. Lett. **113**, 087202 (2014).

[105] A. Heimes, P. Kotetes, and G. Schön, Phys. Rev. B **90**, 060507 (2014).

[106] P. Kotetes, New Journal of Physics **15**, 105027 (2013).

[107] R. Mersevey and B. B. Schwartz, *Superconductivity*, edited by R. D. Parks (Marcel Dekker, Inc. New York, 1969).

[108] R. Gross and A. Marx, *Festkörperphysik* (Oldenburg Verlag, 2012).

[109] C. P. J. Poole, H. A. Farach, R. J. Creswick, and R. Prozorov, *Superconductivity* (Elsevier, 3rd edition, 2014).

[110] A. Y. Kitaev, Physics-Uspekhi **44**, 131 (2001).

[111] H. J. Gardner, A. Kumar, L. Yu, P. Xiong, M. P. Warusawithana, L. Wang, O. Vafek, and D. G. Schlom, Nat Phys **7**, 895 (2011), 10.1038/nphys2075.

[112] M. M. Ozer, J. R. Thompson, and H. H. Weitering, Nat Phys **2**, 173 (2006).

[113] R. B. Dinner, A. P. Robinson, S. C. Wimbush, J. L. MacManus-Driscoll, and M. G. Blamire, Superconductor Science and Technology **24**, 055017 (2011).

[114] J. H. Dil, F. Meier, J. Lobo-Checa, L. Patthey, G. Bihlmayer, and J. Osterwalder, Phys. Rev. Lett. **101**, 266802 (2008).

[115] K. Yaji, Y. Ohtsubo, S. Hatta, H. Okuyama, K. Miyamoto, T. Okuda, A. Kimura, H. Namatame, M. Taniguchi, and T. Aruga, Nat Commun **1**, 17 (2010).

[116] B. Slomski, G. Landolt, G. Bihlmayer, J. Osterwalder, and J. H. Dil, Sci. Rep. **3** (2013).

[117] G. Bihlmayer, S. Blügel, and E. V. Chulkov, Phys. Rev. B **75**, 195414 (2007).

[118] H.-Y. Hui, P. M. R. Brydon, J. D. Sau, S. Tewari, and S. Das Sarma, ArXiv e-prints (2014), arXiv:1407.7519 [cond-mat.mes-hall] .

[119] P. M. R. Brydon, H.-Y. Hui, and J. D. Sau, ArXiv e-prints (2014), arXiv:1407.6345 [cond-mat.mes-hall] .

[120] A. Heimes, D. Mendler, and P. Kotetes, ArXiv e-prints (2014), arXiv:1410.6367 [cond-mat.mes-hall] .

[121] H. Imamura, P. Bruno, and Y. Utsumi, Phys. Rev. B **69**, 121303 (2004).

[122] M. Misiorny, M. Hell, and M. R. Wegewijs, Nat Phys **9**, 801 (2013).

[123] H. Brune and P. Gambardella, Surface Science **603**, 1812 (2009), special Issue of Surface Science dedicated to Prof. Dr. Dr. h.c. mult. Gerhard Ertl, Nobel-Laureate in Chemistry 2007.

[124] A. Roldán-Molina, M. J. Santander, A. S. Núñez, and J. Fernández-Rossier, Phys. Rev. B **89**, 054403 (2014).

[125] L. P. Gor'kov and E. I. Rashba, Phys. Rev. Lett. **87**, 037004 (2001).

[126] S. Tewari, T. D. Stanescu, J. D. Sau, and S. D. Sarma, New Journal of Physics **13**, 065004 (2011).

[127] S. Tewari and J. D. Sau, Phys. Rev. Lett. **109**, 150408 (2012).

[128] P. Kotetes, G. Schön, and A. Shnirman, Journal of the Korean Physical Society **62**, 1558 (2013).

[129] J. Röntynen and T. Ojanen, ArXiv e-prints (2014), arXiv:1406.4288 [cond-mat.mes-hall] .

[130] J. H. Cole, J. Leppäkangas, and M. Marthaler, New Journal of Physics **16**, 063019 (2014).

[131] C. H. van der Wal, F. K. Wilhelm, C. J. Harmans, and J. E. Mooij, Eur. Phys. J. B **31**, 111 (2003).

[132] S.-H. Ji, T. Zhang, Y.-S. Fu, X. Chen, X.-C. Ma, J. Li, W.-H. Duan, J.-F. Jia, and Q.-K. Xue, Phys. Rev. Lett. **100**, 226801 (2008).

[133] R. Fresard, B. Glaser, and P. Wolfle, Journal of Physics: Condensed Matter **4**, 8565 (1992).

[134] Y. V. Fominov, M. Houzet, and L. I. Glazman, Phys. Rev. B **84**, 224517 (2011).

[135] C. Gorter, Physica **17**, 777 (1951).